Experiment and simulation of micro injection molding and microwave sintering

Jianjun Shi

SPIM

Thèse de Doctorat

École doctorale sciences pour l'ingénieur et microtechniques
UNIVERSITÉ DE FRANCHE-COMTÉ

Prepared and presented at

L'U.F.R. DES SCIENCES ET TECHNIQUES
DE L'UNIVERSITÉ DE FRANCHE-COMTE

In order to obtain the

GRADE DE DOCTEUR DE L'UNIVERSITÉ DE FRANCHE-COMTE
Spécialité: Génie Mécanique

Experiment and Simulation of Micro-Injection Molding and Microwave Sintering

Expérimentation et Simulation de Micro-Moulage par Injection et Frittage par Micro Onde

Jianjun SHI

Defence on 5 May 2014, defence committee:

Chairman	X-G. ZENG	Professor, Sichuan University, China
Advisor	J-C. GELIN	Professor, Ecole Nationale Supérieure de Mécanique et des Microtechniques, Besançon
	B-S. LIU	Professor, Southwest Jiaotong University, China
Co-Advisor	T. BARRIERE	Professor, Université de Franche-Comté
	Z-Q. CHENG	Professor, Université de Franche-Comté
Reviewers	F. CHINESTA	Professor, Universités à l'Ecole Centrale de Nantes
	J-M. BERGHEAU	Professor, Ecole Nationale d'Ingénieurs de Saint Etienne
	F. VALDIVIESO	HDR, Ecole Nationale Supérieure des Mines de St-Etienne
Examinators	Z-Q. FENG	Professor, Université Evry Val d'Essonne
	J-H. ZHANG	Professor, Sichuan University, China
	L-X. CAI	Professor, Southwest Jiaotong University, China
	H. ZHAO	Professor, Southwest Jiaotong University, China

Classified Index: O345
U.D.C: 621

Southwest Jiaotong University & Franche-Comte University

Doctor Degree Dissertation

EXPERIMENT AND SIMULATION OF MICRO INJECTION MOLDING AND MICROWAVE SINTERING

Grade: 2009

Candidate: SHI Jianjun

Academic Degree Applied for: Doctor of Engineering

Speciality: Engineering Mechanics

Supervisor: LIU Baosheng, Jean-Claude GELIN

March, 2014

Declaration of initiative work for Ph.D. degree

The author hereby solemnly declares that: the present submitted doctoral thesis is the result of researches works carried out independently under the guidance of tutors. Besides the contents of references already mentioned, this thesis does not contain any other individual or collective research result that has been published or authored. Individual and collective contributions of this thesis have been clearly been mentioned in the thesis content. The author is fully aware of the legal consequences resulting from this statement.

The main innovations of the thesis are as follows:

(1) To improve the existing filling algorithm, for modification of the untrue filling patterns in previous in-house software and commercial software when modeling some specific cases, a numerical algorithm similar to upwind method is proposed to strengthen the advection effect of filling flow behind the filling front. In addition, a special algorithm is suggested to ensure the linear filling pattern of incompressible flow when given a constant injection velocity, by imposing reasonable outlet boundary conditions in the calculation model.

(2) The effect of surface tension force is taken into account in micro-injection molding simulation. Because there is no appropriate algorithm in finite element method for surface tension calculation, a simple and systematic operation is proposed and conformed in present thesis. The modeling results indicate that the effect of surface tension represents the significant importance in micro-injection molding process.

(3) Experiments and discoveries of microwave sintering: Implementation of microwave sintering experiment on 17-4PH stainless steel powder, some special results has been detected in present thesis. The author conforms that all the superiorities of microwave sintering relative to the traditional sintering also apply to 17-4PH stainless steel powder. Moreover, because of its rapid heating in the internal volumetric way, microwave sintering results in the obvious gradient in mechanic properties of the sintered material.

(4) Development of the simulation for multi-physics coupling phenomena in microwave sintering: The sintering constitution of powder impacts is planted into the calculation of microwave heating and heat transfer. Based on modeling and simulation of conventional sintering, and together with the principles of electromagnetic fields, thermodynamics and continuum mechanics, the method for multi-physics coupling simulation is built, including the sequenced calculations from distribution of the electromagnetic field to the densification of sintered compacts.

Signature of author:

Date：

Abstract

Powder Injection molding process consists of four main stages: feedstock preparation, injection molding, debinding and sintering. The thesis presents the research on two main aspects: micro-injection molding and microwave sintering. The main contributions can be concluded in the following four aspects: Modification and supplement of previous algorithm for the simulation of injection molding process; Evaluation and implementation of surface tension effect for micro injection; Microwave sintering experiments of compacts based on 17-4PH stainless steel; Realization of the microwave sintering simulation with the coupling of multi-physics, including the classic microwave heating, heat transfer, and the supplement of model for sintering densification of powder impacts.

For the improvement of filling simulation, the present study modifies the explicit vectorial algorithm for simulation of injection filling process. The wrongly directed filling patterns in actual commercial software have been improved, by the implementation of a suggested scheme, which is similar to upwind method. A reasonable numerical method relative to the outlet boundary condition is suggested to overcome the untrue delay of fully filling in the last filling stage. The results from these two modified algorithms are proved to be optimized and more reliable.

For extending the in-house FEM software into the scope of micro injection, surface tension effect is taken into account in the injection molding simulation. Due to the lack of appropriate FEM method for curvature calculation, the present work proposed a systematic algorithm for implementation of the surface tension effect in finite element method. By the example of filling in micro channels, it indicates that the effect of surface tension shows the importance for the projects in sub-millimeter sizes, but does not represent the significant effect in ordinary injection molding.

For microwave sintering of 17-4PH stainless steel powder, compared to the previous reports, some new discoveries have been found in the experiments. The author conform that the microwave sintering process for 17-4PH stainless steel can not only shorten greatly the sintering time, lower the peak sintering temperature, but also it provides higher sintered density and fewer defects in micro structure. Higher Vickers-hardness of microwave sintered compacts is also detected in the present work. Moreover, because of its rapid heating in the internal volumetric way, microwave sintering results in the obvious gradient in mechanic properties of the sintered material.

Microwave sintering represents the coupling of multi-physics in electro-magnetic fields, heat generation, thermal conduction, and densification process of the powder compacts in sintering. The existing researches focuses on the studies of microwave heating and heat

transfer, which couples with the evaluation of electromagnetic field, but none of them includes the densification behaviors of powder material. Bases on the sintering constitution of powder impacts, the mathematical model and simulation method for whole of the microwave sintering phenomena, from distribution of the electromagnetic field to the densification of sintered compacts, are determined in the present thesis. The simulation of microwave sintering process can be realized on the FEM platform of COMSOL Multi-physics. This work provides a reliable way for the further investigations on microwave sintering.

Key words：Micro-Injection Molding, Microwave Sintering, surface tension effect, 17-4PH stainless steel powder, Numerical Simulation, Multi-physics

Résumé

Procédé de moulage par injection de poudres est constitué de quatre étapes principales: la préparation des matières premières, moulage par injection, le déliantage et le frittage. Cette thèse présente les recherches sur deux aspects principaux: la micro-injection et frittage par micro-ondes. Les contributions principaux peuvent être conclues dans les quatre aspects suivants: Modification et complément de l'algorithme précédent pour la simulation du procédé de moulage par injection; L'évaluation et la mise en oeuvre de l'effet de tension de surface pour micro-injection; Micro-ondes expériences de frittage de compacts basés sur l'acier inoxydable 17-4PH; Réalisation de la simulation de frittage à micro-ondes avec couplage de la multi-physique, y compris le chauffage à micro-ondes classique, le transfert de chaleur, et le supplément de modèle pour la densification de frittage de la poudre compacté.

Pour l'amélioration de simulation de remplissage, l'étude présenté a modifié l'algorithme vectoriel explicite pour la simulation de procédés de remplissage par injection. Les motifs de remplissage dirigés à tort dans les logiciels actuelles commerciaux ont été améliorées, par la mise en œuvre d'un schème proposé, qui est similaire à la méthode contre le vent. Une méthode numérique raisonnable pour la condition de limite àla sortie est proposé. Le retard de pleine remplissage à la dernière phase d'injection est donc surmonté. Les résultats de ces deux algorithmes modifiés sont avérés être optimisé et plus fiable.

Pour étendre le logiciel interne FEM dans le champ d'application de micro-injection, l'effet de la tension de surface est prise en compte lors de la simulation de moulage par injection. En raison de l'absence de méthode appropriée des éléments finis pour le calcul de courbure, le présent travail a proposé un algorithme pour la mise en oeuvre systématique de l'effet de tension de surface dans la méthode des éléments finis. Par l'exemple de remplissage à micro-canaux, il indique que l'effet de la tension superficielle montre l'importance pour les projets dans les tailles des sous-millimétriques, mais ne représente pas l'effet significatif dans le moulage par injection ordinaire.

Pour les micro-ondes frittage de poudre d'acier inoxydable 17-4PH, par rapport aux rapports précédents, certaines nouvelles découvertes ont été trouvées dans les expériences. L'auteur confirme que le procédé de frittage par micro-ondes pour l'acier inoxydable 17-4PH, peut non seulement raccourcir considérablement le temps de frittage, baisser la sommet de temperature de frittage, mais il fournit également une densité frittée supérieure et moins de défauts de micro structure. Supérieur Vickers dureté de comprimés micro-ondes frittés est également détectée dans le présent ouvrage. En outre, en raison de son chauffage rapide par un moyenne interne volumétrique, les résultats de frittage par micro-ondes internes conduisent au gradient manifeste dans les propriétés mécaniques du matériau fritté.

Micro-ondes frittage représente le couplage multi-physique dans les champs électro-magnétiques, la production de chaleur, conduction thermique, et le processus de densification des poudres en frittage. Les recherches actuelles se concentrent sur les études de chauffage par micro-ondes et un transfert de chaleur, qui couple avec l'évaluation du champ électromagnétique, mais aucun d'entre eux comprennent les comportements de densification du matériau poudre. Bases sur le comportement de frittage des poudres compactés, le modèle mathématique et méthode de la simulation pour ensemble des phénomènes de frittage micro-ondes, depuis la distribution du champ électromagnétique et à la densification du corps frittés, sont déterminés dans la présente thèse. La simulation de procédé de frittage par micro-ondes peut être réalisé sur la plate-forme FEM de COMSOL Multi-physics. Ce travail fournit un moyen fiable pour les enquêtes sur micro-ondes frittage plus profondément.

Mots clés: La Micro-Injection, Micro-ondes Frittage, L'effet de la Tension de Surface, Poudre d'acier Inoxydable 17-4PH, Simulation Numérique, Multi-physiques

Glossary

CAGR:	Compound Annual Growth Rate
CCIM	Cemented Carbide Injection Molding
CIM	Ceramic Injection Molding
CLSVOF:	Coupled Level Set and Volume of Fluid
CSF:	Continuum Surface Force
CRH:	Conventional Resistive Heating
FEM：	Finite Element Method
FVM:	Finite Volume Method
FDM:	Finite Difference Method
FEMTO-ST:	Franche-Comté Electronique Mécanique Thermique et Optique – Sciences et Technologies
FDTD:	Finite Difference Time Domain
LS:	level Set
MIM:	Metal Injection Molding
MEMS:	Micro-Electro-Mechanical Systems
MW:	Microwave
PIM：	Powder Injection Molding
PP:	Polypropylene
PW:	Paraffin Wax
PLIC:	Piecewise Linear Interface Construction
SWJTU:	Southwest Jiaotong University
SUPG:	Streamline Upwind Petrov Galerkin
SA:	Stearic Acid
VOF:	Volume of Fluid

Nomenclature

A	assembling operation in finite element method
$\mathbf{B}$	derivative matrix of interpolation function N in an element
C_f	coefficient of tangent viscous load
C_p	specific heat coefficient of the feedstock (J/m/ºC)
C_a	specific heat coefficient of air (J/m/ºC)
C_{pp}	heat capacity (J/kg·ºC)

$\mathbf{D}$	divergence operator of velocity field
e	element
E	electric field (V/m)
E_{e}	elastic modulus (Pa)
$\boldsymbol{F}$	filling state variable
F_i	nodal values of filling state variable
$\boldsymbol{F}_{\mathrm{Frt}}$	filling state variable in the filling front
$\boldsymbol{F}_{\mathrm{low}}$	the lowest value for defining the range of filling front
$\boldsymbol{F}_{\mathrm{up}}$	the up value for defining the range of filling front
$\mathbf{F}^{\sigma}$	viscous diffusion term
$\mathbf{F}^{ext}$	external force vector
$\mathbf{F}^{\mathrm{d}}$	incompressibility correction term
$\mathbf{F}_{\mathrm{st}}$	surface tension force (Pa)
$\mathbf{F}_b$	body force in a thin layer of the front (Pa)
$\boldsymbol{F}_{\boldsymbol{p}}$	a prescribed value to identify the position of filling front
$\mathbf{f}$	tangent viscous load (Pa)
$\mathbf{f}^{ext}$	surface loads converted to the nodes on boundary (Pa)
f^*	kinematically admissible field associated to variable
$\mathbf{G}$	gradient operator constructed by derivatives of interpolation functions
G_P	shear viscosity modulus (Pa)
g	gravity vector ($\mathrm{m/s^2}$)
H	magnetic fields (A/m)
h_p	heat exchange coefficients of air (W/m/ºC)
h_a	heat exchange coefficients of feedstock (W/m/ºC)
I	second order identity tensor
$\mathbf{K}^{ad}$	stiffness matrix of advection effect for filling state and temperature field
$\mathbf{K}^{df}$	stiffness matrix of diffusion effect for filling state and temperature field

$\mathbf{K}^{adv}$	stiffness matrix of advection effect for velocity field
K^{o}	operator for outlet surface integration term
K_P	bulk viscosity modulus (Pa)
k_p	thermal conductivity coefficient of the feedstock (W/m/ºC)
k_a	thermal conductivity coefficient of air (W/m/ºC)
k	the upwind-stream node number
$\mathbf{M}_0$	lumped pseudo matrix
$\mathbf{M}$	mass matrix lumped into diagonal form
m	node number in an element
$\mathbf{N}$	matrix of interpolation function
$\boldsymbol{N}_{out}$	nodes associated to outlet surface
$\mathbf{N}_i$	interpolation functions
$\vec{\boldsymbol{n}}_{out}$	a unit vector normal to its edge or side Γ^e_{out}
$\vec{\mathbf{n}}$	unit of outward normal
P	injected pressure on inlet boundary (Pa)
P	hydraulic pressure field (Pa)
P_h	heat source (J)
P_i	nodal pressure values (Pa)
$\dot{\mathbf{Q}}$	heat dissipation term (W.m)
$\mathbf{q}^c$	heat convection term (J)
T	Temperature (℃)
T_i	nodal temperature values (℃)
$\vec{\mathbf{t}}$	unit vector of local tangent
Δt	time increment (s)
V	velocity vector (m/s)
$\mathrm{V_I}$	injected velocity on inlet boundary (m/s)
$\mathbf{V}_i$	nodal velocity vector (m/s)

$\mathbf{V}^{\mathrm{e}}$	velocity vector at each Gauss point in an element (m/s)
$\{\boldsymbol{V}\}_{\boldsymbol{F}}$	discretized value of velocity field at each node
$\{\boldsymbol{V}^{\boldsymbol{e}}\}_{\boldsymbol{F}}$	the column of velocity values at all nodes of an elements
$\boldsymbol{V}_{\boldsymbol{n}}^{\boldsymbol{e}}$	velocity vector in the element associated to $\Gamma_{\boldsymbol{out}}^{\boldsymbol{e}}$ (m/s)
$\|\boldsymbol{V}_{\boldsymbol{n}}\|$	norm of velocity vector (m/s)
$\boldsymbol{V}_{\mathrm{n}}^{*}$	velocity fields of temporary middle values (m/s)
$\boldsymbol{X}$	space position
$\boldsymbol{X}_{\boldsymbol{F}}$	position of filling front
Ω	sum of space position in entire model
Ω_{F}	filled portion in mold cavity
Ω_{V}	void portion in mould cavity
Ω_{Frt}	filling front region
$\Omega_{\boldsymbol{out}}^{\boldsymbol{e}}$	elements associated to node $\boldsymbol{N}_{\boldsymbol{out}}$
Γ_{I}	inlet of the mold
Γ_{O}	outlet of the mold
Γ_{S}	intersection of filled portion and void portion
$\mathbf{\Gamma}^{\mathbf{w}}$	mold walls
$\Gamma_{\boldsymbol{out}}^{\boldsymbol{e}}$	edge or side of element $\Omega_{\boldsymbol{out}}^{\boldsymbol{e}}$ on outlet boundary
ρ_{p}	density value of feedstock (kg/m^3)
ρ_{a}	density value of air (kg/m^3)
ρ	density of the materials (kg/m^3)
ρ_{r}	relative density (kg/m^3)
σ	coefficient of surface tension
σ_{t}	stress tensor in sintered materials (Pa)
$\boldsymbol{\sigma}'$	deviator of Cauchy stress tensor (Pa)
$\boldsymbol{\sigma}_{p}'$	deviator of Cauchy stress tensor in the filled portion (Pa)
$\boldsymbol{\sigma}_{a}'$	deviator of Cauchy stress tensor in the void portion (Pa)

σ_s	sintering stress (Pa)
σ_{EC}	electric conductivity (S)
σ_{air}	electric conductivity of air (S)
$tr\sigma$	trace of the stress tensor
$\dot{\boldsymbol{\varepsilon}}_p$	strain rate of feedstock
$\dot{\boldsymbol{\varepsilon}}_a$	strain rate of air
ε_r	relative complex permittivity (F/m)
ε_r'	dielectric constant (F/m)
ε_r''	dielectric losses factor (F/m)
$tr(\dot{\boldsymbol{\varepsilon}})$	trace of total strain rate
$\dot{\boldsymbol{\varepsilon}}$	tensor of total strain rate
$\dot{\boldsymbol{\varepsilon}}_e$	elastic strain rate
$\dot{\boldsymbol{\varepsilon}}_{th}$	thermal strain rate
$\dot{\boldsymbol{\varepsilon}}_{vp}$	viscoplastic strain rate
λ^F	dilatation coefficient in filled portion
λ^V	dilatation coefficient in void portion
κ	curvature of filling front surface
φ	signed distance function to the interface
$\delta(x)$	delta function concentrated at the interface
ω	angular frequency of the microwave source (rad/s)
μ_r	relative complex permeability (H/m)
μ_r''	magnetic loss factor (H/m)
k	thermal conductivity (W/(m·K))
α	coefficient of thermal dilatation (m/K)
ν	Poisson’s ratio

Table of Contents

Introduction

The PIM (Powder injection molding) industry is comprised of MIM (metal injection molding), CIM (ceramic injection molding) and CCIM (cemented carbide injection molding). This manufacturing process is very efficient for producing small, complex and intricate components in large batch. Excellent mechanical properties and proper geometrical accuracy can be obtained by this newly developed technology under a cost much lower than by the traditional ones. These notable advantages make them a strong competitiveness in the market of alloy die cast components. It creates a new market mainly for complex miniature components. A diverse range of PIM products are used in the chemical, textile, aerospace, automotive, electronic, medical and communications industries. Examples of the components resulting from PIM process are related in the Fig. 1.

Fig. 1 Examples of macro and micro components from PIM process, including the shaft, gear, screw, pin, etc.

The PIM technology combines the well-known polymer injection molding and powder metallurgy technology. It consists of four sequential stages: mixing of the metallic and ceramic powders with the thermoplastic binders to get the feedstock, injection molding of the mixtures of feedstock in the mold die cavities, debinding of green parts to mostly remove the binder and finally sintering of brown parts by solid state diffusion to get the densified component.

The PIM process has already been focused and developed for several decades. Now for satisfying the market requirement, this process draws more and more attention to realize the

manufacturing of intricate structure, advance the miniaturization and reduce the waste of energy by improving the production efficiency. Under this condition, how to achieve the good dimensional accuracy and the desired mechanical properties is one of the key issues to extend the application of PIM process. It is necessary to design the injection molds and process according to the final properties of the components. In order to solve this inverse problem, the trial and error method is often used. But the experimental tests are very expensive to be carried out, and the period for the determination of process parameters is generally long for the production of new components. Alternatively, numerical simulation is a cost-effective way to optimize the PIM process design, which is viewed as computer experiments.

However, although PIM theory has been developed for about 40 years, the physical modeling and numerical simulation are far behind the practices. There remain some persistent problems in the previous developing algorithm, which results in the untrue injection filling patterns. And there is still much work to do in physical experiment for the calibration of sintering constitutive for powder material, spatially when using the new sintering way by microwave heating. So to promote the application, experimental and numerical simulation researches for micro injection molding process and microwave sintering process are presented in the present thesis. The itinerary of the study is organized as follows:

In chapter 1, a brief introduction is made on the process of PIM manufacture, including relative equipment used in the sequenced stages, the advantages of PIM technology, the development and market analysis and the relative scientific research centers for European, Asian and America regions.

In chapter 2, the explicit algorithm with fully vectorial operations for simulation of the injection molding stag is introduced. This vectorial method was previously developed in research team and there remains some unfavorable problems. The work in this chapter is going to optimize the previous algorithm and in-house software. The author improves the untrue distortion in simulation results when some specific runners in shape $\perp$ and L are involved, by the implementation of a suggested scheme. In addition, the untrue delay of filling process when the cavity is near fully filled has been modified. A proposed method is

realized to complement the boundary condition on outlet in simulation of the filling advection. It is proved that these two modification works make the results of simulation more stable and reliable.

In chapter 3, for extending the functionality of in-house software into the problems in micro scales, the evaluation of surface tension effect in the injection molding simulation is implementing by a specially proposed algorithm. Through analyzing the proportion of surface tension force to viscous force in different mold sizes, the effects of surface tension in micro injection molding process are evaluated.

Chapter 4 turns to the investigation of another PIM stage: sintering. The diverse sintering methods and the foundational theories for sintering are briefly introduced. The three sintering models for numerical simulation have been shown, including models in microscopic, mesoscopic and macroscopic.

Chapter 5 makes experiment investigation of microwave sintering. As a new developing technology, Microwave sintering is more and more accepted for its industrial values, which shows significant advantages against conventional sintering procedures. So the research team expands its research topics into microwave sintering field. The densification behaviors of 17-4PH stainless steel powder under microwave sintering are chosen for experimental investigations, because of its sole report and unfavorable conclusion. The relationship between processing factors and the evolution behaviors of powder material is investigated by experiments. The experimental researches will prove the results of microwave sintering for 17-4PH stainless steel powder, under the adequate conditions. The micro structure and mechanic properties in the sintered bodies will be investigated. The distribution of mechanic properties is measured to evaluation the effect of microwave heating and its special outcome on the sintered products. The influences of peak sintering temperature, holding time, heating rate and pre-sintering stages on densification behaviors of the powder material are investigated. The evolutions of microstructure in the sintered components under different sintering conditions are observed by the optical microscope. The Comparison between microwave sintering and conventional sintering is also the interest of investigation.

Chapter 6 focuses on the investigation of numerical simulation method for microwave

sintering process. It expands the actual sintering simulation from heat generation by microwave and temperature evolution to the coupling of multi-physics for whole process. The modeling and simulation includes the coupling effects from distribution of the electro-magnetic fields to the densification of the sintered material. The developed simulation realizes the coupling of electro-magnetic fields, heat generation by microwave effects, heat conduction, and densification process of PIM materials. The last one is based on the sintering model developed in research team. The prediction on evolution of sintering shrinkage and distribution of relative density is achieved based on the coupling of different physical phenomena. This work provides a reliable frame for further investigation of the coupling among the evolution of different material properties during the course of sintering.

Chapter 1 State of the art

1.1 Brief introduction of PIM

The PIM (Powder Injection molding) process is somewhat similar to plastic-injection molding. It combines the well-known polymer injection molding and powder metallurgy process. It consists of the following stages: feedstock preparation, injection molding, debinding of green parts and sintering of brown parts [1]. The PIM process can be stated in Fig. 1-1.

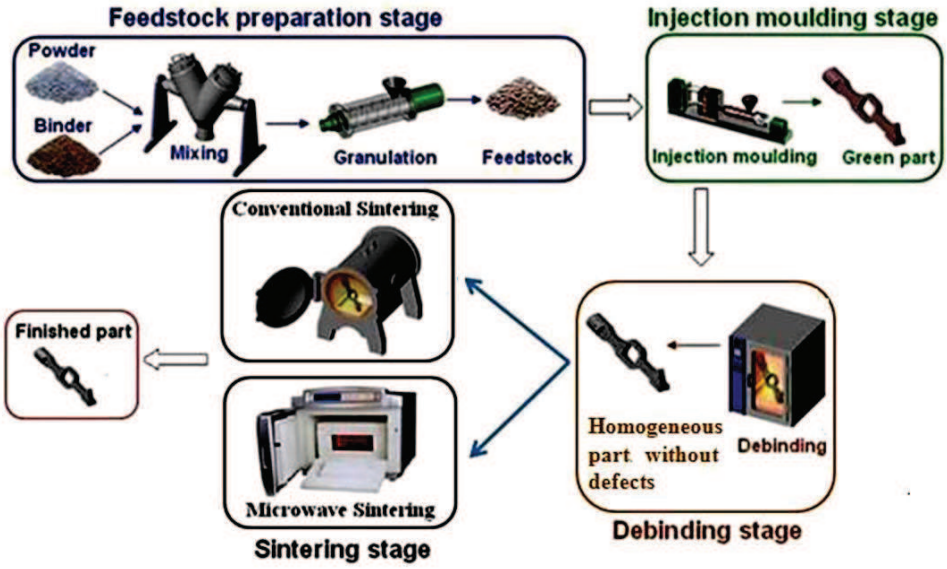

Fig. 1-1 The sequential stages to get the final sintered components [2]. The sintering stage may be processed by Conventional Resistive Heating or Microwave sintering ways.

As showed in Fig. 1-1, feedstock formed by metallic or ceramic powder and thermoplastic binder are prepared and pelletized for injection. Then by using a standard injection-molding process, the polymer-powder mixture is melted and injected into a die cavity under pressure, where it cools and solidifies into the shape of the desired part. Subsequent thermal, solvent or catalytic debinding processes remove the unwanted polymer binder and get a shaped metallic component in porous state. Lastly the brown parts are sintered to get the high-density products in pure metallic or ceramic material.

1) Feedstock preparation stage

In this preliminary state, very fine metallic or ceramic powder are mixed with

thermoplastic polymer (known as the binder) to form a homogeneous mixture of ingredients that is pelletized and can be fed directly into an injection molding process. This pelletized powder-polymer mixture is known as feedstock [3]. Generally, the grain size of the powder may vary from 2 to 20 μm with near spherical shapes. The elaboration of a successful feedstock balances several considerations [3, 4]. It is expect that the feedstock can be as condensed as possible to avoid a large sintering shrinkage. Formulations with high powder contents have the advantages such as: Closer dimensional control leading to tighter tolerances; Reduced probability of distortion during debinding; Improved handling strength after debinding; Reduction of debinding time; Reduced grain growth; Improved structural integrity. However, reducing the proportion of binder can also cause the difficulties. It usually has an adverse effect on the rheology of the material being injected into the mold [5]. Most problems in PIM are caused by a poor appreciation of component-rheology and thermal-rheology interactions. To enhance the process, the portion of powder loading must be maximized without scarifying the rheology. PIM compositions should ideally have low viscosity. At the meantime, it should also have low Herschel Buckley attribute yield stress and pseudo-plastic or shear-thinning characteristics [6]. The behavior similar to that of the toothpaste is generally desirable. The feedstock mixing equipment used in FEMTO-ST institute in France is shown in Fig. 1-2. The one used in the lab of Southwest Jiaotong University (SWJTU) is shown in Fig. 1-3. Both of them are using twin-screw mixer.

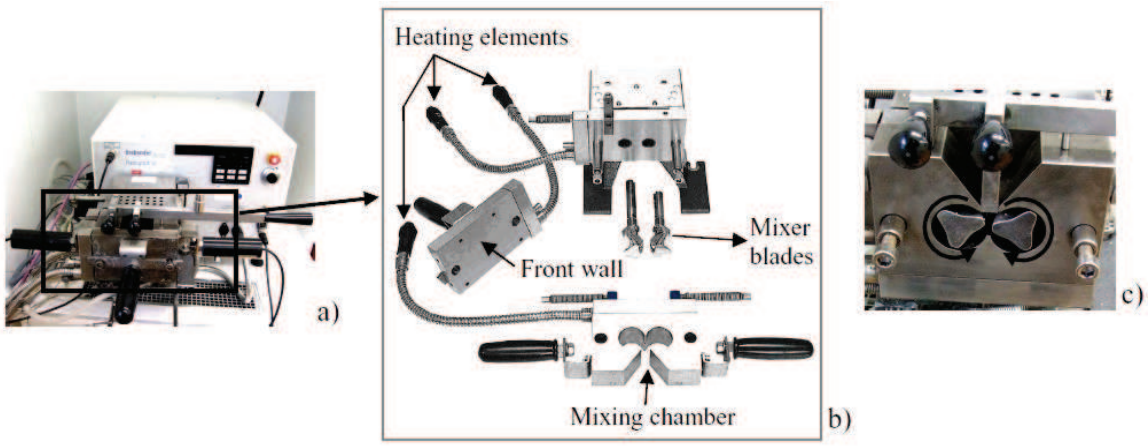

Fig. 1-2 Brabender® twin-screw mixer W 50 EHT, a) general view of the mixer; b) assembly of mixing equipment; c) the two mixer blades and their counter-rotation towards each other

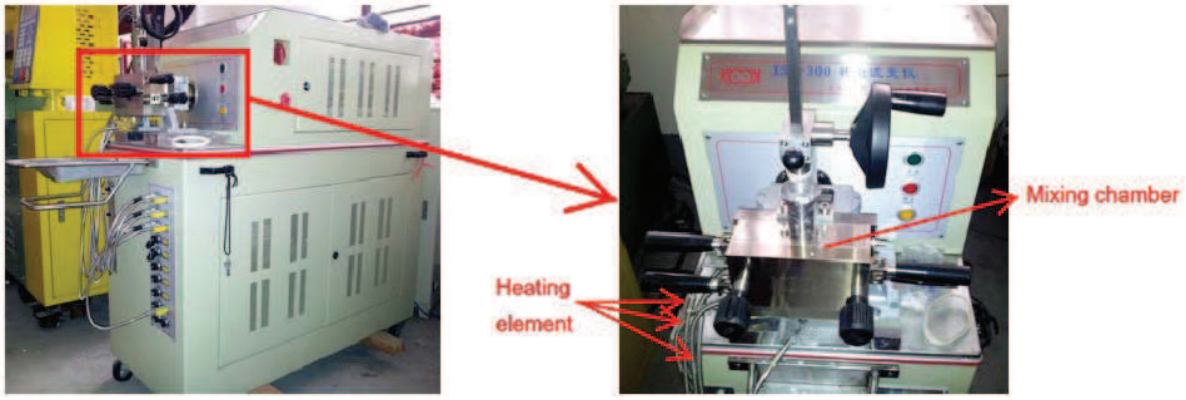

a) b)

Fig. 1-3 Torque rheometer (XSS-300) used in the lab of SWJTU: a) general view of the mixer; b) general view of the mixing chamber

The main parameters of these two mixers are indicated below:

Technical specifications	Brabender® twin-screw mixer (FEMTO-ST)	Torque rheometer XSS-300 (SWJTU)
mixing temperature	20 to 500 °C	20 to 400 °C
mixing speed	0 to 120 rpm	2 to 120 rpm
maximal mixing torque	150 N·m	300 N·m
volume of mixer bowl	55 cm^3	60 cm^3

2) Injection molding stage

This stage includes the injection molding of feedstock and the removal of green parts from the mold [7, 8]. A schematic cycle of the injection molding is shown in Fig. 1-4, which is the same equipment and tooling that are used in plastic injection molding, but it needs higher wearing resistance. In the injection molding stage, the feedstock is injected into the mold cavities under a certain pressure about 60 MPa or more. The pressure is maintained on the feedstock during the cooling until it solidifies at the gates. Then the component is ejected and another new cycle can be repeated. The injection equipment used in FEMTO-ST and SWJTU is shown in Fig. 1-5.

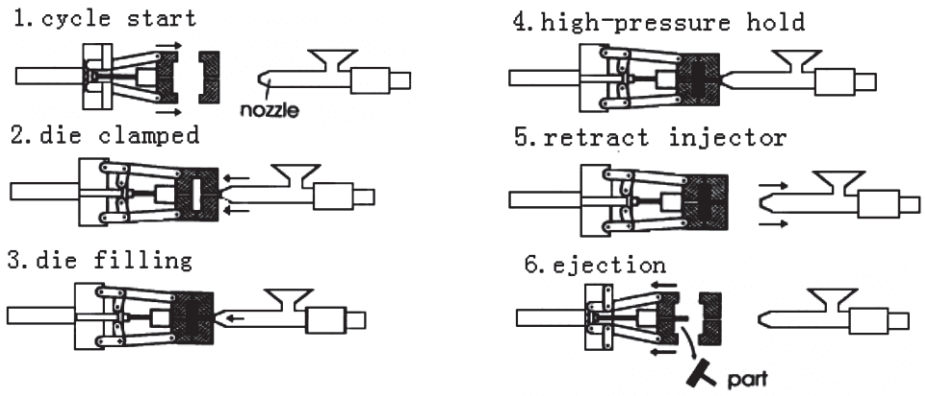

Fig. 1-4 Different steps of the injection molding [9]

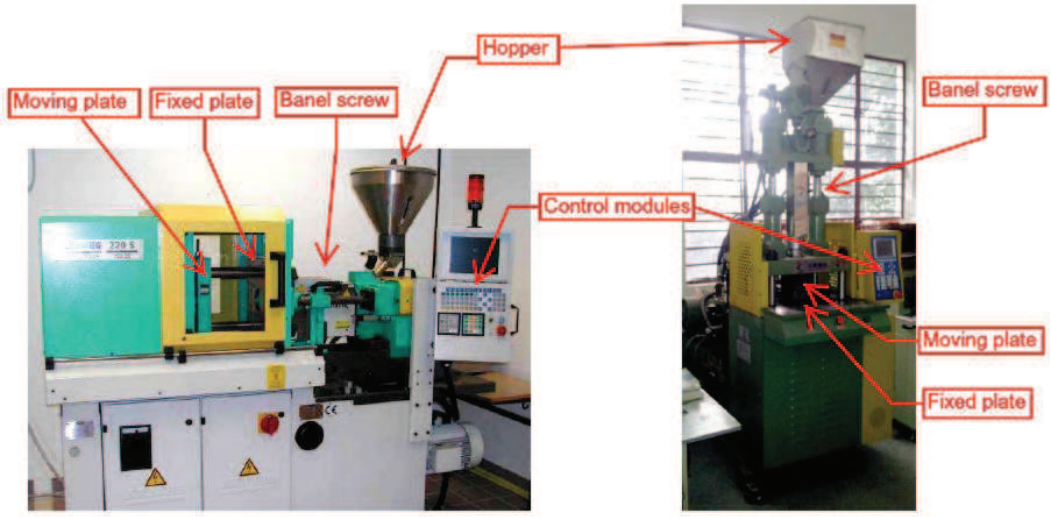

a) b)

Fig. 1-5 Injection equipment: a) Hydraulic Arburg 220-S horizontal injection equipment used in FEMTO-ST; b) TY-400 vertical injection equipment used in SWJTU.

The main technical data of these two injection equipment are shown below:

Technical specifications	Hydraulic Arburg 220-S (FEMTO-ST)	TY-400 (SWJTU)
Clamping force (max.)	20 kN	400 kN
Injection volume	3 to 12 cm^3	73.8 cm^3
Injection speed (max.)	366 mm/s	72 mm/s
Injection temperature (max.)	400 °C	400 °C
Injection pressure (max.)	250 MPa	217 MPa
Injection flow (max.)	22 cm^3/s	44.7 cm^3/s

3) Debinding of green parts

The debinding step is required to remove the binding additives from the green compacts as a prerequisite for sintering. The thermal, solvent or catalytic debinding process is used to get the shaped metallic components in porous state [10]. This process is a complex combination of chemical and physical degradation of the binders under thermal conditions. It is primarily dependent on the binder system used. In the solvent debinding process [11], the injected components are placed in a solvent fluid or vapor to dissolve the binders. The other debinding method is thermal debinding that removes the binders by heating the compacts [12]. In the catalytic debinding [13], the compacts are heated in atmosphere which containing catalyst to sweep away the polymer binders. The result is known as the brown part that still keeps its original geometry and size. For the experimental researches, the thermal debinding device in FEMTO-ST and SWJTU is shown in Fig. 1-6.

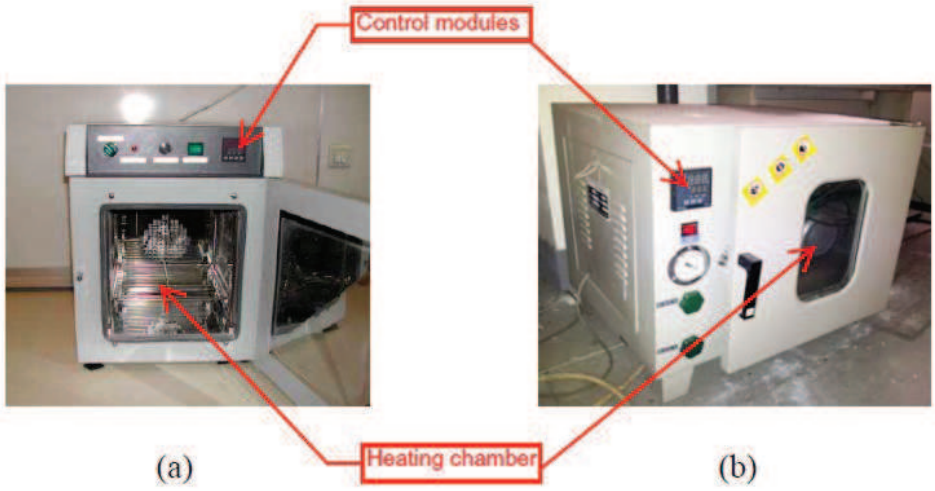

Fig. 1-6 Thermal debinding oven used in (a) FEMTO-ST, (b)SWJTU

The principal technical specifications of these two ovens are related below:

Technical specifications	(FEMTO-ST)	OZE8020 (SWJTU)
Test temperature (max.)	300 °C	250 °C
Volume (max.)	27 L	24.7 L
Gas circulation	air, argon	air, argon, nitrogen
Gas flow (max.)	200 cm^3/min	200 cm^3/min

4) Sintering of brown parts

In this process, the brown part is heated to approximately 85% of the material's melting temperature. Sintering is often performed in a protective atmosphere or vacuum at a peak temperature, which results in rapid elimination of the pores left by departure of the binder. It bonds the metallic or ceramic powders together, allowing densification and shrinking of the powders turning to a much denser solid with the elimination of pores. The sintered density is approximately 98% of theoretical value, which ensures the proper mechanical characteristics and corrosion properties. A shrinkage about 10~20% is obtained corresponding to the elimination of binder and porosity, as shown in Fig. 1-7 [14]. The end result is a metal or ceramic component in net shape or near net-shape, with properties similar to that of the bar stocks. The sintering furnace in FEMTO-ST and SWJTU for research of the sintering cycle is shown in Fig. 1-8.

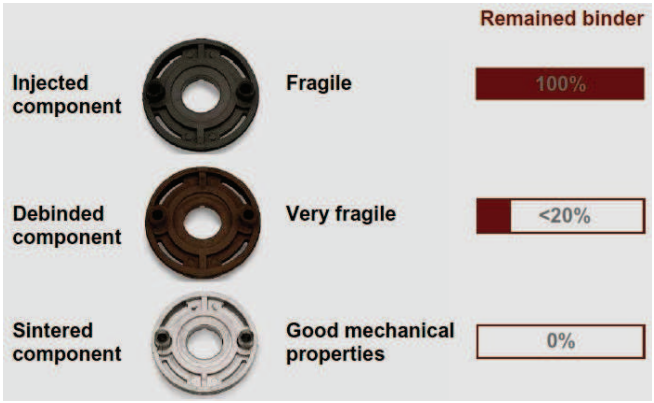

Fig. 1-7 Remained binder in the component issued from different stages of the PIM process [14]

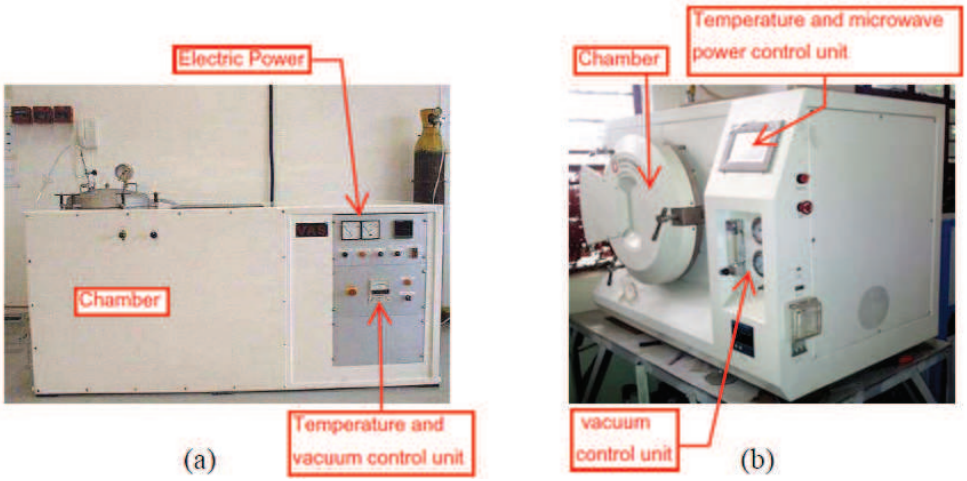

Fig. 1-8 Sintering furnace: (a) Conventional sintering furnace (provided by VAS®) used in FEMTO-ST, (b) Microwave sintering furnace (HAMiLab-V1500) used in SWJTU

The principal technical specification of the sintering furnace is given below:

Technical specifications	Conventional sintering furnace (FEMTO-ST)	Microwave sintering furnace (SWJTU)
Test temperature (max.)	2200 °C	1600℃
Volume (max.)	50 L	1.15 L
Atmosphere	gas circulation: argon, helium; primary vacuum: 10^{-3} mbar, secondary vacuum: 10^{-5} mbar;	gas circulation: argon, helium，nitrogen or the mixture; Static vacuum:＜100Pa
Heating source	graphic heating elements	2.45GHz ± 25MHz Microwave The Continuous adjustable output power: 0.2～1.40KW
Component holder	ceramic plates	Corundum mullite

In addition, some equipment for physical, rheology and mechanical analysis are needed, as show in Fig. 1-9.

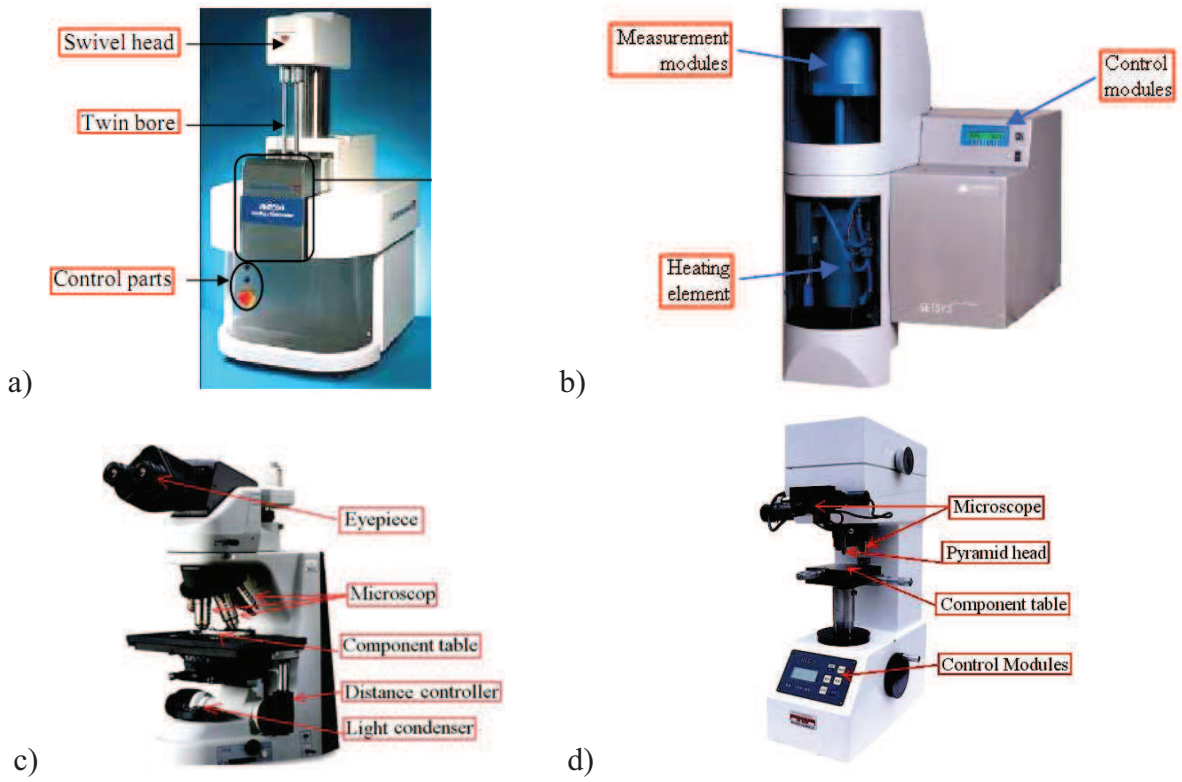

Fig. 1-9 The analysis equipment: a) RH2000 Capillary rheometer for the measurement of viscosity; b) Vertical SETSYS® dilatometer used for the calibration of sintering constitutive; c) Nikon Eclipse 55I/50I microscope used for observation of the sintered grains morphology; d) HV-5 small load Vickers hardness tester.

1.2 The advantages of PIM

As comparison to the conventional metal-forming processes, which is still in a wide range of applications in industrial production, like machining, stamping, forging, casting and powder metallurgy, PIM shows some superiorities and is fast becoming an integral process in metal forming, as shown in Table 1-1.

Table 1-1 Comparison of PIM to conventional metal-forming processes [15]

Parameters	PIM	Powder Metallurgy	Casting	Machining	Stamping
Density	98%	86%	98%	100%	100%
Tensile Strength	High	Low	High	High	High
Surface Finish	High	Medium	Medium	High	High
Miniaturization	High	Medium	Low	Medium	High
Thin Wall Capability	High	Medium	Medium	Low	High
Complexity	High	Low	Medium	High	Low
Design Flexibility	High	Medium	Medium	Medium	Low
Production Quantity	High	High	Medium	Med-High	High
Range of Materials	High	High	Med-high	High	Medium
Affordability	High	High	Medium	Low	High

PIM has the notable advantages as plastic injection molding process [16]. A crucial advantage of the process is that its near-net-shape capability, which means that very few finishing work is required. It enables the processing of metals with high melting temperature and ceramics, with the following benefits [17]:

1) Attractive cost savings, suitable for moderate-to-high production volume;
2) Great versatility and freedom in design, suitable for intricate and complex geometries such as dovetails, slots, undercuts, threads, and complex curved surfaces;
3) Wide latitude of component shape, sizes (0.1g to 250g) and design;
4) Good dimensional control with close tolerances of ±0.5%;
5) Net shape production, eliminating or minimizing machining and sub-assemblies;

6) Wide range of available alloys;
7) Capability to process the materials very hard and difficult to machine, which cannot be produced by any other technology, such as cermets and ceramics;
8) High material density nearly 95% to 98%, approaching to wrought material properties.

1.3 PIM development and market

The appearance of PIM technology is due to the development of powder metallurgy. It was first used in 1930s for manufacturing ceramic sheaths of spark plug insulators. The process was adopted by the investment casting industry in which it is now still used for manufacturing ceramic cores. However, PIM attracted little other interest until it was used for the molding of metal powders in the mid-1970s. Before 1970, there were only 10 papers related to Metal Injection Molding (MIM) process, even more generally in the domain of PIM, then the number increased to 100 in 1980 and more than 1000 scientific articles were published at the end of 1999 [18]. In the later 8 years, 3120 papers have been issued, including 1810 about MIM process. Till 2007, number of the related scientific papers raised twice [19]. Up to now, the journals related to PIM have been widely distributed, such as Powder Metallurgy, Powder Injection Molding International, International Journal of Powder Metallurgy, Journal of the American Ceramic Society, and Journal of the European Ceramic Society etc. Besides, 400 patents have been registered since 1990s in USA [19]. The researches strengthened the science and knowledge base of PIM. It is now recognized as a sophisticated, interdisciplinary technology. This novel application will initiate the considerable worldwide researches in the coming years.

From a market perspective, the portion of MIM in PIM is over 75%. A general resume of the sales for PIM and MIM has been indicated in Fig. 1-10. The MIM field has exhibited enormous growth since the first sale statistics were gathered in 1986, amounting to $9 million globally. Today, MIM is the dominant form of powder injection molding and has sustained 14% of growth per year in recent years, regardless of a few years of drop. This plot shows that the ceramic business contracted in recent years while MIM expanded, largely due

to the aerospace slowdown. The segment of ceramic injection molding was most likely about $158 million in 2012.

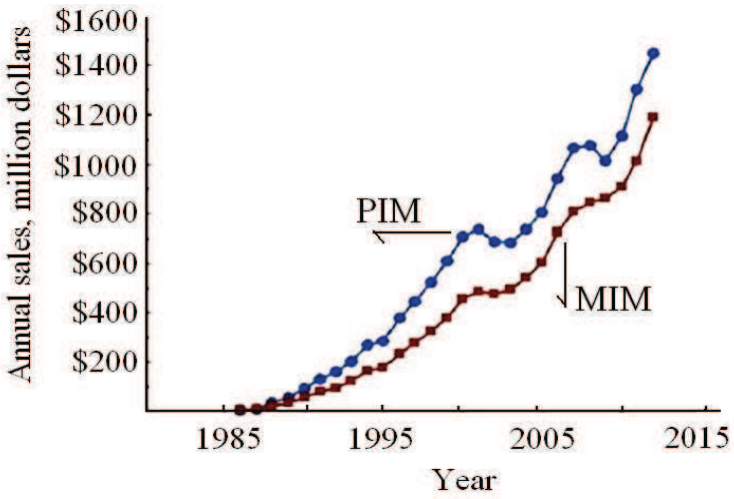

Fig. 1-10 Annual sales of powder injection molding (PIM) and the subset of metal injection molding (MIM) plotted from earlist recorded values to 2012 [20].

In fact, the PIM has spread around the world, including Austria, Belgium, Brazil, Canada, China, Czech Republic, France, Germany, Hungary, India, Ireland, Israel, Italy, Japan, South Korea, Malaysia, Mexico, Netherlands, Singapore, South Africa, Spain, Sweden, Switzerland, the United States and other countries and Chinese Taiwan area. By now, the world has more than 500 companies and institutions involved in the PIM research and development, production and consulting services.

Considering the sales of the firms identified in PIM, a survey from 1990 to 2010 gives the variations in Fig. 1-11, according to geographical origin. The number of firms has grown from about 50 to about 350. It can be clearly observed that China and India had rapidly developed in the last decades and this tendency will continue in the coming years.

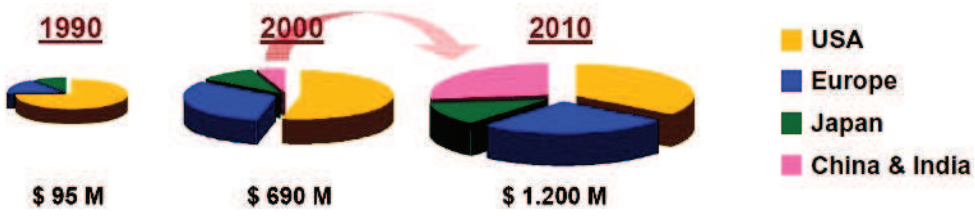

Fig. 1-11 Survey of the sales according to geographical regions (1990 to 2010) [21]

The number of MIM firms has not shown much change in recent times, but the size and sophistication have grown considerably. Various estimations have been offered for how far and how long MIM can sustain the growth. According to a report from Global Industry Analysts, a worldwide business strategy and market intelligence source, released in August 2011, the combined metal and ceramic injection molding market will be worth US$3.7 billion globally by 2017. Continuation of the MIM growth is strongly supported by the economic drivers. Table 1-2 [22], from BCC-research on Metal and Ceramic Injection Molding (AVM049B, retrieved 10/31/2012), illustrates well the projected growth rates. The global MIM market projected to increase from US$ 985 million in 2009 to US$ 1.9 billion in 2014. It represents 14.0% of the compound annual growth rate (CAGR). The strong technical players in MIM can expect to bring more value to customers than all of us can imagined [23].

Table 1-2 Expected global sales of MIM components by region in 2014 [22]

	2009		2014		CAGR%
Region	**($ millions)**	**(% share)**	**($ millions)**	**(% share)**	**2009-2014**
Asia	460.8	48	959.0	51	15.8
Europe	279.7	28	484.0	25	11.6
North America	231.0	23	424.0	22	12.9
Rest of the world	13.4	1	33.0	2	19.8
Total	**984.9**	**100**	**1900.0**	**100**	**14.0**

1.4 The principal research centers in PIM processing

In America, Prof. German and his research team have focused on the PIM process for long time [1, 9, 10, 18, 19, 24, 25]. In Europe, there are active studies in many countries. In United Kingdom, Prof. Ediridsinghe and his research team in Brunel university do the researches related to the large ceramic components [26-29]. Dr. Alock [30] in University of Cranfield mainly commits to the micro-manufacturing, which is also done by Dr. Kowalski [31] in

University of Delft in Netherlands. In Germany, several technical research centers concentrate on the elaboration of components by MIM process, they are Fraunhofer (FhG-IFAM: Dr. Petzoldt [32]; FhG-IWM: Dr. Kraft [33]) and KIT Karlshuhe (Dr. Piotter [34], Ruprecht [35]). In Switzerland, the application of NiTi shape memory materials has been studied with powder injection molding process (Prof. Carreño-Morelli [36]). In the Swedish, characterization of feedstock and its components is studying at Chalmers university (Prof. Nyborg [37]). In Spain, two research groups are developing some new feedstock, especially for M2 HSS (High Speed Steel) in University of Castilla La Mancha, large activities in PIM are also developed by JM Torralba team (university of Madrid, Carlos III) [38]. T Vieira has developed special coating method to improve the fluidity of the feedstock (at Coimbra university) [39] in Portugal. In Austria, a set of modern equipment has been set to build a large center in MIM fields, regrouping a lot of equipment providers. In Japan, several types of very fine powders dedicated to micro-MIM or the other nanotechnology applications have been developed. As example, iron, stainless steel, zircon, nickel and so on, have been used to develop proper feedstock and processes for large varieties of applications [40, 41]. In Korea, the development of MIM process with the titanium, copper, tungsten powders and several alloys have been developed by collaborations with the research centers in USA [42, 43]. Also, the international companies such as Parmatech and FloMet in the United States, BASF in Germany, Pacmaco in Switzerland, AMT in Singapore are well-known in the field.

1.5 Researches on PIM process in France and in China

In France, the researches related to MIM process have been carried out since 1985; meanwhile, the molding stage, the debinding and segregation analyses related to this process have been studied at Ecole des Mines de Paris. Since ten years, an increasing number of laboratories are involved in PIM activities. The ECAM laboratory developed feedstock with biodegradable polymer for biomedical applications. BioPIM project supervised by CEA LITEN (Grenoble, France) is going to develop some components with biodegradable polymer. In CRITT research centers in Charleville-Mézières, a platform has been developed

for pre-industrialization of PIM production. Since two years, POUDR'INNOV platform starts its activities with large investments in Rhône-Alpes, in order to diffuse and promote PIM opportunities. Since two years, almost twenty partners from industries and research centers are participating to SF2M group in order to promote PIM potentialities for industries. From 2010-2013, Newpim projects (FUI Newpim) have regrouped 13 partners to develop miniature components with functional materials and the modeling and simulation of sequential and global stages for MIM process. The projects have been managed by Alliance and Femto-ST. A new project managed by Emetringstene and including 10 partners (Fento, A. Raymond, Radiall, CEA, ...) begin in July 2013, for three years to develop micro component with high accuracy for new materials. Furthermore, DMA is very active partner in Mylisto equipex from 2011 to 2020 to develop a special platform to obtain special and innovative equipment to elaborate micro-components with functional materials with a very short production time by combining all stage and captive innovating process.

China began evolving in the field of PIM since the late 1980s. Central Iron & Steel Research Institute, University of Science and Technology Beijing, Central South University, General Research Institute for Nonferrous Metals, Guangzhou Research Institute of Nonferrous Metals, Beijing Research Institute of Powder Metallurgy carried out successively the PIM researches. In 1990's, more and more universities and institutes were involved. Several PIM Labs were established, such as the PIM Lab of Powder Metallurgy in Central South University. Under the financial support of Nature Science Foundation of China, 863 High-tech agency of China, a lot of fundamental and applied researches have been conducted. Many products are associated with the specific applications such as wristwatches, tungsten penetrators, gun components. Based on these ten years research achievement, to the end of the 90s, the institutes mastered gradually the independent PIM manufacturing technology. Then many big enterprises emerged with capability of mass production, including the Advanced Technology & Materials Co., Ltd. (at&m) (Beijing), Hunan Injection High Technology Co., Ltd (HIHT) (Changsha), Jin Zhu Pang injection manufacturing co., LTD. (Shandong), Fu Chi technology co., LTD. (Shanghai), etc.

In our laboratory at the Applied Mechanics department of FEMTO-ST institute, the

research team managed by Professor Jean-Claude Gelin and Professor Thierry Barriere has developed researches on micro processing and loaded polymers processing domain since 1995 [44, 45]. The conventional MIM and PIM have been carried out using various metallic or ceramic powders. The micro-MIM and bi-material MIM have also been investigated [6, 46]. Concerning the simulation of PIM, the FeaPIM© software has been adopted, in which a bi-phasic model was used to predict the powder segregation during the mold filling process [47]. In the same research group, studies have also been developed on solid state sintering, the activities have concerned experiments, modeling, simulation and optimization [48]. The research team in SWJTU of China also has more than 20 years' experiences in forming processes. Based on the same research background and target, the two research team from both French side and Chinese side began their cooperation in 1999. A chronology of the Ph. D. theses processed in both laboratories in the last years is given in the Fig. 1-12. The names of co-tutorial Ph. D. (Shi, Larsen, Song and Cheng) are set in the capital, bold and italic font.

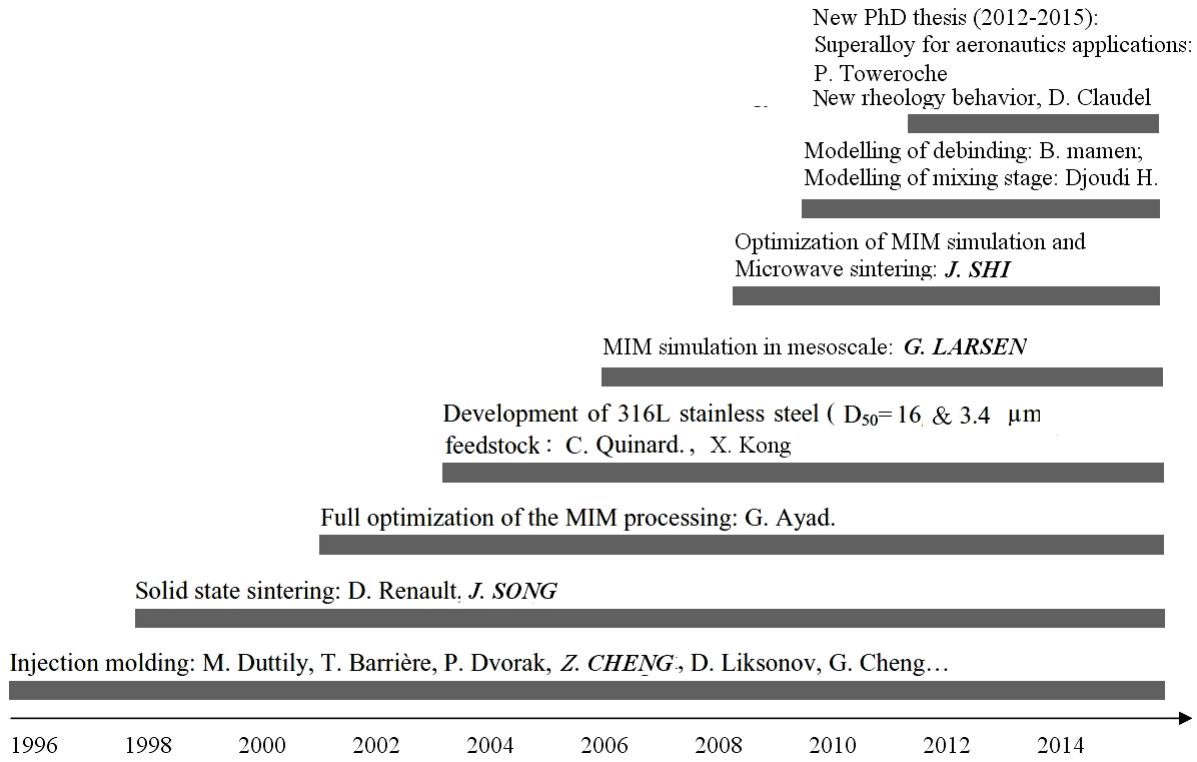

Fig. 1-12 Chronology of the Ph. D. theses processed in the French and Chinese research teams

Chapter 2 Developments of modified algorithms for Mold Filling Process

Powder Injection Molding is a new and advanced manufacturing technology. Numerical simulation plays an important role in its efficient applications. The analysis of injection molding was started by Spencer and Gilmore [49] in the early 1950s. Ballman et al [50] began to investigate one-dimensional rectangular flow in 1959. Analytical solutions for two-dimensional flow in a rectangular cavity were presented since the late 1970s [51-54]. Then large amounts of research works were done in detail on fountain flow [55, 56]. The implicit finite element method for simulation of the filling process was first tried by some authors [57-59]. It was found that the main barrier for filling flow model is the tremendous computational time due to the application of 3D finite element or finite difference method. Therefore, the explicit algorithms that improve the efficiency of simulation for injection flow model were studied and realized by Lewis and Gao, using MINI elements in 2D problems [60, 61]. The explicit algorithms with MINI element are much faster than the implicit ones. Their validity was proven by the experiments [45, 62]. For the sake of computational cost, a new explicit algorithm with fully vectorial operations was proposed by Liu [63]. The development is carried out by the research work of Cheng [64, 65]. By eliminating the global solutions in the previous explicit algorithm, it made successfully the computational cost to be about linearly proportional to the degree of freedom number. Based on this explicit algorithm, G. Larsen et al. [66] proposed a method combining finite element method and finite difference method for investigating the mono-injection case.

The performance of the new explicit vectorial algorithm has been evaluated by comparison with the results from both experiments and other numerical solvers, such as commercial software MPI software (Autodesk(C)). The fully vectorial feature of new algorithm provides the important advantage in computational cost for the simulation of large scale problems in industrial application. It is easy to be parallelized for the computation on a high performance system of multi-clusters. It was developed on the platform of Matlab (C) software and has improved the previous in-house software for simulation of the injection

filling process. However, it remains still some problems:

1) For some special cases when the phenomena of opposite joining and bi-pass are involved, inside which the flow directions subject to the sudden changes during the filling process, the present algorithm may result in untrue filling fronts. So modification is still required to improve the simulation of injection filling at some specific filling channels. This problem can be also seen in commercial FEM software MPI software (Autodesk$^{(C)}$).
2) The delay to fully fill the mold cavity when the filling process is close to be finished, meanwhile the filling front approaches to the outlet boundary, is remained in the developed solvers. This problem was mentioned in the doctoral thesis of Cheng [67], and left unsolved because of the absence of a suitable method to complete the boundary condition in the solution of advection equation for filling function. Also, the special modified outlet boundary conditions are required to make the in-house software more stable and more reliable.
3) How to extend the availability of present software into simulation of injection molding problems in micro scales. It needs a more comprehensive consideration of the mechanisms in mold injection. Some effects that can be ignore in macro size problems, such as surface tension, wall slip etc., will become remarkable behaviors for problems inmicron scales.

Work in this chapter is going to solve the first two problems mentioned above. And the third one will be discussed in the next chapter.

2.1 Modeling and Simulation of PIM injection

2.1.1 General Definition

As usually chosen, Eulerian description is adopted for simulation of the mold filling problems, which avoids the complicated and expensive remeshing procedures with Lagrangian description. The general definition of mold filling problems with surface tension is expressed as followings:

Let $t \in [0, t_f]$ be an instant in the injection course, in which t_f is the last moment f of filling process to reach the fully filled state. The sum of position $\boldsymbol{X}$ in the whole model is defined as set Ω. The set Ω in modeling of the injection molding consists of two different portions at each instant, the portion Ω_F filled by feedstock and the remained space Ω_V taken by the air. A field variable $\boldsymbol{F}(x,t)$ is defined to represent filling state of the model at different instants. This field variable takes value 1 to indicate the portion filled by feedstock and value 0 for the remained void portion, which contains in fact the atmosphere. The physical and geometrical definition for this modeling is shown in Fig. 2-1. In which Γ_I indicates inlet of the mold, Γ_O represents the outlet through it the air originally in the mold can be squeezed out during the injection. Γ_S stands for intersection of subsets Ω_F and Ω_V, which is in fact the filling front of the injection flow. V_I is the injected velocity on inlet boundary. P_O is the pressure on outlet boundary, which is set to be 0 in the present work to represent the environment pressure.

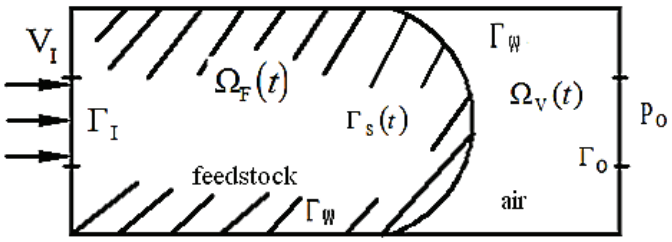

Fig. 2-1 Modeling of injection molding based on Eulerian description

The definitions for these subsets and their common surface are expressed in the following equations:

$$\forall\, t \in [0, T_f], \qquad \forall \mathbf{X} \in \boldsymbol{\Omega}$$

$$\boldsymbol{\Omega}^{\mathbf{F}} = \{\, \mathbf{X} \in \boldsymbol{\Omega}^{\mathbf{F}}(t) \;\big|\; F(\mathbf{X},t) = 1, \quad \boldsymbol{\Omega}^{\mathbf{F}}(t) \cup \boldsymbol{\Omega}^{\mathbf{V}}(t) = \boldsymbol{\Omega} \,\} \tag{2-1}$$

$$\boldsymbol{\Omega}^{\mathbf{V}} = \{\, \mathbf{X} \in \boldsymbol{\Omega}^{\mathbf{V}}(t) \;\big|\; F(\mathbf{X},t) = 0, \quad \boldsymbol{\Omega}^{\mathbf{F}}(t) \cup \boldsymbol{\Omega}^{\mathbf{V}}(t) = \boldsymbol{\Omega} \,\} \tag{2-2}$$

$$\boldsymbol{\Gamma}^{\mathbf{S}} = \{\, \mathbf{X} \in \boldsymbol{\Gamma}^{\mathbf{F}}(t) \;\big|\; \boldsymbol{\Gamma}^{\mathbf{S}}(t) = \boldsymbol{\Omega}^{\mathbf{F}}(t) \cap \boldsymbol{\Omega}^{\mathbf{V}}(t) \} \tag{2-3}$$

2.1.2 Governing Equations

To keep singleness of the solution strategy and simplicity of the software structure, under the frame of Eulerian description, the governing equations for filling flow are chosen the same for filled and void portion of the injection model, except that the physical parameters are chosen differently for these two domains. In fact, the interest of simulation is the filling flow of feedstock in mold cavity. For the portion filled by the feedstock, material properties are the real ones. To keep good stability of the simulation process, the material properties in void portion should to be modified to avoid too much of the difference compared to the ones in filled portion. In fact, the result of simulation in the void portion is not of our interest. So the parameters in the void portion can be chosen artificially to benefit the stable simulations. Nevertheless, for the analysis of temperature in solution of the energy conservation equation, the materials behaviors in both two portions should be the real ones, as we need evidently the correct temperature field in the whole mold cavity. The precondition to distinguish two different portions in the mold is to obtain the filling state field at each instant, which indicates whether or not the position is filled by the feedstock in the model.

2.1.2.1 Advection equation for filling state

The front position of filled domain is represented by the predefined filling state variable $\boldsymbol{F}(x,t)$. Some authors call it as the variable of pseudo concentration or fictive concentration [68, 69]. At each instant *t* in injection course, the evolution of filling state variable is dominated by an advection equation, driven by the velocity field.

$$\frac{\partial \boldsymbol{F}}{\partial \mathrm{t}} + \nabla \bullet (\boldsymbol{V}\,\boldsymbol{F}) = 0 \tag{2-4}$$

where V is the velocity vector, the boundary condition is $\boldsymbol{F} = 1$ on inlet of the mold. Its initial condition is $\boldsymbol{F} = 0$ everywhere in the mold except for the inlet surface.

2.1.2.2 Momentum conservation

Navier-Stokes equation is used to represent the momentum conservation. For two portions filled with different materials in the mold, it is expressed as:

$$\forall \mathbf{X} \in \mathbf{\Omega}^{\mathrm{F}},\ \rho_p\left(\frac{\partial \mathbf{V}}{\partial t} + \mathbf{V} \bullet \nabla \mathbf{V}\right) = -\nabla P + \nabla \bullet \boldsymbol{\sigma}'_p + \rho_p \mathbf{g} \tag{2-5}$$

$$\forall\ \mathbf{X} \in \mathbf{\Omega}^{\mathrm{V}},\ \rho_a\left(\frac{\partial \mathbf{V}}{\partial t} + \mathbf{V} \bullet \nabla \mathbf{V}\right) = -\nabla P + \nabla \bullet \boldsymbol{\sigma}'_a + \rho_a \mathbf{g} \tag{2-6}$$

where ρ_p is the polymer density in the filled mold cavity, whereas ρ_a is the air density in the unfilled mold cavity, P represents the hydraulic pressure field, $\boldsymbol{\sigma}'_p$ and $\boldsymbol{\sigma}'_a$ are the deviatoric Cauchy stress tensors in filled and void portion, $\mathbf{g}$ is the gravity vector.

As the flow in injection molding is often a problem with small Reynolds number, Sometimes the influence of advection effect is negligible compared to the viscous effect in Navier-Stokes equation. The momentum conservation can be then reduced to the solution of two distinct Stokes equations, expressed as:

$$\forall \mathbf{X} \in \mathbf{\Omega}^{\mathrm{F}},\ \rho_p \frac{\partial \mathbf{V}}{\partial t} = -\nabla P + \nabla \bullet \boldsymbol{\sigma}'_p + \rho_p \mathbf{g} \tag{2-7}$$

$$\forall\ \mathbf{X} \in \mathbf{\Omega}^{\mathrm{V}},\ \rho_a \frac{\partial \mathbf{V}}{\partial t} = -\nabla P + \nabla \bullet \boldsymbol{\sigma}'_a + \rho_a \mathbf{g} \tag{2-8}$$

It should be mentioned that the material properties for air portion are chosen different from their true values, for the purpose to keep numerical stability. Because of singleness of the solution scheme for two different portions, it may result in the instability in numerical solution if the mass and viscosity in void portion are too much different from the ones in filled portion. However, the exact flow in void portion is not our interest. The result of such a numerical treatment is acceptable, as our main objective is the flow of injected feedstock.

The boundary condition should be imposed for each variable in the solution process. The mold inlet Γ_{I} can be specified by a prescribed velocity $\overline{\mathbf{V}}$ or imposed pressure $\overline{\mathrm{P}}$. On the mold outlet Γ_{O}, one needs simply to impose a zero pressure, assigned to atmosphere

pressure. For the boundary conditions on the mold walls $\mathbf{\Gamma}^{\mathbf{W}}$, the velocity in normal direction is always imposed to zero. A tangent viscous load $\mathbf{f}$ could be specified for frictional sliding conditions. This tangential load is generally expressed in Chezy's form as [60]:

$$\forall \mathbf{X} \in \mathbf{\Gamma}^{\mathbf{W}}, \quad \mathbf{V} \bullet \vec{\mathbf{n}} = 0, \quad \mathbf{f} = - \ C_f^{-2} \rho \ \left| \ \mathbf{V} \bullet \vec{\mathrm{t}} \ \right| \ \mathbf{V} \bullet \vec{\mathrm{t}} \tag{2-9}$$

where $\vec{\mathbf{n}}$ is the unit of outward normal, $\vec{\mathbf{t}}$ is the unit vector of local tangent , C_f is a coefficient to be determined by experiments. For the sticking condition, the tangent velocity is also specified to be zero as the normal one.

2.1.2.3 Incompressibility condition

Incompressibility condition should be satisfied in the portion filled by feedstock:

$$\forall \ \mathbf{X} \in \mathbf{\Omega}^{\mathbf{F}}, \quad \nabla \bullet \mathbf{V} = 0 \tag{2-10}$$

where $\mathbf{V}$ is the vector which represents the velocity field. Different from the method developed previously in research team with MINI elements [70], incompressibility in the new explicit algorithm [67] is to be kept only in the filled portion. The same numerical operation is used in the void portion to keep simplicity and singleness of the solution procedure, expect that the parameters in the void portion are not chosen attentively to maintain a strict incompressibility. In fact, these parameters in void portion is adjusted preferably to keep stability of the numerical solution, rather than to maintain the exact incompressibility. As mentioned above, the result in void mold portion is not of our interest but just the need for solution of the injection molding problems under Eulerian description.

2.1.2.4 Energy conservation

The viscous law of feedstock is strongly dependent on the local temperature values. The variation of temperature field is very important to determine the flow of viscous feedstock So it is necessary to evaluate the temperature field during the simulation of mold injection filling process. Once the feedstock is considered as isotropic and the Fourier model for heat

flux is applied, the heat transfer is governed by the following advective-diffusive equation:

$$\forall \mathbf{X} \in \mathbf{\Omega}^{\mathrm{F}},\ \rho_p C_p\ (\frac{\partial T}{\partial t} + \mathbf{V} \bullet \nabla T) = k_p \Delta T\ +\ \boldsymbol{\sigma}_p^{'} : \dot{\boldsymbol{\varepsilon}}_p \tag{2-11}$$

$$\forall \mathbf{X} \in \mathbf{\Omega}^{\mathrm{V}},\ \rho_a C_a\ (\frac{\partial T}{\partial t} + \mathbf{V} \bullet \nabla T) = k_a \Delta T\ +\ \boldsymbol{\sigma}_a^{'} : \dot{\boldsymbol{\varepsilon}}_a \tag{2-12}$$

where $\boldsymbol{\sigma}_p^{'} : \dot{\boldsymbol{\varepsilon}}_p$ and $\boldsymbol{\sigma}_a^{'} : \dot{\boldsymbol{\varepsilon}}_a$ stand for the dissipations associated to viscous PIM flow and viscous air flow, T stands for the temperature field in the mold, C_p and k_p are respectively the specific heat and thermal conductivity coefficient of the feedstock, C_a and k_a are respectively the specific heat and thermal conductivity coefficient of air, $\dot{\boldsymbol{\varepsilon}}_p$ and $\dot{\boldsymbol{\varepsilon}}_a$ are the strain rate in filled and void portions. The boundary conditions are generally defined with prescribed temperature values $T = \overline{T}$ on mold's walls. The ambient temperature $\overline{T}^a$ may be imposed on the outlet Γ^{O}. The convection effects can also be considered on the mold walls of filled and void portions with relationships $q = h_p(T - \overline{T})$ and $q = h_a(T - \overline{T})$, in which h_p and h_a are the heat transfer coefficient of feedstock and air.

2.1.3 Explicit algorithm for simulation

The implicit algorithms are often used to solve the problems by finite element method. But these algorithms lead to very expensive simulation even for 2D problems. The present dissertation uses the explicit algorithm developed in research team [67, 70, 71] for simulation of the mold filling problems with only vectorial operations in global sense. Neither the global solution nor the construction of global matrix is required in the newly realized in-house software. An important feature of the new algorithm is the use of elements with equal order interpolations. The interpolations of velocity and pressure field have the same order of interpolation, different from the traditionally used MINI elements for simulation of the incompressible flow. Actually in the new explicit algorithm, the triangle elements in 2D case

and tetrahedral elements in 3D case are employed, as shown in Fig. 2-2. To mesh the models of intricate geometry, they represent less degrees of freedom and better fitness than the quadrangle and hexahedral elements [72].

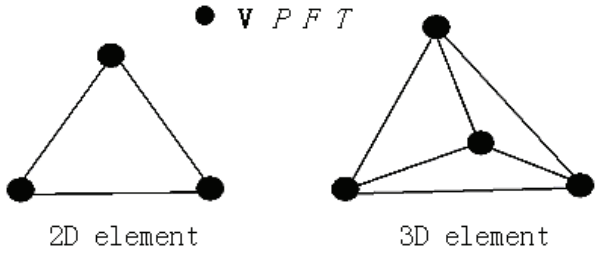

Fig. 2-2 Elements used in new algorithm

The interpolations of different variables are represented at the element level as:

$$\{\mathbf{V},\quad P,\quad F,\quad T\}=\sum_{i=1}^{m}\mathbf{N}_i\ \{\mathbf{V}_i,\quad P_i,\quad F_i,\quad T_i\} \tag{2-13}$$

where m is the node number in such an element for different variables, $\mathbf{N}_i$ is the interpolation functions, $\mathbf{V}_i$ represents the nodal vector values of velocity field. Other notations as P_i, F_i and T_i represent the nodal scalar values of the pressure, filling state and temperature field.

As an explicit algorithm is used, most of the operations in fractional steps are the same as in the previous work [70], while a special strategy is developed by Cheng [67] to verify the incompressibility condition. This advance eliminates all the global operation in simulation. In global sense, only the vectorial operations are performed so that high efficiency can be achieved for further industrial application of the filling simulation. Moreover, it provides a strong facility for computational parallelization on a multi-cluster system. The fractional steps to solve the variable fields of filling state, velocity and temperature are performed in the following manners, according to the dissertation of Cheng [67].

2.1.3.1 Determination of filling states

The determination of filled domain is the premise for other operations in Eulerian description, as different material properties should be assigned in filled and void portions

respectively. The filling state variable F defined to trace the filling front is determined by an advection equation (Eq. 2-4). The numerical solution for the advection equation associated to the filling state employs the same scheme as in polymer injection simulation. For sake of the stability, the solution is based on Taylor-Galerkin method [73]. Solution procedure of the filling state is the same as in the previous work [70]. It is then just a short mention of the method and the necessary explanation.

The time differential of variable F in discretized form can be expressed by the development of Taylor series:

$$\frac{(F_{n+1}-F_n)}{\Delta t}=\frac{\partial F_n}{\partial t}+\frac{\Delta t}{2}\frac{\partial^2 F_n}{\partial t^2}+O(\Delta t)^2 \tag{2-14}$$

in which F_n and F_{n+1} represent the filling state at time step t_{n+1} and t_n, Δt stands for the time increment.

The governing equation (Eq. 2-4) can lead to the follow relationship by an approximation $\partial \mathbf{V}/\partial t=(\mathbf{V}_{n+1}-\mathbf{V}_n)/\Delta t$:

$$\begin{aligned}\frac{\partial F_n}{\partial t}&=-\ \mathbf{V}\bullet\nabla F_n\\ \frac{\partial^2 F_n}{\partial t^2}&=\mathbf{V}\bullet\nabla\ (\ \mathbf{V}\bullet\nabla F_n)-\frac{(\mathbf{V}_{n+1}-\mathbf{V}_n)}{\Delta t}\bullet\nabla F_n\end{aligned} \tag{2-15}$$

The weak form of Eq. 2-14 can be then written as:

$$\int_\Omega f^*\frac{(F_{n+1}-F_n)}{\Delta t}\ d\Omega=-\int_\Omega f^*\mathbf{V}_{n+1/2}\bullet\nabla F_n\ d\Omega+\frac{\Delta t}{2}\int_\Omega f^*\mathbf{V}\bullet\nabla\ (\ \mathbf{V}\bullet\nabla F_n)\ d\Omega \tag{2-16}$$

where $\mathbf{V}_{n+1/2}=(\mathbf{V}_{n+1}+\mathbf{V}_n)/2$, f^* is a kinematically admissible field associated to variable F.

The discretized form of Eq. 2-16 by finite element method can be written as:

$$\mathbf{M}_0\ \frac{\mathbf{F}_{n+1}\ -\ \mathbf{F}_n}{\Delta\ t}=-\ [\mathbf{K}^{ad}(\mathbf{V}_{n+1/2})\ +\ \mathbf{K}^{df}(\mathbf{V}_n)\ ]\ \mathbf{F}_n \tag{2-17}$$

where $\mathbf{M}_0$ is a lumped pseudo matrix, $\mathbf{K}^{ad}(\mathbf{V})$ is a stiffness matrix represents the advection effect, while $\mathbf{K}^{df}(\mathbf{V})$ is a stiffness matrix stands for diffusion effect. These terms take respectively the following forms:

$$\mathbf{M}_0 = \underset{\Omega}{A} \int_{\Omega^e} \mathbf{N}^T \ \mathbf{N} \ d\mathbf{\Omega} \tag{2-18}$$

$$\mathbf{K}^{ad}(\mathbf{V}_{n+1/2}) = \underset{\Omega}{A} \int_{\Omega^e} \mathbf{N}^T \mathbf{V}_{n+1/2}^T \mathbf{G} \ d\mathbf{\Omega} \tag{2-19}$$

$$\mathbf{K}^{df}(\mathbf{V}_n) = \frac{\Delta t}{2} \underset{\Omega}{A} \int_{\Omega^e} \mathbf{G}^T \mathbf{V}_n^T \mathbf{V}_n \mathbf{G} \, d\mathbf{\Omega} \tag{2-20}$$

in above expression, A represents the assembling operation in finite element method, $\mathbf{N}$ is the matrix of interpolation functions in each element for filling state variables, $\mathbf{V}_{n+1}$ and $\mathbf{V}_n$ are the values obtained at time step t_{n+1} and t_n, $\mathbf{V}_{n+1/2} = (\mathbf{V}_n + \mathbf{V}_{n+1})/2$, $\mathbf{G}$ is a gradient operator constructed by derivatives of the interpolation functions:

$$\nabla F = \mathbf{G}F \tag{2-21}$$

This solution is consisted of only local and explicit operations, so the prediction is very efficient.

2.1.3.2 Solution of momentum conservation

Momentum conservation of the viscous flow is represented by Navier-Stokes equation with consideration of the incompressibility condition. As an explicit algorithm, the computation is fractionalised into three consequent steps [74]: solution for the effect of advection, viscous diffusion and incompressibility condition, so Eq. 2-7 and Eq. 2-8 can be decomposed into an advection equation, a viscous diffusion equation and an equation to verify the incompressibility condition:

$$\forall \mathbf{X} \in \mathbf{\Omega}, \ \frac{\partial(\mathbf{V}_{n+} - \mathbf{V}_n)}{\partial t} = -\mathbf{V}_n \bullet \nabla \mathbf{V}_n \tag{2-22}$$

$$\forall \mathbf{X} \in \mathbf{\Omega}^{\mathbf{F}}, \ \rho_p \frac{\partial(\mathbf{V}_{n++} - \mathbf{V}_{n+})}{\partial t} = \nabla \bullet \boldsymbol{\sigma}'_p + \rho_p \mathbf{g} \tag{2-23}$$

$$\forall \mathbf{X} \in \mathbf{\Omega}^{\mathrm{V}},\ \rho_a \frac{\partial(\mathbf{V}_{n++} - \mathbf{V}_{n+})}{\partial t} = \nabla \bullet \boldsymbol{\sigma}'_a + \rho_a \mathbf{g} \tag{2-24}$$

$$\forall \mathbf{X} \in \mathbf{\Omega}^{\mathrm{F}},\ \rho_p \frac{\partial(\mathbf{V}_{n+1} - \mathbf{V}_{n++})}{\partial t} = -\nabla P \tag{2-25}$$

$$\forall \mathbf{X} \in \mathbf{\Omega}^{\mathrm{V}},\ \rho_a \frac{\partial(\mathbf{V}_{n+1} - \mathbf{V}_{n++})}{\partial t} = -\nabla P \tag{2-26}$$

where $\mathbf{V}_n$ and $\mathbf{V}_{n+1}$ are the velocity fields at instant t_n and t_{n+1}, $\mathbf{V}_{n+}$ and $\mathbf{V}_{n++}$ are the intermediate velocity fields used in the fractional steps.

1) Solution of the advection effect

Generally the advection effect in Navier-Stokes equation is neglected to reduce the equation into a Stoke one [70, 71] because the small Reynolds number in injection flow. To solve the advection equation with a vectorial variable, it is however more complex than the solution of advection equation for filling state variable, in which the variable is only a scalar one. The advection effect in momentum conservation is also solved by Taylor-Galerkin method. The time differential of velocity in discretized form can be expressed by the Taylor series development as:

$$\forall \mathbf{X} \in \mathbf{\Omega},\ \frac{(\mathbf{V}_{n+1} - \mathbf{V}_n)}{\Delta t_n} = \frac{\partial \mathbf{V}_n}{\partial t} + \frac{\Delta t_n}{2} \frac{\partial^2 \mathbf{V}_n}{\partial t^2} + O(\Delta t_n)^2 \tag{2-27}$$

After discretization by finite element method, Eq. 2-22 can be written in the following form:

$$\begin{aligned} \forall \mathbf{X} \in \mathbf{\Omega},\ \mathbf{M}\ \frac{(\mathbf{V}_{n+} - \mathbf{V}_n)}{\Delta t_n} = &-\ (1 + \frac{\Delta t_n}{\Delta t_{n-1}})\ \mathbf{K}^{ad}(\mathbf{V}_n)\ \bullet \mathbf{V}_n \\ &+ \frac{\Delta t_n}{2\Delta t_{n-1}} \mathbf{K}^{ad}(\mathbf{V}_{n-1}) \bullet \mathbf{V}_n + \frac{\Delta t_n}{2\Delta t_{n-1}} \mathbf{K}^{ad}(\mathbf{V}_n) \bullet \mathbf{V}_{n-1} \end{aligned} \tag{2-28}$$

where $\mathbf{M}$ is the mass matrix lumped into diagonal form, Δt_{n-1} and Δt_n are the time increments at instant t_{n-1} and t_n, $\mathbf{V}_{n-1}$ is the velocity fields at instant t_{n-1}, $\mathbf{K}^{adv}(\mathbf{V})$ is

a stiffness operator that represents the advection effects in Navier-Stokes equation. These terms take respectively the follow forms:

$$\forall \mathbf{X}\in\mathbf{\Omega}^{\mathbf{F}},\ \mathbf{M}=\underset{\Omega^F}{A}\int_{\Omega^e}\rho_p\ (\mathbf{N})^T\ \mathbf{N}\,d\mathbf{\Omega} \tag{2-29}$$

$$\forall \mathbf{X}\in\mathbf{\Omega}^{\mathbf{V}},\ \mathbf{M}=\underset{\Omega^V}{A}\int_{\Omega^e}\rho_a\ (\mathbf{N})^T\mathbf{N}\,d\mathbf{\Omega} \tag{2-30}$$

$$\forall \mathbf{X}\in\mathbf{\Omega}^{\mathbf{F}},\ \mathbf{K}^{adv}(\mathbf{V})=\underset{\Omega^F}{A}\int_{\Omega^e}\rho_p\ (\mathbf{N})^T(\mathbf{G}\ \mathbf{V}^e)\ \mathbf{N}\,d\mathbf{\Omega} \tag{2-31}$$

$$\forall \mathbf{X}\in\mathbf{\Omega}^{\mathbf{V}},\ \mathbf{K}^{adv}(\mathbf{V})=\underset{\Omega^V}{A}\int_{\Omega^e}\rho_a\ (\mathbf{N})^T(\mathbf{G}\ \mathbf{V}^e)\ \mathbf{N}\,d\mathbf{\Omega} \tag{2-32}$$

in the above expression, A represents the assembling operation in finite element method, $\mathbf{V}^e$ represents the vector that contains the velocity components at all nodes in an element. The gradient operator $\mathbf{G}$ should be built according to the arrangement of velocity values in its vector $\mathbf{V}^e$. So at each Gauss point of the element, one has the relationship:

$$\nabla\mathbf{V}=\mathbf{G}\ \mathbf{V}^e \tag{2-33}$$

2) Solution of the viscous diffusion effect

By Galerkin method, Eq. 2-23 and 2-24 can be discretized in the following form:

$$\forall \mathbf{X}\in\mathbf{\Omega},\ \mathbf{M}\frac{(\mathbf{V}_{n++}-\mathbf{V}_{n+})}{\Delta t}=\mathbf{F}^{\sigma}(\mathbf{V}_n)+\mathbf{F}^{ext} \tag{2-34}$$

where $\mathbf{M}$ is the mass matrix in the form of Eq. 2-29 and 2-30, $\mathbf{F}^{\sigma}$ is the viscous diffusion term, $\mathbf{F}^{ext}$ is the load vector with gravity contribution and boundary conditions. They are numerically defined as:

$$\forall \mathbf{X}\in\mathbf{\Omega},\ \mathbf{F}^{\sigma}(\mathbf{V})=\underset{\Omega}{A}\int_{\Omega^e}(\mathbf{B})^T\mathbf{\sigma}'\,d\mathbf{\Omega} \tag{2-35}$$

$$\forall \mathbf{X}\in\mathbf{\Omega}^{\mathbf{F}},\ \mathbf{F}^{ext}=\underset{\Omega^F}{A}\int_{\Omega^e}(\mathbf{N})^T\rho_p\ \ \mathbf{g}\ d\Omega+\mathbf{f}^{ext} \tag{2-36}$$

where A represents the assembling operator in finite element method, $\mathbf{B}$ is the matrix of derivatives of the interpolation functions $\mathbf{N}$ in an element, defined to calculate the symmetric part of velocity's gradient $\dot{\mathbf{\varepsilon}}=\mathbf{B}\mathbf{V}^e$, $\mathbf{V}^e$ represents the nodal values of velocity vectors in an element, $\mathbf{\sigma}'$ stands for the deviator of Cauchy stress tensor. This stress

deviator should be calculated on the deviator of the strain rate, by means of different viscous laws defined distinctly in the filled and void portion, $\mathbf{f}^{ext}$ stands for the surface loads converted to the nodes on boundary. In the void portion, $\mathbf{F}^{ext}$ is generally set to be 0, as the gravity effect of air can be ignored and pressure imposed on outlet is 0.

3) Incompressibility

The new strategy for verification of the incompressibility condition is the most important feature of the newly algorithm. It eliminates the last global solution in explicit algorithms to realize the fully vectorial computations. The incompressibility is maintained by a feedback correction procedure, which avoids the direct evaluation of pressure fields. In the new vectorial algorithm, Eq. 2-25 and 2-26 are replaced by the following equations for the corrections to obtain the velocity field that satisfies the incompressibility condition.

$$\forall \mathbf{X} \in \mathbf{\Omega}^{\mathbf{F}}, \quad \rho_p \frac{\partial(\mathbf{V}_{n+1} - \mathbf{V}_{n++})}{\partial t} = -\nabla \bullet [\lambda^F (\nabla \bullet \mathbf{V}_{n++}) \mathbf{I}] \tag{2-37}$$

$$\forall \mathbf{X} \in \mathbf{\Omega}^{\mathbf{V}}, \quad \rho_a \frac{\partial(\mathbf{V}_{n+1} - \mathbf{V}_{n++})}{\partial t} = -\nabla \bullet [\lambda^V (\nabla \bullet \mathbf{V}_{n++}) \mathbf{I}] \tag{2-38}$$

Incompressibility condition $\nabla \bullet \mathbf{V}_{n+1} = 0$, as shown in Eq. 2-10, is satisfied by a corrective term with factor λ^{F} and λ^{V}. Such a special term is used to substitute the term of pressure gradient in Eq. 2-25 and 2-26.

Eq. 2-25 and 2-26 can be discretized by Galerkin finite element method, which results in the solution of velocity field $\mathrm{V}_{\mathrm{n+1}}$ in the following form:

$$\forall \mathbf{X} \in \mathbf{\Omega}, \ \mathrm{i} \in \{\mathrm{F}, \mathrm{V}\}, \ \mathbf{M} \frac{(\mathbf{V}_{n+1} - \mathbf{V}_{n++})}{\Delta t} = \mathbf{F}^d(\lambda^i_{n+1}, \mathbf{V}_{n++}) \tag{2-39}$$

where $\mathbf{M}$ is the mass matrix in form of Eq. 2-29 and 2-30, the variables $\mathbf{V}_{n+1}$ and $\mathbf{V}_{n++}$ represent the final incompressible velocity and intermediate velocity fields, $\mathbf{F}^{\mathrm{d}}$ is the term for correction of the incompressibility.

Determination of the coefficient λ^{F}, λ^{V} and the correction term $\mathbf{F}^{\mathrm{d}}$ will not be

described in detail here. It belongs to the main work of Cheng [64, 67].

2.1.3.3 Calculation of heat transfer and temperature field

The heat transfer in Eq. 2-11 and 2-12 is dealt with both advection and diffusion effects. A fractional step method proposed by Lewis [61] is used in the present work as it permits to evaluate the temperature field explicitly. The fractional advection and diffusion steps are written as:

$$\forall \mathbf{X} \in \mathbf{\Omega}, \quad \frac{\partial (T_{n+} - T_n)}{\partial t} = -\mathbf{V} \bullet \nabla T \tag{2-40}$$

$$\forall \mathbf{X} \in \mathbf{\Omega}^{\mathrm{F}}, \quad \frac{(T_{n+1} - T_{n+})}{\partial t} = \frac{1}{\rho_p C_p} (k_p \Delta T_{n+} + \boldsymbol{\sigma}'_p : \dot{\boldsymbol{\varepsilon}}_p) \tag{2-41}$$

$$\forall \mathbf{X} \in \mathbf{\Omega}^{\mathrm{V}}, \frac{(T_{n+1} - T_{n+})}{\partial t} = \frac{1}{\rho_a C_a} (k_a \Delta T + \boldsymbol{\sigma}'_a : \dot{\boldsymbol{\varepsilon}}_a) \tag{2-42}$$

where T_n and T_{n+1} are the temperature fields at instant t_n and t_{n+1}, T_{n+} is an intermediate temperature field used in the fractional step method.

Same as for the evaluation of filling state by Taylor-Galerkin method, Eq. 2-40 can be discretized in following form:

$$\forall \mathbf{X} \in \mathbf{\Omega}, \quad \mathbf{M}_0 \frac{(\mathbf{T}_{n+} - \mathbf{T}_n)}{\Delta t} = -\left[\mathbf{K}^{ad}(\mathbf{V}) + \mathbf{K}^{df}(\mathbf{V})\right] \mathbf{T}_n \tag{2-43}$$

where $\mathbf{M}_0$ is a lumped pseudo matrix in the form of Eq. 2-18, $\mathbf{K}^{\mathrm{ad}}(\mathrm{V})$ is a stiffness matrix of the advection effect in the form of Eq. 2-19, while $\mathbf{K}^{\mathrm{df}}(\mathrm{V})$ is a stiffness matrix of the diffusion effect in the form of Eq. 2-20.

By Galerkin method, the solution of Eq. 2-41 and 2-42 can be written in the following manner:

$$\forall \mathbf{X} \in \mathbf{\Omega}, \quad \mathbf{M}_0 \frac{(\mathbf{T}_{n+1} - \mathbf{T}_{n+})}{\Delta t} = \mathbf{K}^d \mathbf{T}_{n+} + \dot{\mathbf{Q}} + \mathbf{q}^c \tag{2-44}$$

where $\mathbf{M}_0$ takes the same form as in Eq. 2-18, $\mathbf{K}^{\mathrm{d}}$ is the thermal diffusion term, $\dot{\mathbf{Q}}$ is

the heat dissipation term, $\mathbf{q}^c$ is the heat convection term. These terms can be deduced from the following forms:

$$\forall \mathbf{X} \in \mathbf{\Omega^F}, \quad \mathbf{K}^d = \frac{k_p}{\rho_p C_p} \underset{\Omega^F}{A} \int_{\Omega^e} \mathbf{G}^T \mathbf{G} \; d\mathbf{\Omega} \tag{2-45}$$

$$\forall \mathbf{X} \in \mathbf{\Omega^V}, \quad \mathbf{K}^d = \frac{k_a}{\rho_a C_a} \underset{\Omega^V}{A} \int_{\Omega^e} \mathbf{G}^T \mathbf{G} \; d\mathbf{\Omega} \tag{2-46}$$

$$\forall \mathbf{X} \in \mathbf{\Omega^F}, \quad \dot{\mathbf{Q}} = \frac{1}{\rho_p C_p} \underset{\Omega^F}{A} \int_{\Omega^e} \mathbf{N}^T (\boldsymbol{\sigma}_p^{'} : \dot{\boldsymbol{\varepsilon}}_p)^e \; d\mathbf{\Omega} \tag{2-47}$$

$$\forall \mathbf{X} \in \mathbf{\Omega^V}, \quad \dot{\mathbf{Q}} = \frac{1}{\rho_a C_a} \underset{\Omega^V}{A} \int_{\Omega^e} \mathbf{N}^T (\boldsymbol{\sigma}_a^{'} : \dot{\boldsymbol{\varepsilon}}_a)^e \; d\mathbf{\Omega} \tag{2-48}$$

$$\forall \mathbf{X} \in \mathbf{\Omega^F}, \quad \mathbf{q}^c = \underset{\Gamma^q}{A} \int_{\Gamma^q} \mathbf{N}^T h_p \, (T_{n+} - \overline{T}) \; dS \tag{2-49}$$

$$\forall \mathbf{X} \in \mathbf{\Omega^V}, \quad \mathbf{q}^c = \underset{\Gamma^q}{A} \int_{\Gamma^q} \mathbf{N}^T h_a \, (T_{n+} - \overline{T}) \; dS \tag{2-50}$$

where $\mathbf{G}$ is a gradient operator in the form of Eq. 2-21, $(\boldsymbol{\sigma}_p^{'} : \dot{\boldsymbol{\varepsilon}}_p)^e$ and $(\boldsymbol{\sigma}_a^{'} : \dot{\boldsymbol{\varepsilon}}_a)^e$ are the values calculated at each Gauss point on the basis of obtained velocity field $\mathbf{V}_{n+1}$ and prescribed flow behaviour in filled and void portions respectively, h_p and h_a are the heat exchange coefficients of feedstock and air with the mold boundary, $\overline{T}$ is the temperature values on the mold walls.

2.2 Algorithm for improvement of wrongly adverted filling profile

With the development of injection molding process, shape of the components is increasingly complex [75]. Due to the constraints in physical experiments and the availability of measurements for micro-scale factors, the accurate numerical simulation becomes more and more important in designing and manufacturing. In general, Eulerian description is used for simulation of the filling flow problems [76, 77]. The mold die cavity is assumed occupied

by two different flow substances, viscous polymer in the filled portion and air in the remained void part. A filling state variable $\boldsymbol{F}(x,t)$ is used to describe the evolution of filling process, as the definition in section 2.1.1. The governing equation for filling state takes the form of an advection equation (Eq. 2-4). The evolution of filling state is governed by the velocity field in whole mold cavity.

However for some cases, it is observed that the filling patterns predicted by simulation are not the realistic ones, especially when the phenomena of opposite joining and bi-pass are involved. In most cases, the filling flow direction doesn't change dramatically. The velocity field in void portion close to filling front is similar to that of the polymer behind the filling front. So according to the traditional mechanical model of injection filling process, as described in chapter 2, it will often result in an accurate and realistic simulation. But it is not so good for some special cases when the opposite joining and bi-pass are involved, such as runners in shapes of ⊥ and L, inside which the flow directions subject to the sudden changes in the filling runners. At this instance, the untrue results may be produced, as shown in Fig. 2-3. The simulations are carried out using Matlab (C) software. The modeling algorithm is based on the same principle as the previous work done by Barriere [70] and Cheng [67, 70]. The related material properties are listed in table 2-1. These material properties and boundary conditions are assigned just for the purpose of software validation. They do not mean the real values obtained from experiments.

Table 2-1 Material properties and parameters used in numerical simulations

Parameter	value
Feedstock:	Polymer (PP)
Density:	1 g/cm^3
Viscosity of the mixture:	100 Pa.s (constant viscosity)
Injection rate:	20 cm^3/s
Injected velocity:	0.1 m·s^{-1} (constant velocity)
Boundary condition:	sticky wall (no-slip on the wall)

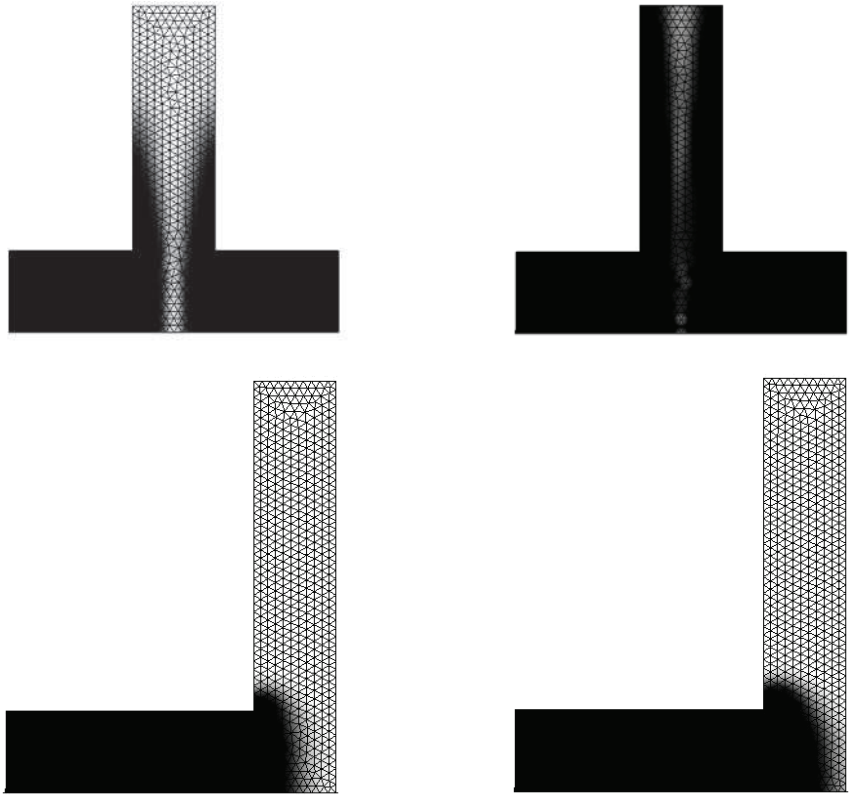

Fig. 2-3 Filling problems of front joining for specific die cavities in shap ⊥ and L

For the case of runner in shape ⊥, the polymer is injected from two inlets in opposite sides of the cavity. The same injected velocities (as inlet boundary condition) are imposed in both inlets. The two different filling fronts with the same speed should independently progress in the mold die cavities, and then meet to each other to reach a common outlet. However, in Fig. 2-3, it is observed that the filling fronts get the way to bi-pass before them merging together at the middle of bottom in ⊥ cavity. There exists an air gap between the two evolving fluid fronts that is not completely filled at the end of simulation. For the case of runner in shape L, after the polymer being horizontally injected into the mold die cavity, it should arrive mainly at the right hand side wall first, and then moving into the vertical part of the cavity. But the same untrue phenomenon happens.

As another example, the simulation result made by commercial finite element software MPI software (Autodesk$^{(C)}$) is introduced, as shown in Fig. 2-4. It uses the same material and boundary conditions as the example in Fig. 2-3. The related material properties can be referred to table 2-1. It can be found that in the filling of a typical runner in shape ⊥, the filling fronts from two opposite inlets got their own way to the middle bi-pass before they

joined together. Evidently this result doesn't meet the real physical phenomenon. Although the running of software uses some strategy to modify this problem in post-processing steps, but the filling patterns are not yet the true ones for the two opposite filling fronts to join together.

Fig. 2-4 Simulation by MPI software (Autodesk(C)), front joining in mold cavity of shape ⊥ with opposite inlets

G. Larsen et al. [66] used the Streamline Upwind Petrov Galerkin method (SUPG) to improve this filling problem, and confirmed that the simulation results are more close to the real situation than the ones by Taylor-Galerkin method [67, 70, 78]. However, the real pattern of front joining in injection molding had not been exactly predicted, as shown in Fig. 2-5.

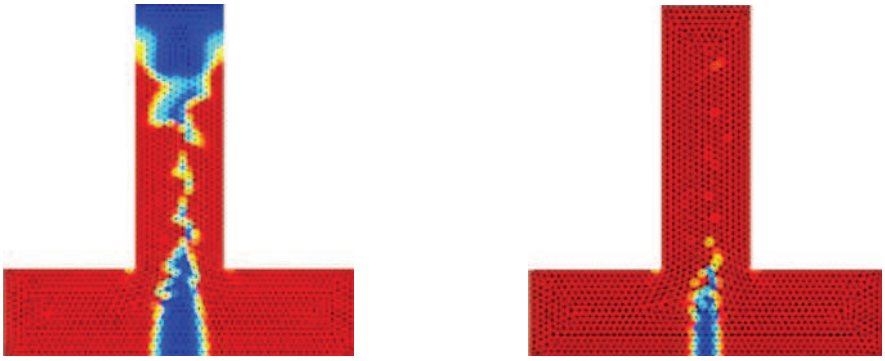

Fig. 2-5 The improved but still untrue results by SUPG method [66]

The objective of present study is to analyze the source for the untrue simulation results and find the effective way to settle the problem. A modified algorithm, which is similar to upwind method, was proposed to trace the filling front. This proposed method makes the advection of filling state be mainly affected by the filling flow behind the filling front. Based on finite element method and the efficient vectorial explicit algorithm developed in research

team, a systematic operation was proposed for modifying the velocity field ahead filling front, making the advance pattern of flow front be guided more on the flow of the polymer instead of the fictive air flow. The simulation results in shapes of ⊥ and L show that the proposed algorithm can effectively improve the untrue filling patterns in simulation.

2.2.1 The source for distorted simulation results

The filling processes may be distorted in simulation by the following sources:

1) Differences in physical properties of the polymer and air not being taken into account in governing equation of the filling evolution

Eulerian description is used for simulation of the injection molding process. The filling state variable is governed by advection equation to track the filling fronts. As in Eq. 2-4, it doesn't distinguish the different effects of the polymer and air on advance of the filling front. Due to extreme difference in the nature of these two substances, their effects to evolution of the filling front are extremely different, too. In fact, as an incompressible fluid, the advance of filling front is mainly driven by the flow of polymer behind it, and rarely guided by the air flow ahead. But the variable of filling state $\boldsymbol{F}$ is advected by the velocity field in whole mold cavity in simulation. It means that the velocity ahead and behind the filling front represent the equal effect on advance of the filling front. But in fact, the gradient of pressure is built-up mainly in the flow of polymer, rather than in the air flow. The flow of air has much less effect on the advance of polymer filling front.

2) Artificial air properties taken in simulation

As Eulerian description is used for injection molding, a filling state variable governed by advection equation is defined to track the filling fronts. The void portion in mold is supposed to be filled by a fictive fluid to simplify the procedures. Under the frame of Eulerian description and in order to keep integrity and consistency of the solution scheme, air in the void portion is also assumed to be incompressible as the polymer. By doing this strategy, the computation of both filled cavity and void portion can be implemented with the unique numerical operation. However, the incompressible assumption for the air flow is not

really consistent with its true nature. Such an assumption may affect also on the advance of filling front, other than its virtue to simply the solution algorithm.

Besides that, the flow of materials in both filled and unfilled portions (air flow) should satisfy the conservation of momentum. In Eq. 2-5 & 2-6, it can be noticed that in these two parts, the same Navier-Stocks equation has been used, except that different material parameters are assigned. The large difference in the natures of the polymer and air may result in numerical instability. So increasing artificially the mass and viscosity of air becomes a common practice to keep stability of the numerical simulation. Then the inaccurate air flow may affect advance of the filling front, leading the simulation results to be distorted. It is another factor to produce the distortion in simulation of the front tracking.

According to the analysis on the cause of distortion for front tracking, the problem is then how to make the advection of filling state function depends more on the flow behind the front, less on the flow of air ahead of the front.

2.2.2 Modification of the solution procedure

Based on the mechanical model and the notion of upwind method to strengthen the influences of the polymer flow located behind the filling front, a notion similar to upwind method was introduced. A corresponding correction method was proposed to settle the distortion of filling front mentioned above. A feasible way to make the filling pattern more realistic is to modify the velocity field near the filling front. Advance of the filling front can be made to follow the guidance of polymer flow behind it, if the velocity just before the front is set to be similar to that behind the front. By means of a systematic operation to modify the velocity field for filling simulation, the untrue impact of air flow, represented by the velocity field ahead of the filling fronts, can be reduced. To implement such method, there exist two key issues to be solved:

First question: how to determine the band to be modified, ahead of the filling front?

The selection can be made by the unit of element, judging and selecting element by element. Then the question is turned to be: which elements locate in the band close to filling front? And what is the criterion to judge if an element is in the band?

In fact, according to the definition of field variable $\boldsymbol{F}(x,t)$, it takes the value $\boldsymbol{F}$ =0 to indicate void portion while $\boldsymbol{F}$ =1 represents the filled one inside the mold cavity. Then the nodes near filling front should represent the values between 0 and 1, note that $\boldsymbol{F}_{\text{Frt}}$, $0<\boldsymbol{F}_{\text{Frt}}<1$. One can prescribe two values $\boldsymbol{F}_{\text{low}}$ and $\boldsymbol{F}_{\text{up}}$ to define the range of band before the front.

$$0<\boldsymbol{F}_{\text{low}}<\boldsymbol{F}_{\text{Frt}}<\boldsymbol{F}_{\text{up}}<1 \tag{2-51}$$

By example, for the 2D triangle elements with 3 nodes, an element can be regarded in the band if there exists at least one node for its $\boldsymbol{F}$ value to locate between $\boldsymbol{F}_{\text{low}}$ and $\boldsymbol{F}_{\text{up}}$. Let Ω_{Frt} represent the band region (neighbor to the filling front). Assumed element e being anyone in the model, i is the node number belong to this element:

$$\forall \text{e}, \forall \text{i}\in \text{element e} \qquad \boldsymbol{F}_{\text{low}}<\boldsymbol{F}_{\text{i}}<\boldsymbol{F}_{\text{up}} \;\Rightarrow\; e\in\Omega_{\text{Frt}}(t) \tag{2-52}$$

as shown by the gray area in Fig. 2-6.

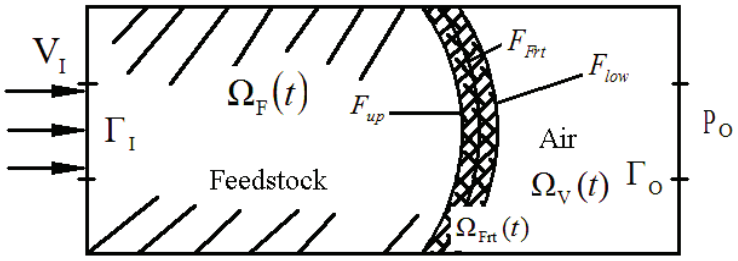

Fig. 2-6 Schematic of the band near filling front

Question two: how to modify the velocity field for computation of the filling state?

It is evident that the modified velocity fields are used only for solution of the filling states. The modified velocity fields should be smoothed and continuous ones. Otherwise solution of the advection equation will become the instable one to produce the spurious results.

A general smoothed procedure is proposed as followings

$$\{\boldsymbol{V}\}_{\boldsymbol{F}} = \bigcup_{\Omega^e}\int[\widetilde{\boldsymbol{N}}]^T[\widetilde{\boldsymbol{N}}]\boldsymbol{d}\Omega\{\boldsymbol{V}^e\}_{\boldsymbol{F}} \tag{2-53}$$

where $\{\boldsymbol{V}\}_{\boldsymbol{F}}$ is the velocity field, expressed in a discretized way at each node, for the solution of filling state. Pay attention that it is a modified and smoothed one to make

simulation of the front progress more realistic.

$\{\boldsymbol{V}^e\}_F$ represents the column of velocity values at all nodes of an elements. It takes initially the velocity values obtained by solution of the Stokes equations, but these values are modified when the elements locate in the band ahead of the filling front. First, one node with maximal $\boldsymbol{F}$ value will be determined as the upwind node, then the velocity value of the rest nodes in the same element will be replace by the velocity value of the upwind node.

For an element in the band, element number e and the node number i:

$$\begin{aligned} &\forall e \in \Omega_{\mathrm{Frt}}(t), \quad \forall i \in \text{ element } e \\ &\exists k \in \text{element } e, \quad \text{for} \quad \boldsymbol{F}_k = (\boldsymbol{F}_i)_{max} \end{aligned} \tag{2-54}$$

where k is the upwind-stream node number, it indicates the node of maximum $\boldsymbol{F}$ value $(\boldsymbol{F}_i)_{max}$ in the element.

$$\forall i \in \text{ element } e, \quad \text{let} \quad v_i = v_k \tag{2-55}$$

By this treatment to the velocity values of the elements located in the band, the velocity in thin layer elements ahead of the filling front is modified to be the values of the elements behind. This operation reinforces the effect of polymer behind the flow front, while reduces the unrealistic guidance of air flow ahead of the filling front. It represents more the real physical phenomenon. And it is more consistent with the true flow process.

For the details of different operators, let's take the triangle element of 3 nodes as a simpler example. This type of the elements includes 3 linear interpolation functions $\boldsymbol{N}_1$, $\boldsymbol{N}_2$, $\boldsymbol{N}_3$.

The values of $\boldsymbol{V}$ at element level $\{\boldsymbol{V}^e\}$ take the following form

$$\{\boldsymbol{V}^e\}^T = \{\boldsymbol{V}_{11} \quad \boldsymbol{V}_{12} \quad \boldsymbol{V}_{21} \quad \boldsymbol{V}_{22} \quad \boldsymbol{V}_{31} \quad \boldsymbol{V}_{32}\} \tag{2-56}$$

The matrix of interpolation function $[\widetilde{\boldsymbol{N}}]$ for velocity should be arrange in the corresponded form as

$$[\widetilde{\boldsymbol{N}}] = \begin{Bmatrix} \boldsymbol{N}_1 & 0 & \boldsymbol{N}_2 & 0 & \boldsymbol{N}_3 & 0 \\ 0 & \boldsymbol{N}_1 & 0 & \boldsymbol{N}_2 & 0 & \boldsymbol{N}_3 \end{Bmatrix} \tag{2-57}$$

2.2.3 Validation of the modification scheme

2.2.3.1 Simulation result of the proposed modification

This corrective strategy is also carried out based on the explicit algorithm with fully vectorial operations, which was previously developed in the research team with Taylor-Galerkin algorithm to solve the transport equation. For comparison, it also uses the same material (PP) and boundary conditions as the examples in Fig. 2-3 and Fig. 2-4. The related material properties can be referred to table 2-1.

By the proposed modification on solution algorithm, the injection filling processes in runners of shapes ⊥ and L are represented in Fig. 2-7 and Fig. 2-8. The filling duration for ⊥ shape and L shape cavity is 0.7s and 0.8s respectively. A constant speed is imposed on the inlet. For the injection by incompressible flow, the filling volume should be proportional to the injection time until totally filled.

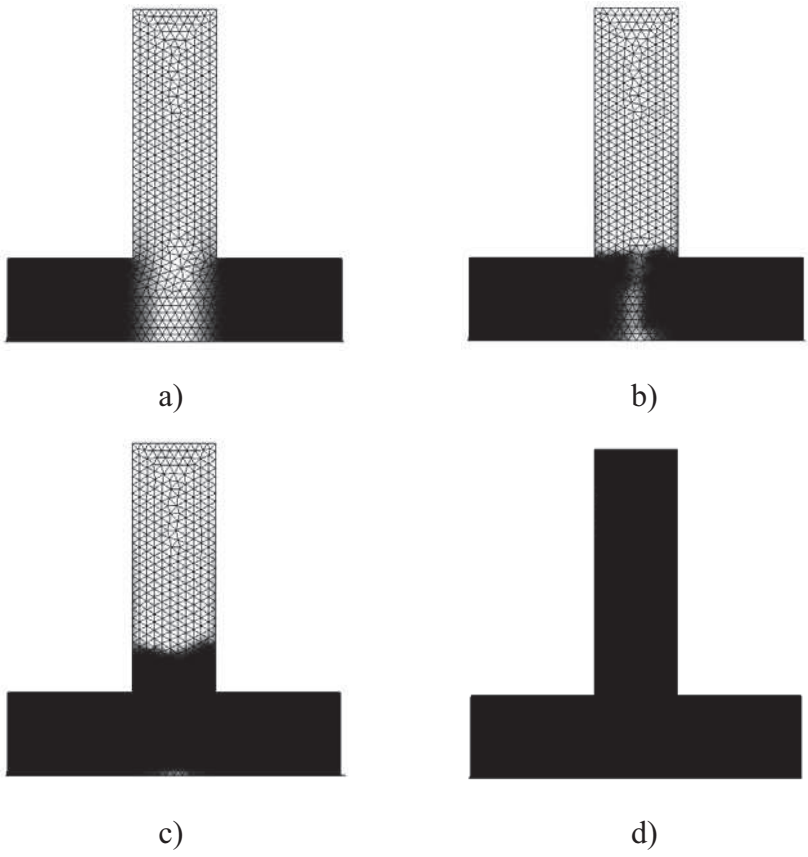

Fig. 2-7 Filling by two opposite inlets in cavity of shape ⊥ for different filling time: a) 0.32s, b) 0.38s, c) 0.45s, d) 0.7s.

Fig. 2-7 shows the injection process in runner of shape ⊥. The polymer is injected by two opposite inlets with the same speed. The filling fronts get advanced oppositely, join at middle of the cavity first and then go to the bi-pass together.

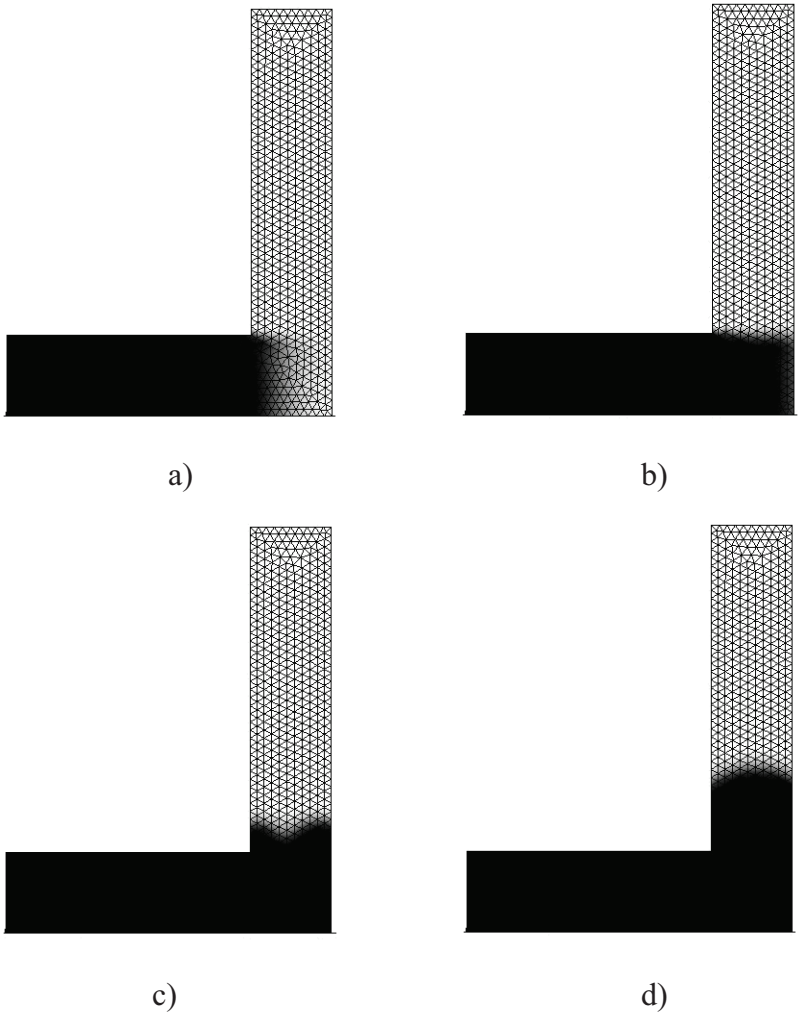

Fig. 2-8 filling process in mold cavity of shape L obtained in different filling time: a) 0.32s; b) 0.4s; c) 0.45s; d) 0.5s.

Fig. 2-8 shows the result of runner in shape of L by modified method. The polymer is horizontally injected into the mold cavity. It touches the wall at right end first, and then be extruded into the vertical runner.

By comparison of the simulation results in Fig. 2-3, Fig. 2-7 and Fig. 2-8, it is observed that the filling flows of polymer are more reasonable. They get advanced to join together, or touch the wall in front before moving into the by-pass. The wrong guide of air flow to make the opposite polymer flows going to bi-pass separately is largely reduced.

2.2.3.2 Comparison with experiments

In order to show more about the validity of the above proposed method, experiment results from G. Larsen [66] is introduced to make a comparative analysis. The specific micro-injection molding equipment Battenfeld Microsystem 50 has been used in G. Larsen's work to perform the molding process. A two-plate mold has been designed and manufactured in FEMTO-ST institute. It has the dimensions indicated Fig. 2-9(a). It is composed of three primary entities: mold die cavity (Fig. 2-9(b)) and ejector (Fig. 2-9(c)) for mechanical ejection of small components.

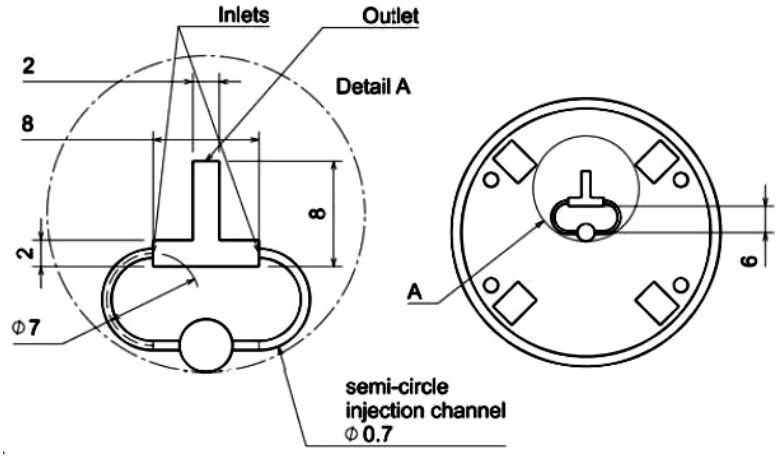

(a)

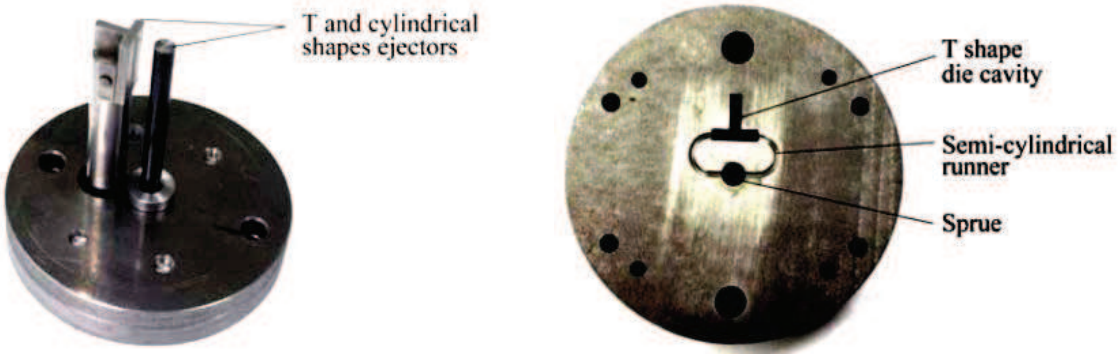

（b） (c)

Fig. 2-9 Detail of runners and micro-component: (a) floating die cavity insert for micro-injection designed for Battenfeld injection equipment, (b) geometry of the ejector, (c) injection runners and moving die mold cavity.

Short-shots have been achieved for the injection filling process. The Polymer (PP) is injected from the both inlets. The injection temperature is 210 °C, the injection velocity is 10 $m \cdot min^{-1}$ and the injection pressure is 35 bars. The Comparison between results from experiment and the improved simulation are shown in table 3-1.

Table 3-1 Comparison between results from experiment and the improved simulation

Short-shot from 58 ~ 65 mm^3	**Simulation result**
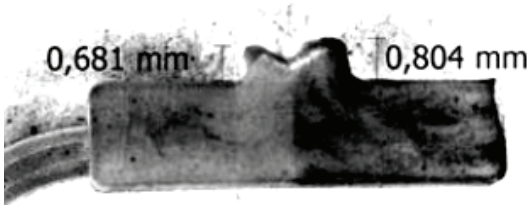	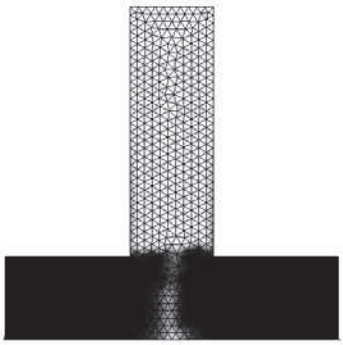
a) 58 mm^3, filling state: 69%	A) 0.38s, filling state: 54.3%
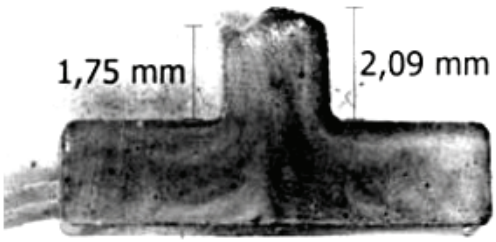	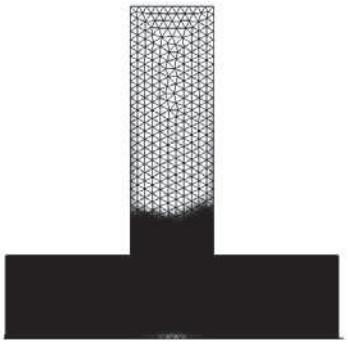
b) 60 mm^3, filling state: 71.4%	B) 0.45s, filling state: 64.3%
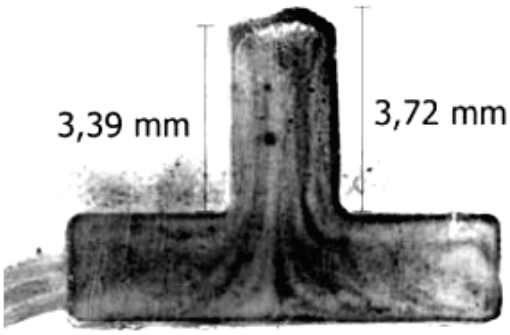	
c) 65 mm^3, filling state: 77.4%	C) 0.7s, filling state: 100%

From table 3-1, it can be seen that the track of filling flow is nearly the same as the experiment results. No clear differences appear in the whole filling process, including the instant when the two opposite flow merging together at the middle of bottom in ⊥ cavity. And it can be completely filled at the end of simulation without any air gap between the two evolving flow. It can be regarded as an effective and true simulation result.

2.2.4 Conclusion

In order to improve accuracy of the numerical simulation for injection molding process, source of the inexact filling fronts was analyzed. As Eulerian description is generally used for filling flow problems, the governing equation of filling state takes the form of advection equation. The extreme difference in properties of polymer and air results in different effects for their flows on the advance of filling front. This difference cannot be taken into accord by the governing advection equation. The filling of polymer may be wrongly guided by the flow of air, for some specific cases with the sudden change in flow direction of the polymer. To settle the problem, a corrective method is proposed and implemented, by the notion similar to upwind method. Based on the efficient explicit algorithm for PIM simulation and the FE software developed by research team, a systematic operation is designed to modify the velocity field of air flow close to filling front for solution of the filling advection equation. The untrue impact of air flow, represented by the velocity field ahead of the filling fronts, is significantly reduced. Then the advance of filling front can be mainly affected by the polymer flow behind the filling front. The simulation results show that the corrective algorithm can effectively improve the distorted results. The simulation of filling processes in the complex cavities with runners in shapes ⊥ and L can be significantly improved.

2.3 The outlet condition in simulation of MIM injection to track the end of filling process

As a new manufacturing technology, numerical simulation plays an important role in the efficient applications of PIM technology. As described in Section 2.1, there is a long history in analyzing the flow behaviors of injection molding process. It existed in the early 1950s [49] , then the analysis went to one-dimensional rectangular flow in 1959 [50], and two-dimensional flow since the late 1970s [51-54], then large amounts of research works were done in detail on fountain flow [55, 56]. The implicit finite element method for simulation of the filling process was firstly tried in 1990s [57-59]. It was found that the computational time for implicit algorithm was too tremendous, then the explicit algorithms were studied and realized to improve the efficiency [60, 61]. For further reduction in computational cost, a new explicit algorithm with fully vectorial operations was proposed by Liu [63], then carried out by the research work of Cheng [64, 65]. The global solutions in the previous explicit algorithm were eliminated. The computational cost is reduced to be about linearly proportional to the degree of freedom number.

However, there remains a persistent trouble in simulation of the filling states at the end of injection molding. It happens in the simulations of filling process with imposed constant velocity on inlet. As the polymer is regarded as incompressible flow, the filling ratio should be a linear one with respect to time. But the linearity is not respected when the filling front approaches to the outlet boundary. The cause is indicated in the Ph.D. thesis of T. Barriere [70] in 2000, but none of the references is involved to its solution in the retrieving of available sources. In fact, there is a lack of the integration term on the outlet boundary. This integration is negligible when the filling front is far away from the outlet, but it becomes significant when the front of polymer approaches. To remedy this defect, the modeling is formulated again. An integration term on the outlet boundary is realized in solution of the advection equation for filling state. The problem in solution of the filling process at the ending stage is finally solved. The examples prove well validity of the proposed method. Stability of the in-house solvers for solution of the volume fractions is improved.

2.3.1 The inexact result at the end of filling process

Because of incompressibility of the injection flow, the filling ratio should behave linearly versus time when constant velocity is imposed on inlet. But it did not at the ending stage of filling process, when the modeling and simulation in laboratory is applied. There remains a persistent trouble for simulation of the final stage of injection process, when the filling front approaches to the outlet boundary, as shown in Fig. 2-10.

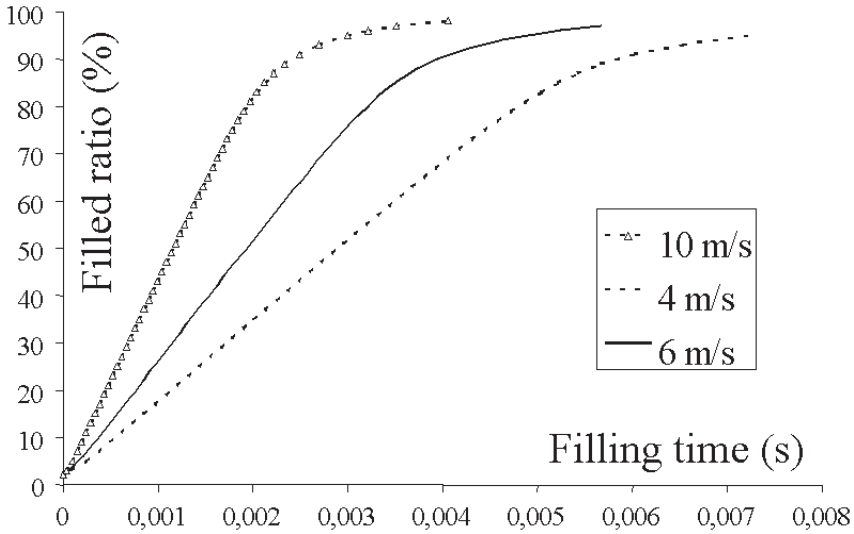

Fig. 2-10 Persistent troubles in simulation for the ending of filling process

The results reproduced accurately the real nature until the filling ratio reached to 90%, when the filling front gets near to the outlet boundary. Then the filling of remained void portion becomes slower than the true fact. The cause of such a trouble was indicated in the Ph.D. thesis of T. Barriere [70]. For Eq. 2-58, which is the weak form of the advection equation （Eq. 2-4）by a Taylor-Galerkin method, the integration was supposed to take value zero all around the boundary, while it is not true when the filling front approaches to the outlet boundary $\boldsymbol{X} \in \Gamma_O$.

$$\frac{\Delta t}{2}\int_{\Omega}\nabla\bullet[\,\boldsymbol{f}^{*}\boldsymbol{V}_n\cdot(\boldsymbol{V}_n\bullet\nabla\boldsymbol{F}_n)\,]\,\mathrm{d}\Omega=\frac{\Delta t}{2}\oint_{\Gamma}\boldsymbol{f}^{*}\boldsymbol{V}_n\cdot(\boldsymbol{V}_n\bullet\nabla\boldsymbol{F}_n)\bullet\vec{\boldsymbol{n}}\,\mathrm{dS} \tag{2-58}$$

where $\boldsymbol{F}_n$ and $\boldsymbol{V}_n$ represent the filling state and velocity variable at time step t_n, Δt stands for the time increment. $\boldsymbol{f}^{*}$ is a kinematically admissible field associated to variable $\boldsymbol{F}$. This equation takes indeed value zero when the filling front represents the distance to outlet boundary, when the filling ratio is smaller than 90%. But for the last duration in

injection course, this term must be taken into account to simulate correctly the filling pass through the outlet.

2.3.2 Modification of the outlet boundary condition

To remedy the problem mentioned above, an additional integration term should be taken into account on outlet boundary for the last stage in injection course. The following procedure is proposed to realize the adequate integration on outlet boundary.

The discretized form of advection equation（Eq. 2-4）by finite element method should be written as:

$$\mathbf{M}\,\frac{\boldsymbol{F}_{n+1}-\boldsymbol{F}_{n}}{\Delta t}=-\left[\mathbf{K}^{\mathbf{ad}}(\boldsymbol{V}_{n+1/2})+\mathbf{K}^{\mathbf{df}}(\boldsymbol{V}_{n})\right]\boldsymbol{F}_{n}+\mathbf{K}^{\mathbf{O}}(\boldsymbol{V}_{n})\,\boldsymbol{F}_{n} \tag{2-59}$$

where **M** is a lumped pseudo matrix constructed in a specific manner, $\mathbf{K}^{\mathbf{ad}}(\boldsymbol{V})$ is a stiffness matrix represents the advection effect while $\mathbf{K}^{\mathbf{df}}(\boldsymbol{V})$ is a stiffness matrix stands for diffusion effect. $\mathbf{K}^{\mathbf{O}}(\boldsymbol{V}_{n})$ is the operator for outlet surface integration term.

$$\mathbf{M}=\underset{\Omega}{A}\int_{\Omega^{e}}\boldsymbol{N}^{T}\,\boldsymbol{N}\,d\Omega \tag{2-60}$$

$$\mathbf{K}^{\mathbf{ad}}(\boldsymbol{V}_{n+1/2})=\underset{\Omega}{A}\int_{\Omega^{e}}\boldsymbol{N}^{T}\boldsymbol{V}_{n+1/2}^{T}\boldsymbol{G}\,d\Omega \tag{2-61}$$

$$\mathbf{K}^{\mathbf{df}}(\boldsymbol{V}_{n})=\frac{\Delta t}{2}\underset{\Omega}{A}\int_{\Omega^{e}}\boldsymbol{G}^{T}\boldsymbol{V}_{n}^{T}\boldsymbol{V}_{n}\boldsymbol{G}\,d\Omega \tag{2-62}$$

where A represents the assembling operation in finite element method. $\boldsymbol{N}$ is the matrix of interpolation functions in each element for filling state variables F, $\boldsymbol{G}$ is a gradient operator constructed by derivatives of these interpolation functions. $\boldsymbol{V}_{n+1/2}$ and $\boldsymbol{V}_{n}$ are the values obtained at each Gauss points.

Note $\boldsymbol{N}_{out}$ the nodes associated to outlet surface. Ω_{out}^{e} represents the elements associated to node $\boldsymbol{N}_{out}$, defined as:

$$\Omega_{out}^{e}=\left\{\,\Omega^{e}\;\middle|\;\boldsymbol{N}_{out}\subset\Omega^{e}\,\right\} \tag{2-63}$$

Let Γ_{out}^{e} represent the edge or side of element Ω_{out}^{e} on outlet boundary. A unit vector $\vec{\boldsymbol{n}}_{out}$ is defined for each element Ω_{out}^{e}. This vector is normal to its edge or side Γ_{out}^{e}.

The term $\mathbf{K}^{\mathrm{O}}(\boldsymbol{V}_n)$ in Eq. 2-59 takes the following forms:

$$\mathbf{K}^{\mathrm{O}}(\boldsymbol{V}_n)=\frac{\Delta t}{2}\underset{N_{out}}{\boldsymbol{A}}\int_{\Gamma_{out}^{e}}\boldsymbol{N}^{T}(\boldsymbol{V}_n^{e})^{T}\boldsymbol{V}_n^{e}\cdot\vec{\boldsymbol{n}}_{out}^{T}\boldsymbol{G}\,d\Omega \tag{2-64}$$

where $\boldsymbol{V}_n^{e}$ represents the velocity vector in the element associated to Γ_{out}^{e}.

By investigation of the flow pattern at outlet of the mold cavity, it is realized that the velocity vector $\boldsymbol{V}$ and outer normal $\vec{\boldsymbol{n}}$ take the same direction, whereas the gradient of variable $\boldsymbol{F}$ should exhibit the direction opposite to $\boldsymbol{V}$ and $\vec{\boldsymbol{n}}$. So on the integration of Eq. 2-58 can be simplified.

Taking into account the above mentioned features, the integration of Eq. 2-58 can be written as:

$$\frac{\Delta \mathrm{t}}{2}\oint_{\Gamma}\mathrm{f}^{*}\boldsymbol{V}_n\cdot(\boldsymbol{V}_n\bullet\nabla\boldsymbol{F}_n)\bullet\vec{\boldsymbol{n}}\,\mathrm{d}\boldsymbol{S}=\frac{\Delta \mathrm{t}}{2}\int_{\Gamma^{o}}\|\boldsymbol{V}_n\|\boldsymbol{V}_n\bullet\nabla\boldsymbol{F}\,\mathrm{d}\boldsymbol{S} \tag{2-65}$$

in which $\|\boldsymbol{V}_n\|$ is the norm of velocity vector, it represents the value $\|\boldsymbol{V}_n\|=\sqrt{\boldsymbol{V}_n\bullet\boldsymbol{V}_n}$.

Then the term $\mathbf{K}^{\mathrm{O}}(\boldsymbol{V}_n)$ in Eq. 2-59 takes the following forms:

$$\mathbf{K}^{\mathrm{O}}(\boldsymbol{V}_n)=\frac{\Delta \mathrm{t}}{2}\underset{N_{out}}{\boldsymbol{A}}\int_{\Gamma_{out}^{e}}\boldsymbol{N}^{T}\|\boldsymbol{V}_n^{e}\|\cdot(\boldsymbol{V}_n^{e})^{T}\boldsymbol{G}\,\mathrm{d}\Omega \tag{2-66}$$

where $\boldsymbol{V}_n^{e}$ represents the velocity vector in the element associated to Γ_{out}^{e}.

This solution scheme consists of only the local and explicit operations, so the prediction is very efficient.

A brief description on the modified algorithm relative to the outlet boundary condition is shown in Fig. 2-11.

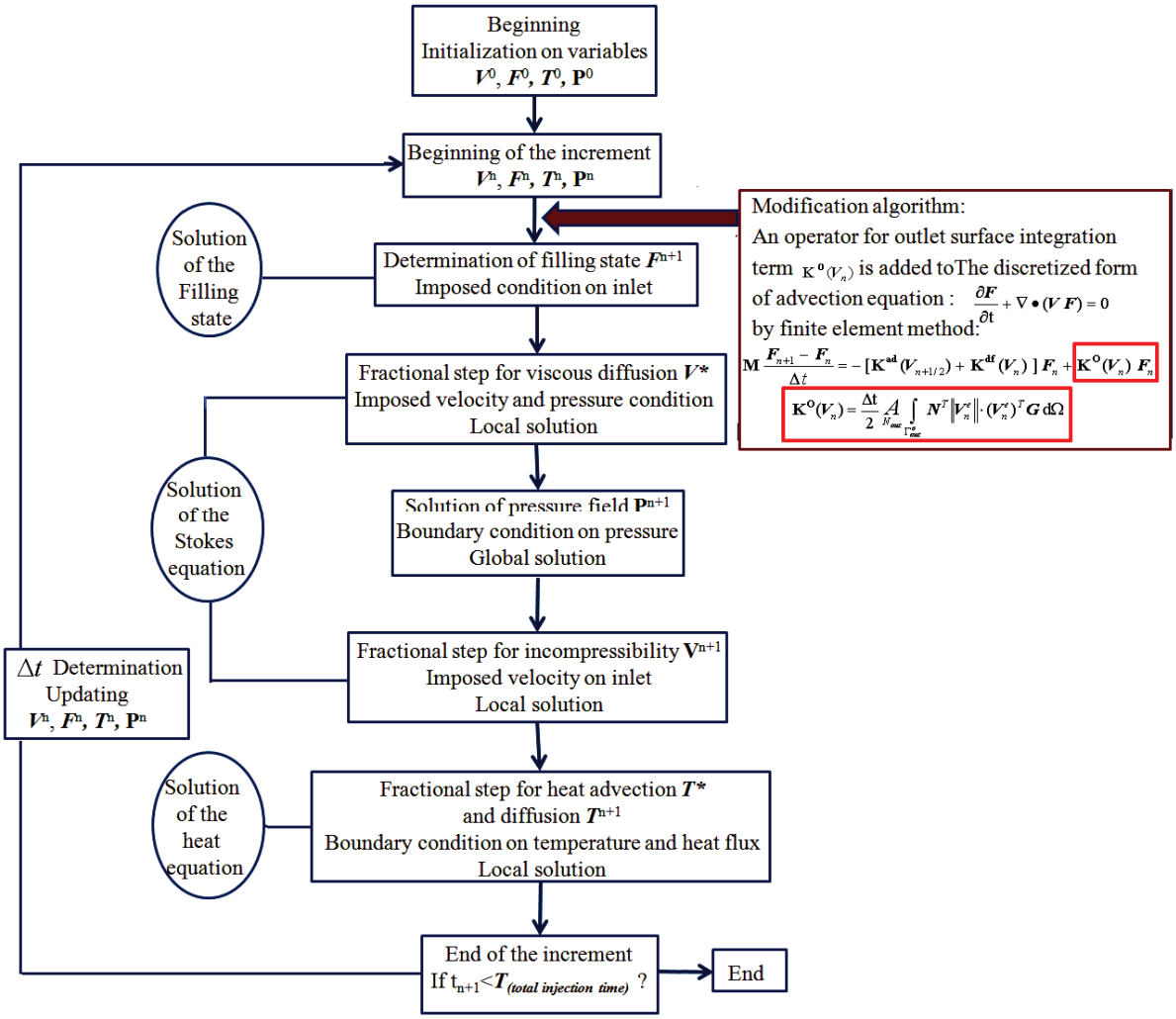

Fig. 2-11 The modified explicit algorithm relative to the outlet boundary condition for simulation of injection molding process. It is suggested to overcome the untrue delay of fully filling in the last filling stage.

2.3.3 Validation of the modified algorithm

The modified integration term on outlet boundary in section 4 was realized on Matlab (C) platform to focus the effort on its development and validation. As this work is based on the previous work on explicit algorithm in laboratory [67, 70], some technical issues were taken directly from the previous work. A simplest filling mold in shape of straight channel was chosen to do the simulation, which was often used as the evidence of validation for a newly developed algorithm. It was meshed with triangle elements as shown in Fig. 2-12. The related material properties are listed in table 2-2. These material properties and boundary

conditions are assigned just for the purpose of software validation. They do not mean the real values obtained from experiments.

Table 2-2 Material properties and parameters used in numerical simulations

Parameter	value
Feedstock:	Polymer (PP)
Density:	1 g/cm^3
Viscosity of the mixture:	100 Pa.s (constant viscosity)
Injection rate:	20 cm^3/s
Injected velocity:	4 m/s，6 m/s and 10 m/s respectively for the three examples (constant injected velocity)
Boundary condition:	sticky wall (no-slip on the wall)

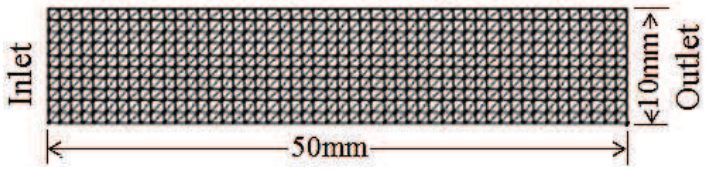

Fig. 2-12 Mesh of straight channel model

Comparison on evolution of the filling ratio versus time, obtained by previous and modified algorithm, is shown in Fig. 2-13. It shows that the results obtained by two methods are globally the same until the filling ratio reaches to 90%. Then the results issued of previous algorithm show the filling rates slower than the true ones. While the filling ratio of modified algorithm keeps nearly proportional all over the whole time, including the ending stage. Although it presents a little deviation to the real fact when it fills up to 98%, the fully filled pattern is soon achieved. For the approach and simulation by computation, it represents no more a significant problem.

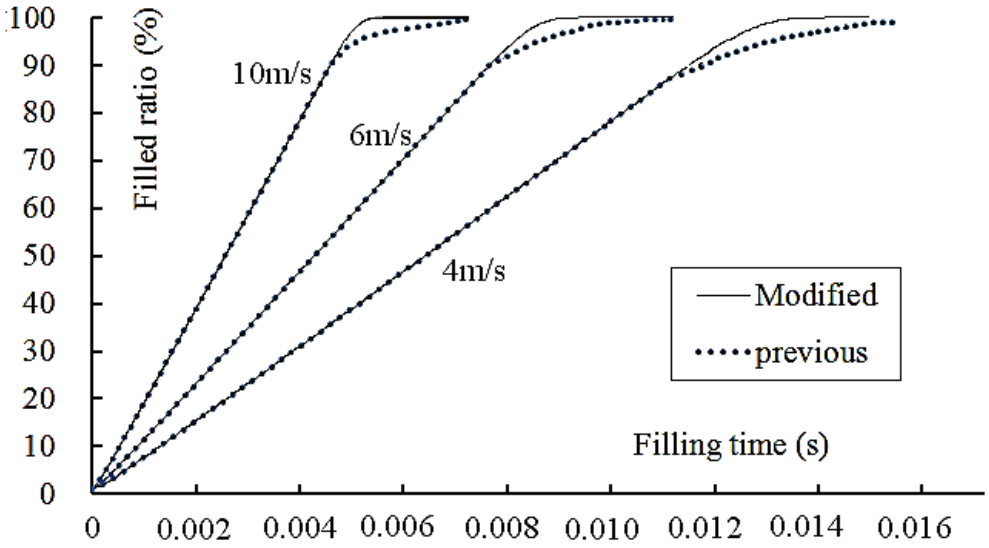

Fig. 2-13 Comparison on evolution of the filling ratio versus time

2.3.4 Conclusion

The modeling of injection molding is modified to simulate correctly the ending stage of filling process. The incorporated implementation is realized in the developed solver. The examples with constant injection velocity on inlet are provided to validate the proposed method. Based on the validations, one can conclude that:

(1) The modified boundary condition represents a true effect that should be taken into account. Incompressibility of the filling flow can hence be well respected at the last stage of filling process.

(2) The filing problems in simulation happened in the work of Dutilly [44] and Barriere [70] can be solved by modification of the boundary condition on outlet. The opinion of Barriere [70] was correct. Lack of the integration term on outlet boundary was the true cause for such a problem.

(3) The persistent problem is solved successfully. The simulation of filling process is made more reliable. Furthermore, the stability for solution of the volume fractions was improved. The in-house solver for simulation of the injection molding was optimized.

Chapter 3 Numerical method and analysis for surface tension effects in micro-injection process

Micro-injection molding is one of the effective manufacturing methods in the field of MEMS (Micro-Electro-Mechanical Systems). It is suited for the high-volume production of very small components [79]. As the injection molding in ordinary sizes, these components may be geometrically complex and have thin walls and structures.

Due to micro-scale factors, filling flow in micro die cavity shows the rheological phenomena different from the conventional ones [80]. The factors such as surface tension, wall slip, viscous dissipation and convective heat transfer, which can be not taken into account in simulation of macro-injection molding process, will play an important role when solving the problems in micro-scaled sizes. This chapter focuses on the proposition, implementation and validation of a method for surface tension force in FEM simulation, and the evaluation of surface tension effects in micro-injection filling process.

Surface tension is a contractive tendency of the liquid surface [81]. It is revealed, for example, in the floating of some objects on the surface of water, even though they are denser than water, and in the ability of some insects (e.g. water striders) to run on the water surface. This property is caused by cohesion of similar molecules, and is responsible for many of the liquid behaviors. Various inter molecular forces, such as Van der Waals forces, draw the liquid particles together. These cohesive forces between molecules in liquid are shared with all neighboring atoms. In the bulk of the liquid, each molecule is pulled equally in every direction by neighboring liquid molecules, resulting in a net force of zero. The molecules at the surface do not have the liquid molecules in outer side, and therefore exhibit stronger attractive forces on their nearest neighbors on the surface. This enhancement of the intermolecular attractive forces at the surface is called surface tension. Along the surface, the particles are pulled inwards the liquid.

In the process of micro-injection molding, the feedstock is injected into the mold cavity then air inside is squeezed out. In such a process, there exists a moving interface between the feedstock and the air. Because of different properties of the feedstock and air, the molecules

on interface are significantly more attracted by the molecules of feedstock than that of the air. Then the molecules on interface subject to the resultant force directed inward of the feedstock, as shown in Fig. 3-1.

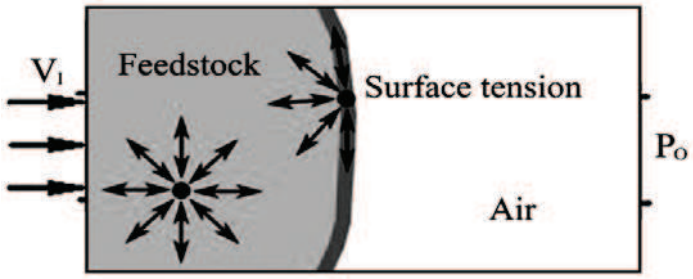

Fig. 3-1 Illustration of surface tension force in the interface of feedstock and air

The feasibility for simulation of micro-injection molding is dependent on accuracy and stability of the surface tension evaluation, when it is in sufficiently micro-scale [82]. Front capturing is prerequisite for its implementation. A number of numerical methods have been developed over the past few decades for front capturing. The well knows methods are volume-of-fluid [83], level-set [84], phase field [85], and Smooth Volume of Fluid [86] methods. Among them, two Eulerian-based methods, the volume-of-fluid (VOF) and level set (LS) methods have been extensively employed.

The VOF method was proposed by Hirt and Nichols [87] in 1981, which is the simplest treatment for controlling the numerical diffusion during advection of the VOF function. It was later proved to be robust and relatively easy to code. It satisfies well mass conservation while still maintaining a sharp representation of the interfaces [88]. But the overall accuracy of this method relies heavily on the performance of its interface reconstruction scheme. Because the VOF function is a step function and not continuous across the interface, it is difficult to obtain the accurate calculations of normal and curvature of the interface, then leads easily to unphysical flows around the interface. Several methods have been proposed later to reduce these spurious currents by coupling the VOF function with smoothing kernels [89], height-function (HF) [90], and parabolic fitting (PROST) [91]. The level-set (LS) method, first introduced by Osher and Sethian [92], was known as a very efficient interface-capturing method. The advantages of LS method are the fact that the curvature can be computed accurately and the smoothness of discontinuous physical quantities near interfaces is very

good. It suits for flows with large flow distortions and geometrical changes. However, because the LS function is a smooth function, it produces more numerical error than VOF method, especially when the interfaces experience severe stretching or tearing. It has been shown in [93] that this method is subjected to significant mass loss under complicated situations since the scheme does not explicitly impose mass conservation.

Based on the above analysis to VOF and LS methods respectively, it can be found that they have the complementary advantages and disadvantages. So it is an inevitable trend to develop a method combining the VOF and LS methods. That is the coupled method (CLSVOF method), which was introduced by Bourlioux [94], and then put forward by Sussman and Puckett [88], Son and Hur [95] and Menard et al. [96]. In the CLSVOF method, the interface is reconstructed via a PLIC (Piecewise Linear Interface Construction) scheme from the VOF function and the interface normal vector is computed from the LS function $\vec{n} = \nabla\varphi / |\nabla\varphi|$ (where φ is an approximation of the signed distance function to the interface). The principle of this coupling is to use VOF function for mass conservation, while the interface and curvature is captured smoothly by the LS function. Curvature of the interface is evaluated by:

$$\kappa = \nabla \cdot \vec{n} = \nabla \cdot \left(\frac{\nabla\varphi}{|\nabla\varphi|} \right) \tag{3-1}$$

where $\vec{n}$ is the interface normal vector, φ is an approximation of the signed distance function to the interface.

To solve the differential Eq. 3-1 for curvature, the approaches such as the Finite Volume Method (FVM), Finite Difference Method (FDM) and Finite Element Method (FEM) are widely used. It is discretized by the finite volume method on the non-staggered meshes in [97]. Sun and Tao [98] proposed an iterative geometric operation to calculate the level set function near interfaces, which can be applied to compute the accurate curvature and smooth the discontinuous physical quantities near interfaces. Based on FVM, it uses the high order ENO upwind difference [99] for the convection term and the central difference for the viscous and curvature terms. In [100], the advection equation of level set function is solved by a second-order finite volume method. The advection of volume fraction is performed by a

scheme based on bounded compressive normalized variable diagram (NVD). The interface is reconstructed by both the level set and the volume fraction information. In [88], the CLSVOF method is used but it does not smooth the curvature at all. The curvature is obtained via finite differences of the level set function, which is derived at the previous time step by both the level set function and volume-of-fluid function.

Compared to finite difference method, finite element method is easy to be used with a great variety of the element types, and is thus capable of handling complex geometries and boundary conditions. Moreover, it is very convenient to improve the finite element codes for the solution of fluid structure interaction problems with free surface. Hysing [101] introduced a new level set methodology for simulation of immiscible fluid flows, which essentially combines a non-conforming finite element flow solver with a conforming level set interface tracking method. It used a more accurate approach to reconstruct the curvature via L2-projection and patch recovery operations. In [102], surfaces are implicitly represented by the level set method. It studies the possibility to use the shape functions of higher order approximation with X-FEM, when geometries include curved discontinuities. The finite element approximation is enriched by additional functions with the notion of partition of unity to track material interfaces. Yang et al. [103] presents an adaptive CLSVOF method for interfacial flow simulations on unstructured triangular grids. At each time step, it evolves both the level set function and the volume fraction. Evolution of the level set function is governed by advection equation. A discontinuous Galerkin finite element method is used for its solution. The advection of volume fraction is performed by a Lagrangian–Eulerian method.

However, when dealing with the determination of front curvature according to Eq. 3-1, it contains second derivative of the function, in the form of a Laplacian operator. As the filling function is a scalar one while the velocity function is a vector one, the integration of filling function in second derivative is not suitable be transformed into the boundary integration and the integration of function in lower order derivative. It is difficult to use ordinary integral transform to reduce the derivative order of integrated function. Some methods were previously proposed to settle this problem. In traditional level set methods [104], curvature is computed from the spatial derivatives of a scalar function at any instant in time,

as $\kappa = \nabla \cdot \left(\frac{\nabla \varphi}{|\nabla \varphi|} \right) = \frac{\varphi_{xx}\varphi_y^2 - 2\varphi_x\varphi_y\varphi_{xy} + \varphi_{yy}\varphi_x^2}{\left(\varphi_x^2 + \varphi_y^2\right)^{3/2}}$ (where φ is a function of the signed distance to interface). On a Cartesian grid, this divergence is generally calculated at node points by using a 9-point stencil with centered differences for all the partial derivatives. Ramšak and Škerget [105] presented an efficient 3D multi-domain boundary element method (BEM) for solving problems governed by the Laplace equation, where the domain problem is transformed into a boundary problem. It used a multi-domain approach, also known as the subdomain technology, very similar to FEM. Trontin et al. [106] uses markers with the LSET-PART method to redefine the curvature. The cubic spline interpolation gives for each marker an estimation of the local curvature of the interface. It can be evaluated exactly on the interface without any interpolation from the Eulerian grid. Rangogni [107] dealt with the generalized Laplace equation by coupling the boundary element method with the perturbation method. The method requires an internal network but the unknowns are only on the boundary. Based on the VOF method, Meier et al. [108] devised a new method, which used empirical formulas obtained from databases that had been generated and stored in a data bank to determine the interface curvatures. Raessi et al. [109] presents a new method for calculating interface normal vectors and curvatures, where the interface unit normal is advected along with whatever function represents the interface, and curvatures are calculated directly from these advected normals.

Due to the lack of appropriated FEM method for curvature calculation, the present investigation proposed a simpler and easier way for implementation of the surface tension effect in finite element method. The work provided an effective method for the analysis of capillarity-dominant free surface flows in micro-injection molding, which involves the computation of Laplacian operation for evaluation of the curvature of filling front. It can be used in the problems that require the integration of a scalar function (filling function) in second derivative, but the effect is associated with the vector functions. It affords the practical way for evaluation of the surface tension effects in viscous filling flow. The incorporation of surface tension effect is realized under the frame of Taylor-Galerkin method, which is used for solution of the advection equation to track the filling front. The notion of

CLSVOF method is used. The force of surface tension is incorporated into the Navier–Stokes equation via an individual source term. At each time step, both the level set function and the volume fraction are evolved to update the filling front. The level set function in advection equation is evolved by the Taylor-Galerkin method of second-order characteristics. The interface is reconstructed based on the information of level set and volume fraction. It provides the necessary accuracy for evaluation of the surface curvature and the surface normal on the filling front. The present work takes the mathematic model of surface tension force as explained by Tong and Wang [75], but the implementation is realized in an explicit finite element solver [64] with the easy method proposed by author. The work of Tong and Wang [75] is based on the finite difference method with the easy way to evaluate the second derivative of level set function. The FEM explicit solver employs the simple elements of low order interpolation functions, so no second derivative of the function can be obtained by a direct way. The numerical implementation is clearly distinguished. The explicit finite element solver, developed by the research team, appears to be an efficient tool for simulation of the viscous filling flow [64]. However, the elements of low order interpolation functions do not provide the direct way to evaluate the second derivative of represented function. To avoid the complication in evaluation of the Laplacian operation on filling function, a specific method is proposed to evaluate curvature of the filling front by the simple and systematical procedures. Then the force of surface tension can be introduced directly in solution of the Navier-Stokes equation. By comparison between the magnitudes of surface tension force with the viscous force for a filling example in micro channels, the effects of surface tension in micro injection molding were studied. It shows the importance of surface tension in micro injection molding of sub-millimeter sizes, though this effect does not represent the significance in ordinary injection molding process. These numerical results are in close agreement with the data reported in the literature [110].

3.1 Mechanical modeling

The general definition of filling process variables, boundary conditions of the injection molding, the governing equations including advection equation, Navier-Stokes equation,

incompressibility condition, energy conservation, and the explicit FEM algorithm for simulation have been introduced in chapter 2, section 2.1.

In the present thesis, surface tension effect is introduced. The implementation is based on a coupled volume-of-fluid (VOF) and level set (LS) method (CLSVOF) to track the filling front. Based on VOF definition, the field variable $\boldsymbol{F}(x,t)$ is also defined to represent filling state in the mold at different instants. It is used for visualization of the filling patterns during the injection course, and the assignment of different material properties at each time step for filled and void portion in mold cavity. This variable is governed by the advection equation (Eq. 2-4), which is shown again by Eq. 3-2. The mechanical model of injection flow with surface tension effect is shown in Fig. 3-2. According to the continuum surface force (CSF) model, the surface tension force $\mathbf{F}_{st}$ is handled to be a body force $\mathbf{F}_b$ in a thin layer of the front. The details will be discussed later in the chapter.

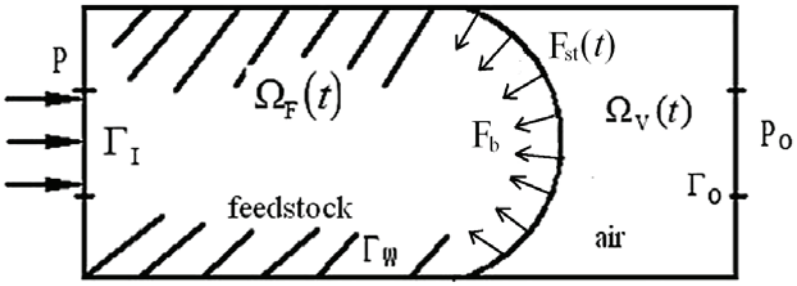

Fig. 3-2 Mechanical model of injection flow with surface tension effect

$$\frac{\partial \boldsymbol{F}}{\partial t} + \nabla \bullet (\boldsymbol{V}\,\boldsymbol{F}) = 0 \tag{3-2}$$

For the convenience in numerical methods, the solution of above advection equation is based on the continuous functions, and discretized at each time step. The continued function is in fact the LS function, named φ by other authors [92]. It is called the filling function *F*, for clearness and integrity of the presentation. It changes continuously across the filling front, with a prescribed value to distinguish the position of filling front. The value of filling function in mold cavity varies according to the distance from filling front. It distributes from higher value in filled portion to lower value in void portion. The governing equation for evolution of the filling function is expressed in the same way as shown in Eq. 3-2. The

solution of advection equation is to determine a function $F(x,t)$ continuous in space. Then the filling front locates at the position X_F where the filling function takes a prescribed value between the larger value in filled portion and smaller value in void portion.

$$X_F = x\Big|^{F=F_P} \tag{3-3}$$

where F_p is a prescribed value to identify the position of filling front according to the distribution of filling function F. This value can be adjusted for the purpose of mass conservation in filling process.

The continuum surface force (CSF) model [111] has been widely used to introduce the surface tension. In the CSF model, surface tension effect is treated as a body force $\mathbf{F}_b$ in a thin layer of the elements that locate on the filling front. It can be added directly into the Navier-Stokes equation (Eq. 2-5 & Eq. 2-6) as a source term. Considering surface tension force, the equations of momentum conservation for two different portions can be expressed as:

$$\forall x \in \Omega_{\mathrm{F}},\ \ \rho_p(\frac{\partial \mathbf{V}}{\partial t} + \mathbf{V} \bullet \nabla \mathbf{V}) = -\nabla P + \nabla \bullet \boldsymbol{\sigma}'_p + \rho_p \mathbf{g} + \mathbf{F}_b \tag{3-4}$$

$$\forall x \in \Omega_{\mathrm{V}},\ \ \rho_a(\frac{\partial \mathbf{V}}{\partial t} + \mathbf{V} \bullet \nabla \mathbf{V}) = -\nabla P + \nabla \bullet \boldsymbol{\sigma}'_a + \rho_a \mathbf{g} \tag{3-5}$$

where ρ_p is the density of feedstock in the filled mold cavity, ρ_a is the air density in the unfilled mold cavity. P represents the hydraulic pressure field, $\boldsymbol{\sigma}'_p$ and $\boldsymbol{\sigma}'_a$ are the deviatoric Cauchy stress tensors in filled and void portion, that is, in the feedstock and air inside the mold cavity. $\mathbf{g}$ is the gravity vector. $\mathbf{F}_b$ represents the surface tension force in the filling front. In the modeling, the surface tension is supposed to be acted on in a thin layer of the feedstock that locates on filling front. It should be mentioned that the material properties for air portion are chosen different from their true values, for the purpose to keep numerical stability. In order to keep consistency of the solution scheme for the whole model, the same operations are carried out for both the portion filed by feedstock and the portion that contains still the air. It may result in the instability in numerical solution if the mass and

viscosity in void portion are too much different from the ones in filled portion. However, the exact flow in void portion is not our interest. The result of such a numerical treatment is acceptable, as our main objective is the flow of injected feedstock.

3.2 Surface tension force

With the CSF model, surface tension effect is treated as a body force $\mathbf{F}_b$ and added into the Navier-Stokes equation as an external force. It is distributed within a transition region of finite thickness at the interface, given by:

$$\mathbf{F}_b = \sigma\kappa\vec{n}\delta(x) \tag{3-6}$$

where σ is the coefficient of surface tension, κ is the curvature of filling front surface, $\vec{n}$ is normal vector of the surface, indicated inward the injected material. $\delta(x)$ is a delta function concentrated at the interface. From the definition of filling function $\boldsymbol{F}(x,t)$, the gradient of filling function $\nabla\boldsymbol{F}(x,t)$ represents a vector in inner normal direction of the filling front. Its value in tangential direction of the interface is zero. So the following expression can be used:

$$\forall x \in x_p \ , \ \vec{n} = \nabla\boldsymbol{F}(x,\ t) \ / \ | \ \nabla\boldsymbol{F}(x,\ t) \ | \tag{3-7}$$

The above expression serves to determine unit normal of the filling front surface, no matter how much is the value of filling function and the magnitude of its gradient.

The body force in Eq. 3-6 can also be expressed into:

$$\mathbf{F}_b = \sigma\kappa\nabla\boldsymbol{F}\left(x,t\right)\Big/\left|\nabla\boldsymbol{F}\left(x,t\right)\right| \tag{3-8}$$

This body force will be included into the momentum equation as a source term, as $\mathbf{F}_b$ in Eq. 3-4. This continuous treatment of the discontinuous change at the interface makes easier the implementation of surface tension effect. In problems with complex topological changes, the CSF model is superior to the conventional method in robustness and versatility.

3.3 Implementation of Surface tension in FEM

From Eq. 3-8, it is evident that accuracy of the curvature estimation is the key issue in

implementation of the surface tension.

3.3.1 Surface curvature computation

As in Eq. 3-1, normal and curvature of the filling front can be calculated by the distance functions in LS method. In mathematics, it depends on the shape of filling front surface, no matter value of the LS function and the magnitude of its gradient. In the present study, the LS function is replaced by the filling function $\boldsymbol{F}(x, t)$. The expression in Eq. 3-1 then becomes:

$$\kappa=\nabla\cdot\vec{n}=\nabla\cdot\left(\frac{\nabla \boldsymbol{F}}{|\nabla \boldsymbol{F}|}\right) \tag{3-9}$$

The filling function $\boldsymbol{F}(x, t)$ is determined by simulation of the filling state, that is, the solution of advection equation (Eq. 3-2). Based on the filling function $\boldsymbol{F}$ at actual instant, curvature of the filling front $\kappa(x)$ can be determined by an explicit way, as shown in Eq. 3-9.

For implementation of the surface tension in finite element method, it is necessary to realize the second derivative of filling function, incorporating with the interpolation functions of finite elements. The research in laboratory resulted in the development of an explicit algorithm, in which the simple elements of low order interpolation functions are used [112]. The integration of filling function in second derivative is not suitable be transformed into the boundary integration and the integration of function in lower order derivative, because of the difference in dimension for filling function and velocity function. To evaluate conveniently the curvature of filling front, a simple and systematic scheme is suggested and implemented into the explicit FEM solver. This specific scheme includes only the vectorial operations in low cost, and is completely systematic without piecemeal operations. In solution of the Navier-Stokes equation, the source term including field $\kappa(x)$ is determined by the following procedure:

1) Firstly get the gradient field at the nodes

$$\{\nabla \boldsymbol{F}\} = \underset{\Omega}{\mathbf{A}} \int_{\Omega^e} [\boldsymbol{N}]^T [G] dV \{\boldsymbol{F}^e\} \tag{3-10}$$

where A represents the assembling operation of finite element methods, $[\boldsymbol{N}]$ is the matrix of interpolation functions for filling function. [$\boldsymbol{G}$] is a gradient operator consists of the derivatives of interpolation functions for filling function $\boldsymbol{F}$. $\{\nabla \boldsymbol{F}\}$ stands for the discretized field of $\nabla \boldsymbol{F}$, represented at the nodes. $\{\boldsymbol{F}^e\}$ includes the node values of $\boldsymbol{F}$ for a prescribed element.

2) In the second steps, the Laplace of $\boldsymbol{F}$ is determined by the following way

The values determined at Gauss point can be obtained by:

$$\kappa = \Delta \boldsymbol{F} = [\boldsymbol{D}]\{\nabla \boldsymbol{F}^e\} \tag{3-11}$$

If the discretized values at nodes $\{\Delta \boldsymbol{F}\}$ are required for next procedure of the solution, the discretized field of Laplace $\boldsymbol{F}$ is determined by

$$\{\kappa\} = \{\Delta \boldsymbol{F}\} = \underset{\Omega}{\mathbf{A}} \int_{\Omega^e} [\boldsymbol{N}]^T [\boldsymbol{D}] d\boldsymbol{V} \{\nabla \boldsymbol{F}^e\} \tag{3-12}$$

where $[\boldsymbol{D}]$ is a divergence operator, built based on the interpolation function for filling function.

According to the work of Cheng [67], the elements with equal order interpolation are adopted in the new explicit vectorial algorithm instead of the use of MINI element in mixed interpolations. A systematic smoothing scheme is chosen to avoid the mesh lock and numerical instability. For illustration, a simple example of triangle element with linear interpolation is used. This type of the elements includes 3 linear interpolation functions N_1, N_2, N_3 for filling function $\boldsymbol{F}$.

$$[\boldsymbol{N}] = \begin{Bmatrix} N_1 & 0 & N_2 & 0 & N_3 & 0 \\ 0 & N_1 & 0 & N_2 & 0 & N_3 \end{Bmatrix} \tag{3-13}$$

The nodal values of $\boldsymbol{F}$ for an element $\{\boldsymbol{F}^e\}$ take the following form:

$$\{\boldsymbol{F}^e\}^T = \begin{Bmatrix} \boldsymbol{F}_1^e & \boldsymbol{F}_2^e & \boldsymbol{F}_3^e \end{Bmatrix} \tag{3-14}$$

The discretized value of $\nabla \boldsymbol{F}$ at element level is assigned in the form:

$$\{\nabla \boldsymbol{F}^e\}^T = \left\{ \nabla \boldsymbol{F}_{1x}^e \quad \nabla \boldsymbol{F}_{1y}^e \quad \nabla \boldsymbol{F}_{2x}^e \quad \nabla \boldsymbol{F}_{2y}^e \quad \nabla \boldsymbol{F}_{3x}^e \quad \nabla \boldsymbol{F}_{3y}^e \right\} \tag{3-15}$$

The gradient operation should be determined in the following way:

$$[\boldsymbol{G}] = \begin{Bmatrix} \dfrac{\partial N_1}{\partial x} & \dfrac{\partial N_2}{\partial x} & \dfrac{\partial N_3}{\partial x} \\ \dfrac{\partial N_1}{\partial y} & \dfrac{\partial N_2}{\partial y} & \dfrac{\partial N_3}{\partial y} \end{Bmatrix} \tag{3-16}$$

The divergence operator is to be made in the way:

$$[\boldsymbol{D}] = \begin{Bmatrix} \dfrac{\partial N_1}{\partial x} & \dfrac{\partial N_1}{\partial y} & \dfrac{\partial N_2}{\partial x} & \dfrac{\partial N_2}{\partial y} & \dfrac{\partial N_3}{\partial x} & \dfrac{\partial N_3}{\partial y} \end{Bmatrix} \tag{3-17}$$

3.3.2 Surface tension force in computation

In finite element method, the surface tension is implemented in a layer of the elements, located at the positions of filling front surface. It is processed as body force acting in a thin layer at the front. Term $\mathbf{F}_b$ in Eq. 3-6 can be directly added into the Navier-Stokes equation, as shown in Eq. 3-4. Based on the explicit algorithms, the evolution of velocity field is effected by two fractional steps [64]. Effects of viscous diffusion, force loading and surface tension are considered in the first step. The incompressibility is kept in the second step, with the solution of pressure field. By Galerkin method [113], Navier-Stokes equation (Eq. 3-4), including the term of surface tension, can be discretized in the following form:

$$\forall x \in \Omega \qquad \mathbf{M} \frac{\mathbf{V}_{\mathrm{n}}^* - \mathbf{V}_n}{\Delta t} = \mathbf{F}_{\sigma} + \mathbf{F}_{\mathrm{ext}} + \mathbf{F}_{\mathrm{st}} \tag{3-18}$$

where $\boldsymbol{V}_{\mathrm{n}}^*$ is the velocity fields of temporary middle values, $\mathbf{M}$ is the mass matrix lumped into diagonal form, $\mathbf{F}_{\sigma}$ is the viscous diffusion term, $\mathbf{F}_{\mathrm{ext}}$ is the load vector with gravity contribution and boundary conditions. $\mathbf{F}_{\mathrm{st}}$ is the term of surface tension force.

$$\mathbf{F}_{\sigma} = \underset{\Omega}{A} \int_{\Omega^e} [\mathbf{B}]^T \boldsymbol{\sigma}' \, d\boldsymbol{\Omega}$$

$$\mathbf{F}_{\text{ext}} = \underset{\Omega_{\text{F}}}{A} \int_{\Omega^e} [\boldsymbol{N}]^T \rho_{\text{p}} \mathbf{g} d\boldsymbol{\Omega} + \mathbf{f}^{ext}$$

$$\mathbf{F}_{\text{st}} = \underset{\Omega}{A} \int_{\Omega^e} [\boldsymbol{N}]^T \mathbf{F}_b \, d\mathbf{V} = \underset{\Omega}{A} \sigma \int_{\Omega^e} [\boldsymbol{N}]^T \sigma \kappa \vec{n} \delta(x) \, d\mathbf{V}$$

$$= \underset{\Omega}{A} \sigma \int_{\Omega^e} [\boldsymbol{N}]^T \{\nabla \boldsymbol{F}(x,t) / |\nabla \boldsymbol{F}(x,t)|\}^e [\mathbf{D}] d\mathbf{V} \{\nabla \boldsymbol{F}^e\} \tag{3-19}$$

where A represents the assembling operator in finite element method, $\mathbf{B}$ is the matrix of derivatives of the interpolation functions $[\boldsymbol{N}]$ in an element, defined to calculate the symmetric part of velocity's gradient $\dot{\boldsymbol{\varepsilon}} = \mathbf{B}\mathbf{V}^e$, $\mathbf{V}^e$ represents the nodal values of velocity vectors in an element, $\boldsymbol{\sigma}'$ stands for the deviator of Cauchy stress tensor, $\mathbf{f}^{ext}$ stands for the surface loads converted to the nodes on boundary. In the void portion, $\boldsymbol{F}_{\text{ext}}$ is generally set to be 0, as the gravity effect of air can be ignore and pressure imposed on outlet is 0

The second fractional step is to satisfy incompressibility of the filling flow, with the solution of pressure field. The relevant literatures can be referred for its implementation [64].

A brief description on the explicit algorithm for simulation of micro-injection molding process, which is taking into account the surface tension effect, is shown in Fig. 3-3.

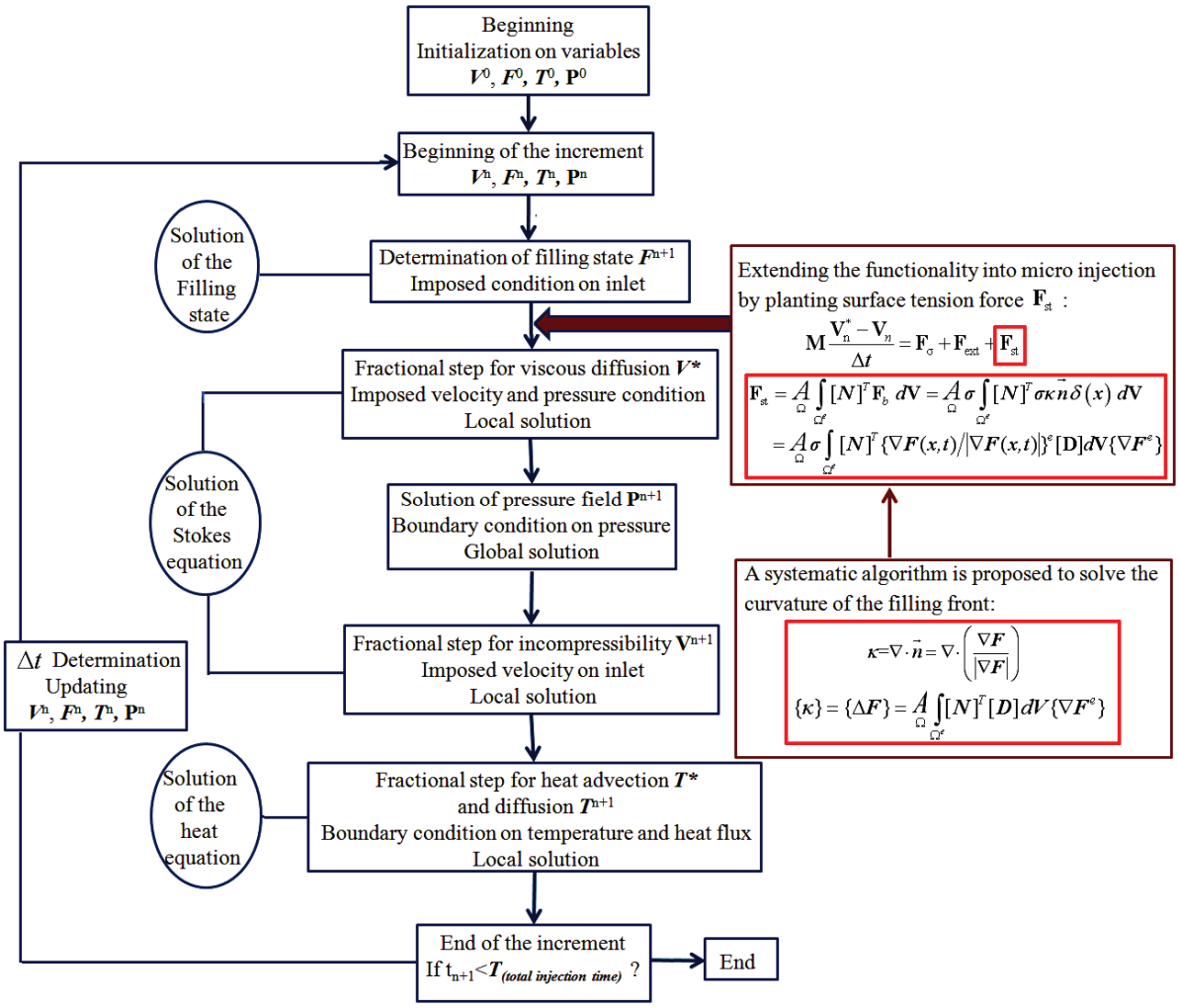

Fig. 3-3 The explicit algorithm for simulation of micro-injection molding process with taking into account the surface tension effect. A simple and systematic operation is proposed for filling front curvature calculation in FEM method.

3.4 Numerical investigation and discussion

In order to study the effect of surface tension in the process of micro-injection molding, the evaluation of surface tension force in filling viscous flow is realized by simulation. The development is made on the explicit algorithm with fully vectorial operations [64], previously developed in research team. Based on the finite element software developed on Matlab (C) platform, this section focuses on realization and validation of the new developed function for surface tension.

For simplification, the injection filling in a straight channel for 2D case is often chosen

as the first validation of new algorithm. The model meshed with triangular elements is shown in Fig. 3-4. The width of mold inlet W=10 mm, the mold length L =5×W =50 mm. The mesh includes totally 561 nodes, 1000 triangle elements. The related material properties are listed in table 3-1. These material properties and boundary conditions are assigned just for the purpose of software validation. They do not mean the real values obtained from experiments.

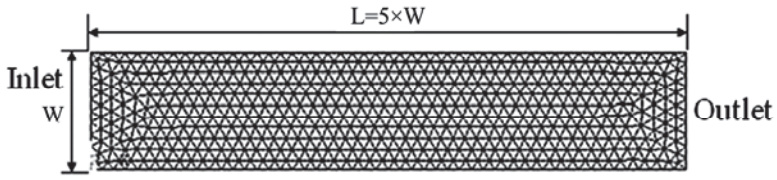

Fig. 3-4 Finite element mesh of straight channel for simulation of injection filling process in 2D case

Table 3-1 Material properties and parameters used in numerical simulations

Parameter	value
Feedstock:	Polymer (PP)
Density:	1 g/cm^3
Viscosity of the mixture:	100 Pa.s (constant viscosity)
Injection rate:	20 cm^3/s
Injected pressure:	p = 1 × 10^5 Pa (constant pressure along the axial direction)
Boundary condition:	sticky wall (no-slip on the wall)
Surface tension coefficient	$\sigma = 0.5$ (constant value)

Based on the explicit algorithm of research team [64], the present work focuses on investigation of the surface tension effects in filling processes of the viscous flow. The comparison of filling states with or without the effect of surface tension at the same instant is shown in Fig. 3-5. The component of surface tension force in horizontal direction x and in vertical direction y is shown in Fig. 3-6.

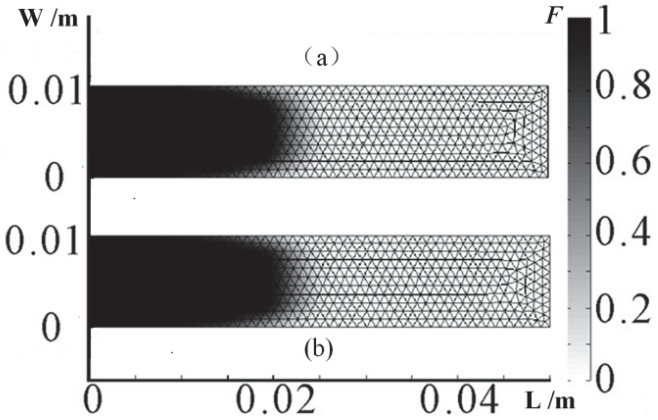

Fig. 3-5 Comparison of the filling states with or without the effect of surface tension at the same instant: (a) Without surface tension; (b) With surface tension effect.

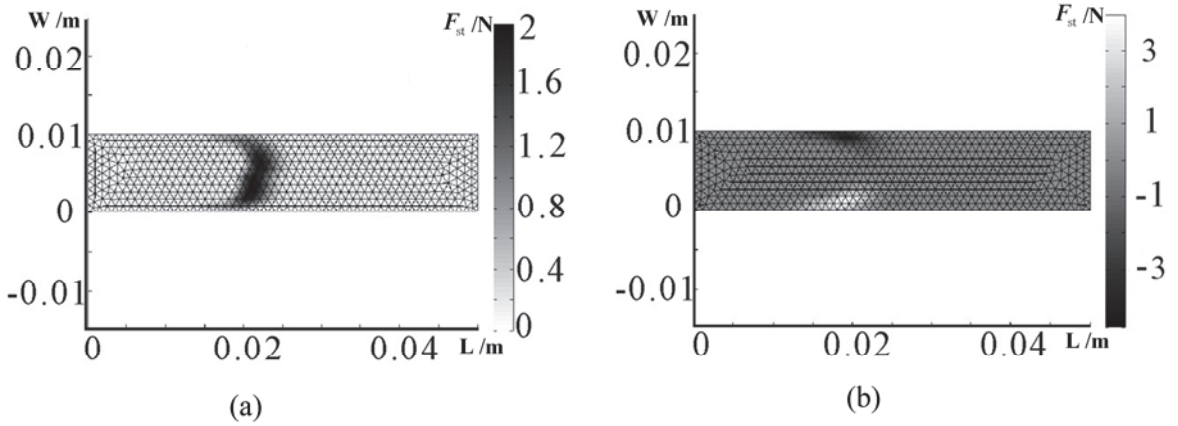

Fig. 3-6 Distribution of surface tension force: (a) Component in x direction; (b) Component in y direction

For analyzing the impacts of surface tension on molds filling of different scales, the examples of different sizes are realized in simulation. In order to understand the variation of surface tension effect when the geometrical scale of mold filling changes, the examples are made under the same conditions, except for their sizes. The meshes for different models of different sizes remain proportionally the same, except that the size of elements changes accordantly. Then the influence of element distribution can be removed for the examples of different sizes.

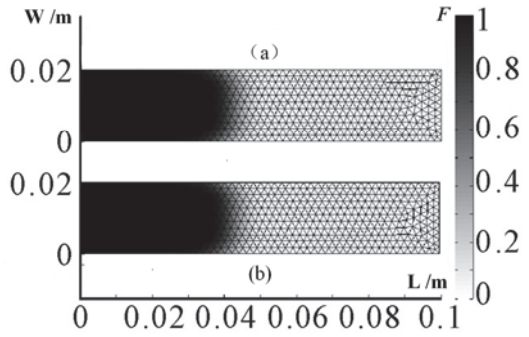

Fig. 3-7.1 W=20mm

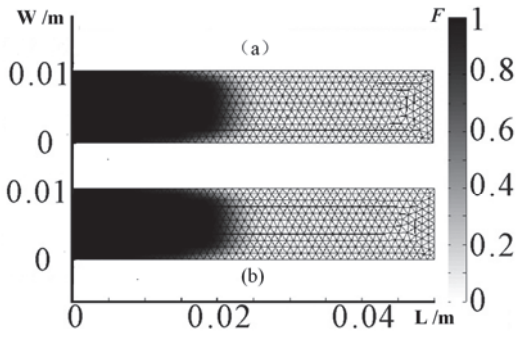

Fig. 3-7.2 W=10mm

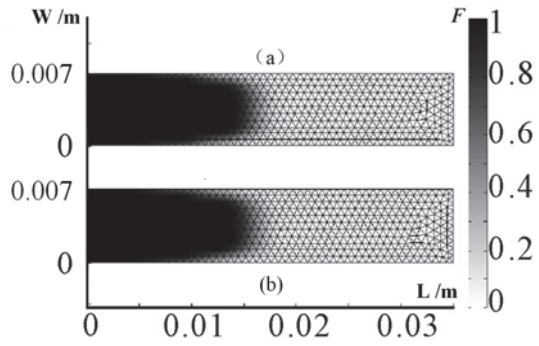

Fig. 3-7.3 W=7mm

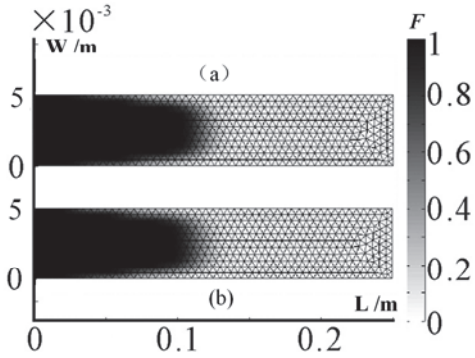

Fig. 3-7.4 W=5mm

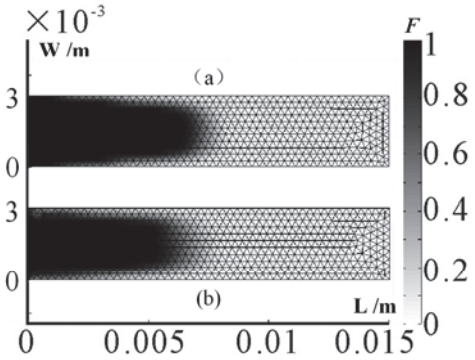

Fig. 3-7.5 W=3mm

Fig. 3-7 Results of injection filling states in molds of different sizes: (a) surface tension ignored; (b) surface tension included.

Fig. 3-7 (including 3-7.1 ~ 3-7.5) represents variation of the simulation results for filling state at different geometrical scales, with disregard and consideration of the surface tension term. The comparison of two results is labeled by (a) and (b) for the simulations of each size, respectively. The notation W and L are shown in Fig. 3-4. W is the width of mold inlet, and L = 5W is mold length.

Comparison of the simulation results for different sizes, shown in Fig. 3-7, provides variation of the surface tension effect according to the change in geometrical scale. All examples retain the same feedstock properties and same shear rate for the flow of feedstock. The evolutions of filling state are nearly the same for the examples with and without the surface tension term. Slight difference in curvature of the filling front surface is observed. The smaller the example is, the more obvious for the difference in surface curvatures. It indicates that the surface tension force impacts on the shape of filling front in injection molding process. The surface tension increases the curvature value of filling front. The results of simulation explain well the physics nature of surface tension, which tells that the surface tension induces contraction of the liquid surface. But it should be noticed that the surface tension term almost does not affect the filling of feedstock, for the size scales investigated in the present paper. The filling ratio in mold cavity at the same instant, with or without considering the surface tension effect, is shown in Table 3-2.

Table 3-2 Filling ratio in mold cavity at same instant with or without surface tension effect

Mold size W (/m)	$F_{(Filled)}$ % (without surface tension)	$F_{1(Filled)}$ % (with surface tension)	difference （$F-F_1$）%
0.02	42.718	42.6055	0.1125
0.01	42.994	42.8665	0.1275
0.007	43.1645	42.6422	0.5223
0.005	43.356	41.8267	1.5293
0.003	43.5102	38.8243	4.6859

The data in Table 3-2 indicates that surface tension effect has the tendency to slow down the filling process, within the scale of simulated examples. Although the difference between the filling ratios with or without surface tension effect is not significant for the example in ordinary sizes, it increases obviously when the mold size is decreased. This phenomenon can be also found in Table 3-3 and Fig. 3-8.

Table 3-3 Relation between mold size and maximal value of surface tension force

Width of mold W (/m)	0.02	0.01	0.007	0.005	0.003
Maximal value of surface tension force F_{b_max} (/N)	3.012	3.874	5.884	8.124	13.167

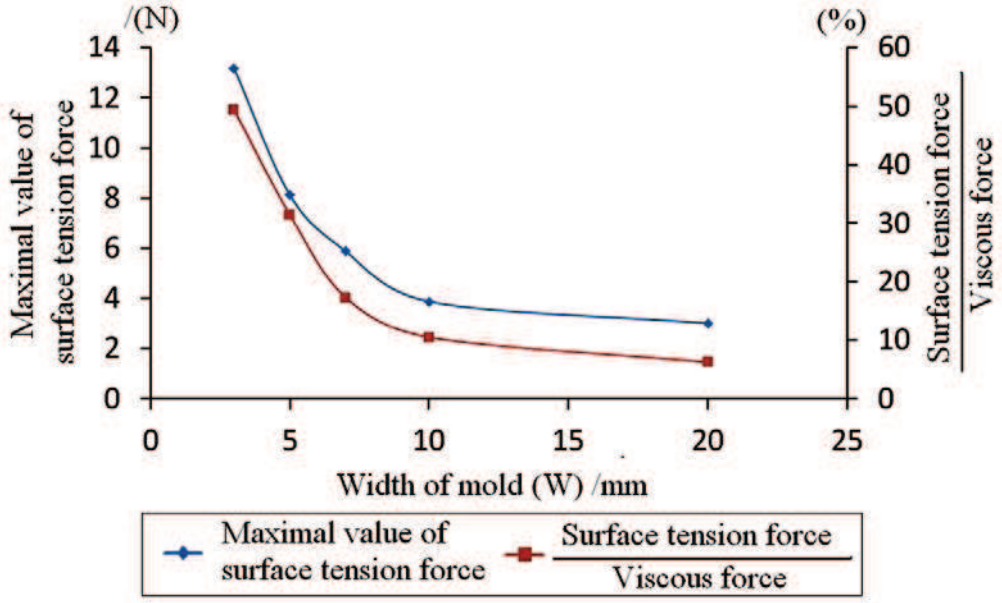

Fig. 3-8 Relationship of Mold width and surface tension effect

For the flow of small Reynolds number, filling front surface is governed by advection equation, advected by velocity field. The solution of velocity field is affected by viscous force and surface tension force. In order to evaluate and compare their effects on advance of the filling front, 10 nodes on filling front surface were chosen to compare the values of surface tension and viscous force. The average value of surface tension force and viscous force at 10 nodes was used to evaluate the effect of surface tension on evolution of the filling front surface, as shown in Table 3-4.

Table 3-4 Average values of surface tension force and viscous force in the molds of difference sizes

Width of mold W (/m)	Surface tension force F_{st} (/N)	Viscous force F_{σ} (/N)	Proportional relationship (F_{st} / F_{σ})
0.02	2.889	46.077	6.27%
0.01	3.643	34.629	10.52%
0.007	5.239	30.248	17.32%
0.005	7.587	24.132	31.44%
0.003	10.056	20.377	49.35%

From Table 3-3, Table 3-4 and Fig. 3-8, it can be also found that the surface tension effect increases obviously when the mold size decreases. Especially for the case of mold width W=3mm, the average value of surface tension force represents nearly half of the viscous force. However, surface tension force distributes only on the filling front surface in a thin layer of elements (see Fig. 3-6). Its effect on filling of the feedstock is small. But it plays an important role for the shape of filling front. Moreover, the value of surface tension increase quickly when size of the mold decrease to the scale range of micro injection. Its value may exceed the value of viscous force then become the dominating factor on the filling front. This conclusion agrees well with the work of Chien-Te Li et al. [110], who investigated the effects of gravitation and surface tension on the evolution of flow front in injection of the center-gated disks.

To validate the conclusions above, other three models with more complex cavities are specially designed for the simulation, as shown in Fig. 3-9. All of them have variation of the cross sections along the flow paths. In order to learn the surface tension effect on evolution of the filling state in each of the models, two similar cases are used to make the comparison work. All conditions are set to be the same for these two cases except the consideration or not the surface tension effect. The same pressure is imposed on the inlet boundary. The surface tension effects can be observed by the difference between two filled ratios versus time, as shown in Fig. 3-9.

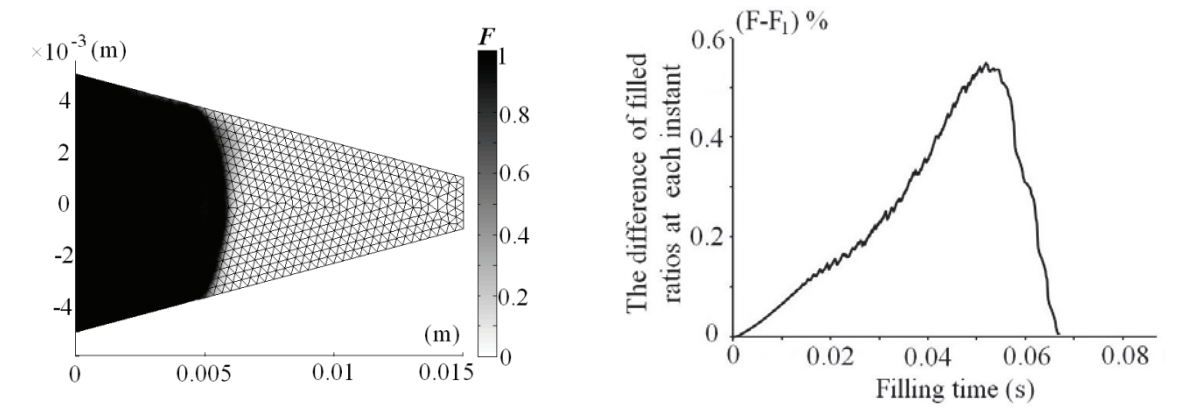

(a)

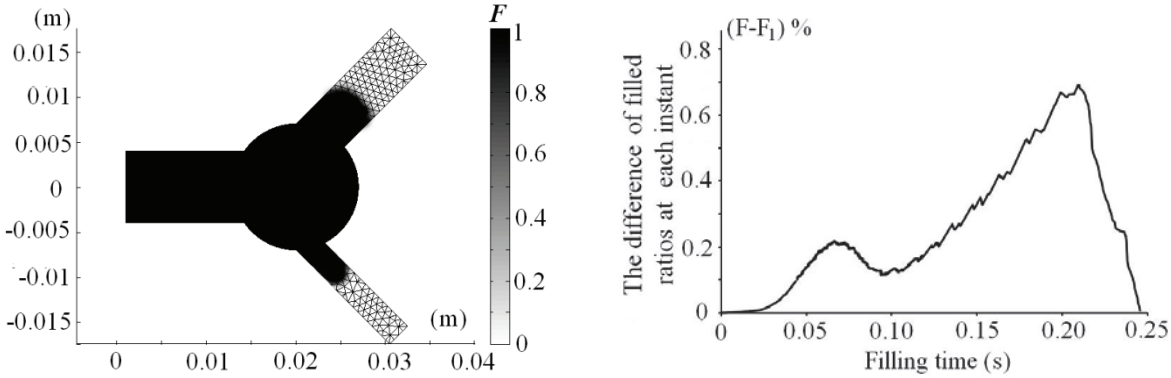

(b)

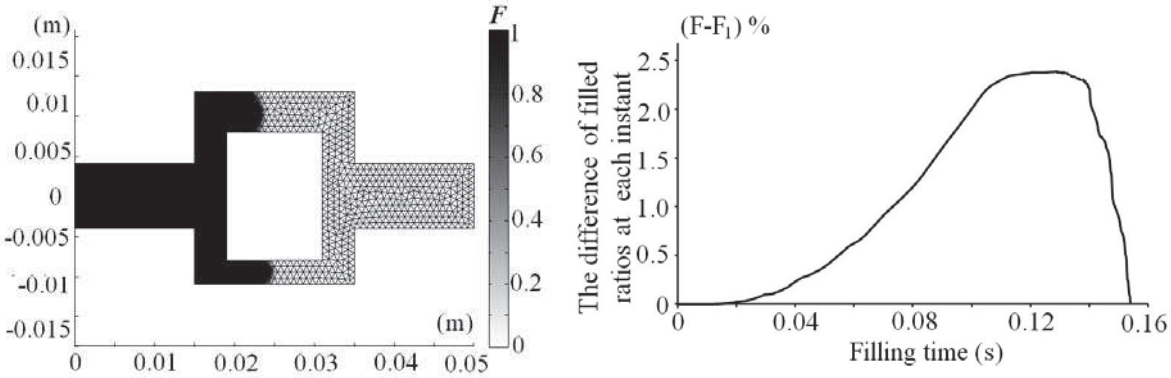

(c)

Fig. 3-9 Three models for validation of the surface tension effect in different mold sizes

From Fig. 3-9, the variational trend of surface tension effect according to the mold sizes is obvious. All of the three cavities have the variation of cross secrion from a bigger one to the smaller branches. It makes accordingly the difference of filled ratios at different instant for the cases with or without surface tension effect. The difference in filling ratios of these

two cases is growing from a very low value to the peak value until one of them getting to the fully filling state, then the other case continue to fill untill difference of the filling ratios become zero. However, we should also notice that although the growing of difference is obvious, but the magnitude of difference is small, at most 2.5%. So we can still conclude that the surface tension effect is not so important for injection filling of the sizes in these analysis.

3.5 Conclusion

In this Chapter, the effect of surface tension is implemented in an explicit finite element solver. A simple and systematic scheme is proposed and realized to fit the requirement of finite element methods. The Laplacian operation of filling function is realized by a two-step vectorial procedure to evaluate curvature of the filling front. The results are introduced directly into the source term of surface tension force in the solution of Navier-Stokes equations. According to the continuum surface force (CSF) model [111], the force of surface tension is distributed in a thin layer of the elements, which locates on the filling front of injection flow. A series of the examples for filling flow at scales of different dimensions are realized by the developed software with the ability to take into account the effect of surface tension. These examples prove that the importance of surface tension term increases when the mold size decreases. The surface tension can be neglected in ordinary injection molding, but it plays the significant role for the problems in sub millimeter sizes.

Chapter 4 Brief Introduction and Foundational Theories for Sintering

4.1 Introduction of sintering

4.1.1 Berif introduction of sintering

Sintering is a widely used processing technology in powder metallurgy and ceramic industries. It is a heat treatment applied to a powder compact in order to improve strength and integrity by bonding together the particles [114]. It might best be described as the synthetic manufacture of solid products using controlled heating of powdered raw materials. Hausner [115] proposed the definition of sintering as follows “sintering is the bonding of particles in a mass of powders by molecular or atomic attraction in the solid state, by application of heat, causing strengthening of the powder mass and possibly resulting in densification and recrystallisation by transport of materials”. Kuczynski [116] defined sintering as diffusional creep under action of capillary forces. According to the ISO definition of sintering, it is the thermal treatment of a powder or compact at the temperature below the melting point of the main constituent. The proper temperature is ordinarily 2/3 the melting point of the particular material. For materials that have high melting points such as molybdenum, tungsten, rhenium, tantalum, osmium and carbon, sintering is one of the few viable manufacturing processes. During sintering the green bodies shaped by die pressing, injection molding, slip casting, extrusion or spraying undergo the shrinkages in dimension and the final high dense or full dense products are obtained. It is based on atomic diffusion. The atoms in the powder particles diffuse across the boundaries of the particles, fusing the particles together and creating one solid component, as shown in Fig. 4-1.

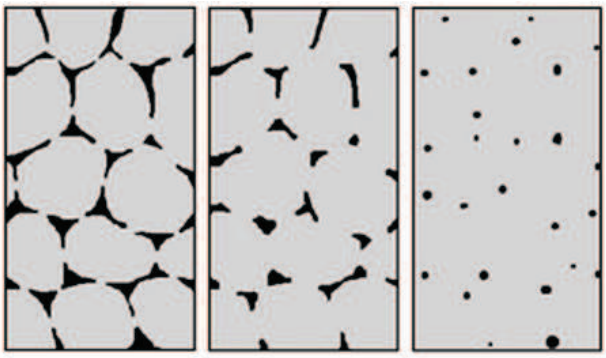

Fig. 4-1 The three stages of solid state sintering: left: initial stage, centre: intermediate stage, right: final stage (Courtesy EPMA) [117]

4.1.1.1 The history of sintering

Sintering is well established as a component fabrication approach. It has been applied to ceramics for 26 000 years. Sinter plants were constructed for iron ore induration starting in the 1860s. By 1871, the term showed up in archival literature with reference to bonding minerals. Subsequently, sintering was widely used to describe ore agglomeration. Before 1900, most of the publications simply called it firing. Metal sintering was evident in the early 1900s. For ceramics, sintering was initially reserved to describe the agglomeration of powders. Then, sintering was used in the technical ceramics literature starting in 1939. After the Second World War, sintering was broadly used to describe the heating of particles to produce components. The first published reports on sintering started in 1829 for platinum. Now, more than 20 000 archival publications are issued each year on sintered materials. About 40% of these literatures are on iron and steel, cemented carbides or alumina based ceramics. Engineering materials commonly processed by sintering are alumina, tool steels, steels, cemented carbides, stainless steels, titanium, copper, silicon nitride, titanates and zirconia. In recent years, sintering has propagated into a wide range of nanoscale powders which extend the small device applications into the electronic and biomedical fields.

4.1.1.2 The advantages of sintering

The advantages of sintered products over stamped, forged, or molded products include higher purity of raw materials, the maintenance of purity through the manufacturing process, the stability of repetitive steps in manufacture, and the uniform density of the item produced.

Obviously, advancements in technology ensure a more cost-effective manufacturing of higher quality sintered products.

4.1.1.3 The essential sintered methods

There are two essential methods of sintered manufacturing. By mass transport mechanisms at the atomic level, it can be devided into solid state, and liquid phase sintering [118]. The sintering proceeded by solid-state diffusion falls into solid-state sintering. Most polycrystalline materials are sintered by this type of the process. As similar, the liquid phase process introduces a transient liquid phase that can improve the mass transport rate. Liquid phase sintering is generally easier and more cost-effective than solid state.

In addition to the convenstional sintering method by resistance heating, there exist many new sintering ways to meet the requirments of fast sintering with high heating rate and temperature, such as Microwave Sintering [119], Selective Laser Sintering [120], Spark plasma sintering [121] and Self-propagating Sintering [122].

Microwave sintering has emerged in recent years as a new method for sintering a variety of materials. It has shown significant advantages against conventional sintering procedures. It is different from the conventional methods where heat is transferred between the objects by conduction, radiation and convection. It is a process in which the materials couple with microwaves, absorb the electromagnetic energy volumetrically, and transform it into heat, then sintered the powder materials. It is now widly used in sintering ceramics, semiconductors, inorganic and polymeric materials. But there are still many unknows about its heating principle, its reaction with sintered materials and the effects of proceeding factors to manufacturing process. In the later research in chapter 5 and Chapter 6, we investigate microwave sintering from both experiment and simulation aspects.

Selective Laser Sintering uses a laser to sinter powder based materials together, layer-by-layer, to form a solid model. The system consists of a laser, component chamber, and control system. This technology is ideal for durable, functional components with a variety of applications and capable of producing snap fits and living hinges. It suits for materials including: Nylon (Duraform PA), Glass-Filled Nylon (Duraform GF), Flame

Retardant Nylon and Durable Nylon (Duraform EX).

Spark plasma sintering, also known as field assisted sintering process or pulsed electric current sintering [123], is a sintering technology. The main characteristic of this sintering method is that the pulsed DC current directly passes through the graphite die, as well as the powder compact, in case of conductive samples. Therefore, the heat is generated internally, in contrast to the conventional hot pressing, in which the heat is provided by external heating elements. This facilitates a very high heating or cooling rate (up to 1000 K/min), hence the sintering process is generally very fast (within a few minutes). The general rate of process ensures its potential of densifying powders with nanosize or nanostructure, because it can effectivlly avoid coarsening phenomenon which accompanies with standard densification routes.

Self-propagating high-temperature synthesis is a method for producing inorganic compounds by exothermic reactions, usually involving salts. A variant of this method is known as solid state metathesis. Since the process occurs at high temperatures, the method is ideally suited for the production of refractory materials with unusual properties, for example: powders, metallic alloys, or ceramics with high purity, corrosion resistance at high temperature or super hardnessity.

In this research work, pressureless solid-state sintering is used to densify the PIM components. This chapter reviews the literatures on the theory of solid-state sintering.

4.2 Foundational Theories for Sintering

4.2.1 Driving Forces of Sintering

In most cases, the density of a collection of grains increases as material flows into voids, causing the decrease in overall volume. Mass movements that occur during sintering consist of the reduction of total porosity by repacking, followed by material transport due to evaporation and condensation from diffusion. In the final stages, metal atoms move along crystal boundaries to the walls of internal pores, redistributing mass from the internal bulk of

the object and smoothing pore walls.

The driving force for densification is the impetus to reduce the free energy in particle surfaces, the externally applied pressure and the chemical reactions [124]. In the present research, sintering is performed without the external pressure or chemical reaction. Fig. 4-2 is the two-sphere sintering model to show the formation of interparticle bond, and the reduction of the free solid-vapor interfaces at the contact area between the two particles. It forms new but lower-energy solid-solid interfaces between the particles with a total decrease in surface energy by removing the free surfaces.

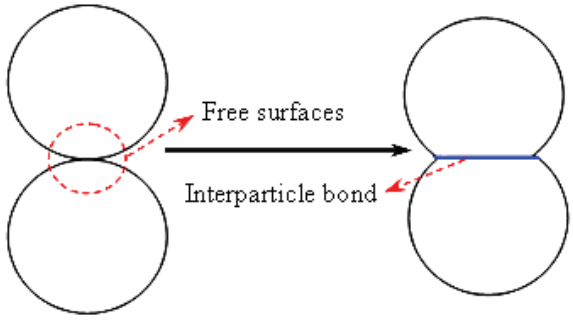

Fig. 4-2 Two-sphere sintering model showing that the reduction of the free energy during sintering by the formation of interparticle bond [14].

On the other hand, the elimination of the grain boundary area via grain growth or coarsening can also lower the free energy of the sintering body, as shown in Fig. 4-3.

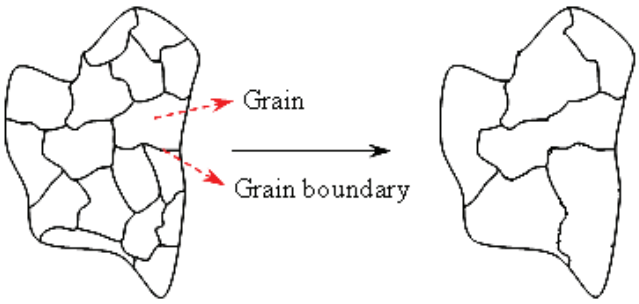

Fig. 4-3 Grain growth reduces the free energy of the sintering body by eliminating the grain boundary area [14].

4.2.2 Sintering Mechanisms

Sintering mechanisms have been discussed by various workers mainly under two categories [125]:

- Plastic deformation mechanism;
- Diffusion mechanism.

Sintering in practice is the control of both densification and grain growth. It occurs by diffusion of atoms through the microstructure. This diffusion is caused by a gradient of chemical potential – atoms move from an area of higher chemical potential to an area of lower chemical potential. The different paths the atoms take to get from one spot to another are the sintering mechanisms. The six common mechanisms are:

- Surface diffusion – Diffusion of atoms along the surface of a particle;
- Vapor transport – Evaporation of atoms which condense on a different surface;
- Lattice diffusion from surface – atoms from surface diffuse through lattice;
- Lattice diffusion from grain boundary – atom from grain boundary diffuses through lattice;
- Grain boundary diffusion – atoms diffuse along grain boundary;
- Plastic deformation – dislocation motion causes flow of matter.

1–3 above are non-densifying. They take atoms from the surface and rearrange them onto another surface or part of the same surface. These coarsening mechanisms lead to neck growth without producing the densification. They are in the form of surface diffusion, evaporation condensation and volume diffusion from the surfaces. 4–6 above are densifying mechanisms. Atoms are moved from the bulk to the surface of pores thereby eliminating porosity and increasing the density of the sample. It includs grain boundary diffusion and volume diffusion from the grain boundaries. In addiction, plastic flow occurs when the sintering stress larger than the in-situ strength of the sintering body. It can result in the rapid densification [126]. Fig. 4-4 shows the various mass transport paths during sinter bonding in a three particles model.

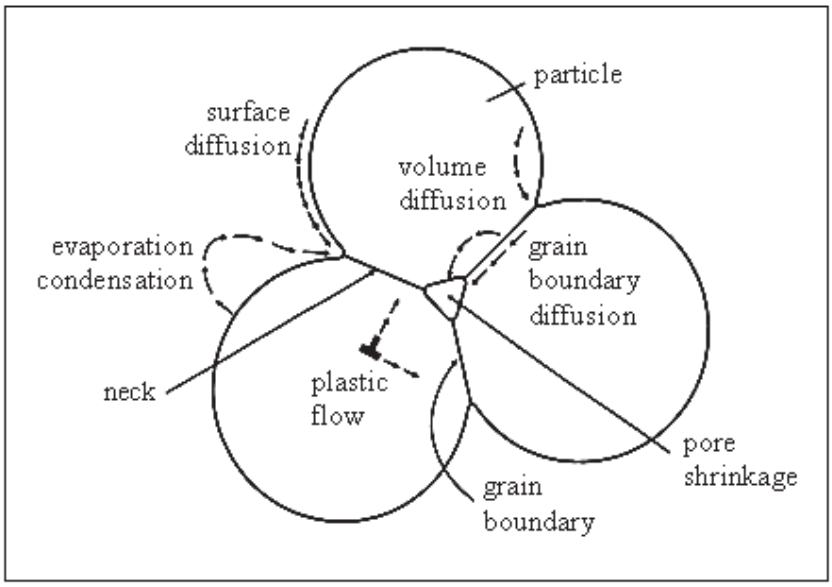

Fig. 4-4 Neck growth among three particles to show various mass transport paths during sinter bonding [9].

4.2.3 Stages of Sintering

The different stages during the sintering process are sketched in Fig. 4-5.

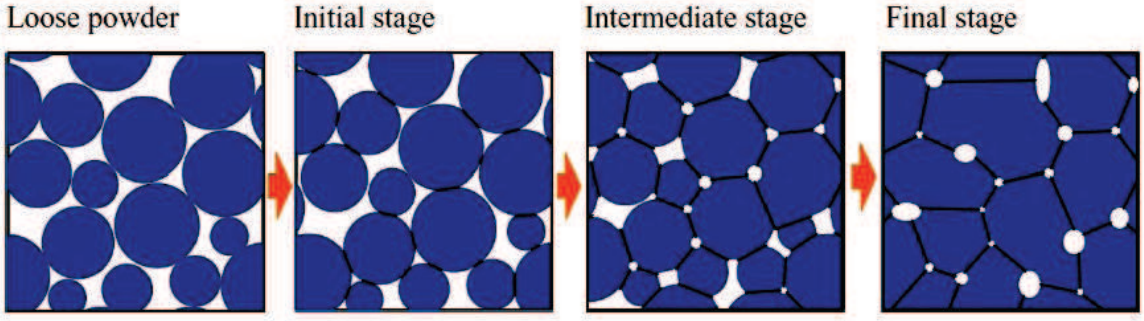

Fig. 4-5 Illustration of the microstructure evolution during the solid state diffusion sintering stage [9].

The debinded components are sintered by solid state diffusion. It can be divided into three stages, based on the geometry of microstructures. There is no clear-cut distinction between the stages, but each stage can be described by their general characters. At the beginning of sintering, powders are in loose state. In the initial stage, the sintering necks are

formed at the contact area and begin to growth by the diffusion process. The shrinkage occurs during the initial stage is about 4%. In the intermediate stage, the pores are rounding and interconnected at the grain boundaries. It undergoes rapidly the densification by reducing the cross section of the cylindrical pores. The final stage is characterized by the isolated pores located at the grain corners. It is also known as the grain coarsening stage.

A typical sintering cycle by solid state diffusion for stainless steel feedstock is given in Fig. 4-6, which is composed by four main steps: thermal debinding, emergence of neck growth, reduction of oxide diffusion and sintering.

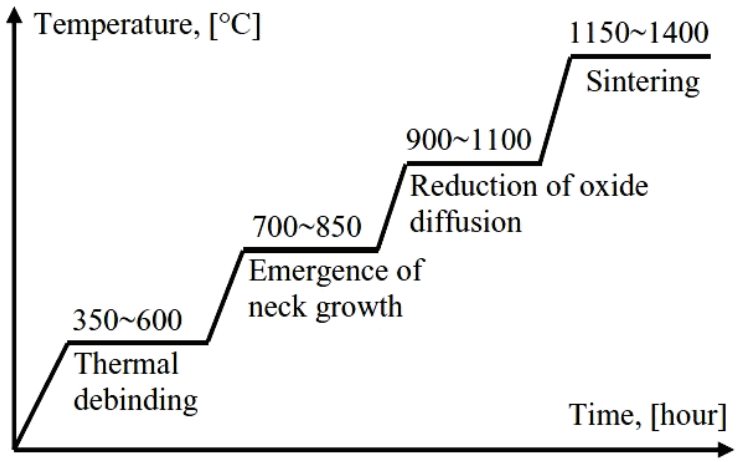

Fig. 4-6 Typical (solid state diffusion) kinetic sintering cycle for stainless steel feedstock with four segments [21].

4.3 Models and Simulations of Sintering

4.3.1 Simulation history

Sintering is an important process to produce the metallic and ceramic powder products. It dominates the final dimensions and mechanical properties. On the other hand, sintering is a complicate process that involves many physical and chemical phenomena. The mechanisms of sintering have not been totally understood yet. The geometrical accuracy and mechanical properties of the final components after sintering depend strongly on the choice

of process parameters in different stages, such as heating rate, peak temperature, holding time, sintering atmosphere and initial density. The introduction of simulation work can be used to optimize and to understand the sintering process better and improve the quality of sintered components. It could be a faster alternative in optimizing entire industrial processes compared to the conventional method of trial and error. The determination and optimization of process parameters have motivated numerous research works, as it needs deep knowledge on different processes and accurate modeling methods for each stage.

Researches on modeling and numerical simulations of the sintering process have been carried out for more than 50 years. The histories, development, achieved performance and the remaining barriers of sintering simulations were reviewed by German [127]. About every ten years the field takes a new turn, and in simple form the history of sintering simulations is as follows:

- 1960 to 1970: numerical simulations of two-particle neck growth in sintering;
- 1970 to 1980: multiple mechanism calculations of one-dimensional shrinkage;
- 1980 to 1990: predictions of density including pressure-assisted sintering;
- 1990 to 2000: continuum mechanics and finite element simulations of shape and size;
- 2000 later: control programs with hybrids of simulations and artificial intelligence.

4.3.2 Three sintering models

There is no unique classification of the various established models of sintering. According to the major approach of the modeling process, there are three kinds of distinguish models of sintering: (i) microscopic model (physically-based), (ii) mesoscopic model (stereological) and (iii) macroscopic model (phenomenological) [128].

4.3.2.1 Microscopic Models

The microscopic models aim to simulate the mass transport mechanisms between several particles. Sintering is treated as a collective result of thermally activated adhesion processes which result in the growth of contacts between particles. A number of

micromechanical models of sintering are based on a particle representation of porous powder material undergoing the sintering process. The most successful approaches to understand the mechanisms of neck growth and shrinkage are the two-sphere model due to Frenkel [129] and Kuczynski [130] for the early sintering stages (particle bonding), as shown in Fig. 4-7. The two-particle model has been extrapolated for the intermediate shrinkage state by Kingery and Berg [131]. Coble [132] developed a cylindrical pore model (as shown in Fig. 4-8), a spherical pore model for the late sintering stages (as shown in Fig. 4-9) was developed by MacKenzie and Shuttleworth [133]. More sophisticated models taking into account the superposition of various sintering mechanisms have been developed by Ashby [134], Arzt [135], and Exner and Arzt [136]. Until recently, simulation of microstructural evolution of large systems was not feasible due to the computer power limitations. It is becoming increasingly possible to simulate microstructural behavior of large systems, and this development is paving the way for embedding microstructural evolution into macroscopic models.

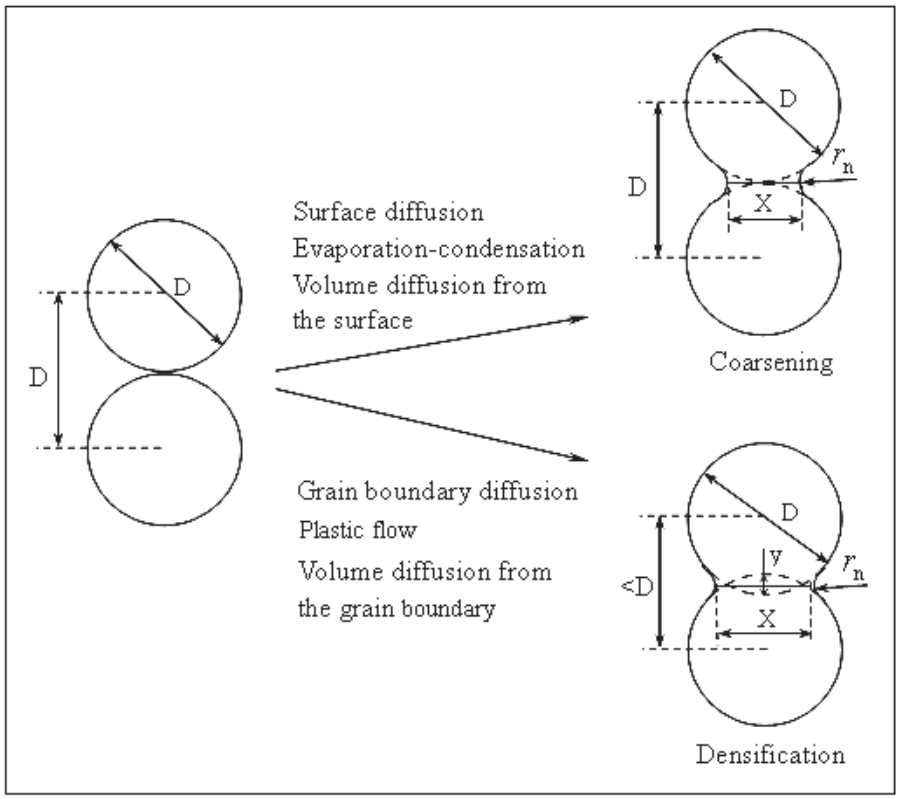

Fig. 4-7 Geometries of the two-sphere model to describe the neck growth and densification in the initial sintering stage. (D is the diameter, X is the diameter of the neck, r_n is neck surface radius, and y is the overlap distance.) [24]

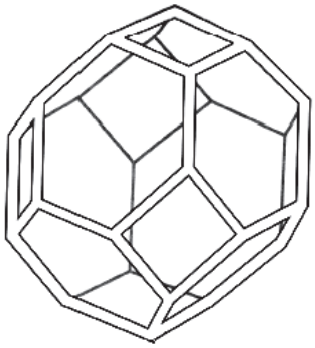

Fig. 4-8 The interconnected pores in cylindrical shape located on the boundaries of tetrakaidecahedron grains in the intermediate stage of sintering [24].

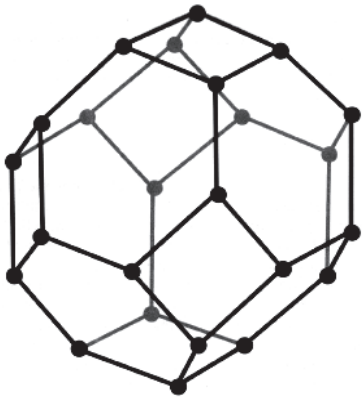

Fig. 4-9 The isolated spherical pores located at the corners of boundaries of tetrakaidecahedron grains in the final stage of sintering [24].

4.3.2.2 Mesoscopic Models

The mesoscopic models choose the representative cell or element in the sintering body, and simulate the microstructural evolutions including densification and grain growth. The mechanical properties of sintered components are determined by the material characters in mesoscopic level such as grain size, pore shape and distributions. A mesoscopic model of sintering capable of simulating large powder compacts could be a step to more realistic macroscopic models. However, although great progress has been made in the last 50 years in understanding microstructural evolution during sintering, current models of sintering [137-139], still consider highly idealized geometries with limited number of circular or spherical particles. While these models have provided much insight into the sintering process by predicting shrinkage rates, geometric changes in the particles and other information, their

ability to predict characteristics of a complex powder compact is limited.

4.3.2.3 Macroscopic Models

In the continuum approach, the porous powder under compaction is treated as a continuous medium at the macro-scale. It is close to the industrial application due to its merit in predication of the dimensional shrinkages and distortions of the sintered bodies. The deformation behavior of sintered bodies is described by constitutive equations based on modified theory of solids. The macroscopic behavior of sintered materials is a result of a complex combination of elastic, viscous, plastic and thermal deformation depending on the processes at the microscopic and atomistic levels [140]. Different mechanisms dominate the deformation behaviors at different stages of a powder metallurgy process. Constitutive equations of continuous media belong to the class of phenomenological models in which model parameters are obtained by fitting experimental data. Well-known phenomenological sintering models are those developed by Abouaf et al. [141], Duva and Crow [142], and Cocks [143]. Phenomenological approaches have been summarized by Olevsky [114], Cocks [144] and German [24]. Phenomenological theories do not take microstructure of the material into consideration. More recent analytical and numerical models of sintering make fewer assumptions. They are able to treat the details of shape change, shrinkage rate or other characteristic more accurately in a sintering compact.

There are many achievements of each kind of the sintering models, but neither of them is perfect. Most of the existing models are based on the spherical particle shape, cylindrical or spherical pore shape. It is much different from the real situation in the sintering process. Moreover, some phenomena occurring at the microstructural level and the non-thermal mechanical factors should be considered, such as phase transition, chemical reaction, influence of sintering atmosphere, oxidization phenomena and in-situ damage criteria etc. The most important thing, effective links are required between the microscopic, mesoscopic and macroscopic models.

Researches for sintering simulation are continued. The model used to simulate sintering in this work is based on the phenomenological macroscopic model. The most widely used linear viscoplastic constitutive law will be introduced in detail later in Chapter 6.

Chapter 5 Efficient sintering of 17-4PH stainless steel powder by microwave

As a new but fast developing technology, microwave sintering represents significant theoretical and industrial values. The heating of microwave sintering is a process in which the microwave energy is absorbed by the sintered materials. The energy is transformed into the kinetic energy of molecules, and thermal energy in the materials. It exhibits the important potential of rapid processing with high production efficiency [145]. Microwave heating is a sensitive function of sintered materials. Microwave penetrates into the media in the form of electro-magnetic waves, and results in the heating by transforming energy into heat. The heat is generated inside the materials, together with the vibration of the microwave in high frequency, which increase the kinetic energy of molecules and ions in the materials. The diffusion effect of densification is then increased, too. These properties are very advantages to improve the properties of final sintered materials in the micro and meso scales [146]. Moreover, microwave heating is selective [147] and pollutionless [148], it can be then widely used in the actual productions.

As a combination of powder metallurgy and microwave heating technology, microwave sintering has been extensively studied in experimental works. Takahashi et al. [149] manufactured zirconate titanate actuator in 2001; Anjana et al. made some researches on $Ce_2(WO_4)_3$ ceramics with low temperature [150]. Since 1999, when Roy et al. [151] sintered powdered-metals successfully in a microwave field, a wide range of standard powdered metals have been sintered by microwave heating. Author's teams have long-term experiences in Micro-PIM technology, which focuses on feedstock characterization and elaboration [152], identification of physical material parameters [153], mathematical model proposed for bi-phase fluid flow [154] and experimental and numerical analysis on the conventional thermal sintering [155]. For further investigation of sintering mechanism under microwave heating, a microwave sintering furnace is equipped in the research team.

Because of its sole report and unfavorable conclusion, the study in this chapter is made on the realization of fully densified 17-4PH stainless steel compact by hybrid microwave

heating. The investigated factors include peak sintering temperature, holding time, heating rate, pre-sintering stages. The results are illustrated by final size shrinkage, relative density, hardness and microstructure. Comparative analysis is made with the sintering in conventional resistive heating furnace. The sintering by microwave takes one tenth of the conventional sintering time to get the better results. The optimal peak temperature is 150℃~200℃ lower. It results in the better densification, more homogeneous microstructure, higher mechanical properties, and more size shrinkage. The experiments proved a remarkable fact for microwave sintering of the 17-4PH stainless steel powder. The heating rate must be set to an order of 30°C/min. Lower heating rate leads to the poor results. The fast processing by microwave results in the gradient of mechanic properties in sintered bodies. The prediction, evaluation and purposes of the gradient properties induced by microwave leads the studies to the more precise and profound insights.

5.1 Research background

17-4PH is a type of martensitic precipitation hardening stainless steel with high mechanical properties [156]. By heat treatment, high yield strength up to 1100-1300 MPa (160-190 ksi) can be achieved. Besides that, it represents excellent corrosion resistance [157]. This versatile material is then widely used in the aerospace, chemical, petrochemical, food processing, paper and general metalworking industries [158].

Nowadays, most researches on sintering of 17-4PH stainless-steel focus on the ways by conventional resistive heating (CRH). Sung et al. [159] studied the effect of sintering temperature on its microstructure and mechanical properties; Ye et al. [160] investigated the densification behavior in the temperature range of 650–1050 °C; Simchi et al. [161] experimented with a bilayer structure and discovered that stain rate of 17-4PH were higher than that of 316L during the course of sintering; Imgrund et al. [162] also produced magnetic–nonmagnetic bimetals made of 316L/17-4PH and 316L/Fe powders by micro-metal injection molding and CRH sintering process.

Microwave (MW) heating results from the absorption by molecular vibration (rotating electric dipole/dipole reorientation) and ionic conduction of a portion of the energy

transported by an oscillating electric field [163]. The primary advantages [164] of microwaves sintering are (a) rapid kinetics leading to savings of time and energy [165], (b) rapid internal heating [166], (c) lower temperature synthesis [167], (d) fine microstructures and improved properties [168]. For MW method, many researches focused on other powder materials. Zheng et al. [169] prepared a novel celsian/yttrium silicate coating by microwave sintering on the surface of C/SiC composites. Chandrasekaran et al. [170] conducted microwave heating and melting of lead, tin, aluminum and copper with the aid of square shaped silicon carbide susceptor. Liu et al. [171] found that the addition of nanometer Al_2O_3 powder and MW sintering process resulted in a synergistic effect on improvement of microstructure and properties of alumina ceramics. Tang et al. [172] elaborated porous nickel titanium (NiTi) shape memory alloy by microwave sintering at relatively low temperature of 850℃ and short sintering time of 15 min. Mula et al. [173] investigated the applicability of microwave sintering to produce bulk metal-based nanocomposites with blend composition of $Cu_{99}Cr_1$, Cu94Cr6, Cu99Cr1– 4wt.% SiC and Cu94Cr6– 4wt.% SiC (average particle size 30 nm). Panda et al. [174] compared the effect of heating mode on the densification, microstructure, strength and hardness of austenitic (316L) and ferritic (434L) stainless steels. The superiorities of MW sintering were all conformed in these works.

However, only one investigation on the microwave processing of 17-4PH stainless-steel powder was found by the retrieves of literatures in the currently available resources. It was a preliminary study done by Bose et al. [175]. They found that MW sintering had not improved the mechanical properties compared to CRH sintering for 17-4PH stainless steel.

To understand better the sintering properties of the 17-4PH stainless steel, the present work examined the densification and microstructure evolution of 17-4PH stainless steel powder produced by MW sintering. The injected specimens subjected to 2.45 GHz microwaves in a mono-mode furnace. The influence factors were investigated, including the peak sintering temperature, holding time, heating rate and pre-sintering stages in microwave sintering process. After such a solid state sintering route [176], the evolutions of micro-structure，densification and mechanical response of the sintered specimens were

studied. Comparison of the results between MW sintering and CRH process was also studied.

In present research, the authors proved that the MW sintering process for 17-4PH stainless steel provides higher sintered density and fewer defects in micro structure. Then better mechanical properties are achieved. Meanwhile, it shortens greatly the sintering time, lowers the peak sintering temperature. Higher Vickers-hardness of MW sintered compacts was also detected in the present work. It is important to indicate that the mechanic properties behave gradiently in the sintered bodies, because of the rapid processing by internal heating. None of the specimens presents visually observable distortion.

5.2 Experimental procedure

The experimental specimens were made of 17-4PH stainless steel powder with average size 11μm. The micrometer-scaled particles can be observed by the optical microscope as demonstrated in Fig. 5-1. Chemical composition of 17-4PH stainless steel is shown in Table 5-1, according to standard AISI630.

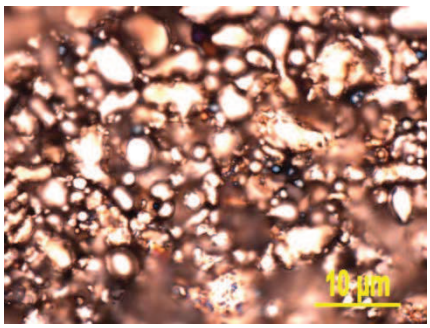

Fig. 5-1 Micrographs of 17-4PH stainless steel powder (average size 11μm) used in the subsequent tests, observed by optical microscope.

Table 5-1 Chemical composition of 17-4PH stainless steel (wt, %)

Fe	Ni	Cr	C	Cu	Nb	Mn	S	P	Si
71.8~73.8	3.0~3.5	15.5~17.5	≤0.07	3.0~5.0	0.45	≤1.0	≤0.03	≤0.04	≤1.0

In the present analysis, specimens in 17-4PH stainless steel powders were prepared by several processes [2] before MW sintering stage. The schematic illustration for all the steps

from powder to sintered components is shown in Fig. 5-2. The final sintering stage is represented by two possible ways: CRH or MW sintering. The green components, which based on 17-4PH stainless steel powder mixing with wax-based binders, were provided by © Beijing Jarain Powder Injection Tech., Co. Ltd. The density of green parts was approximately 5.05 g/cm^3, 64% of the density for pure 17-4PH stainless steel 7.89 g/cm^3. Before sintering, binders were burnt out in an electric thermal debinding oven. The first stage is to remove the water vapor absorbed inside. The injected components were heated from 20℃ to 130℃ with a heating rate 55℃/hour. This temperature is lower than that for decomposition of the paraffin wax. Then the temperature was increased up to 220℃ with a very slow heating rate 4.5℃/hour to eliminate the paraffin wax. Afterwards, the specimens were cooled for 2 hours to reach ambient temperature. This debinding cycle was also used by Quinard et al. [153] for the study of PIM feedstocks with 316L stainless steel powder (mean particle size 3.4 μm) to process the micro-components. Belgacem et al. [177] made an investigation on details of the thermal debinding process and identified the kinetic parameters for fine 316L stainless steel feedstock. In debinding process, 6.3% of the weight was reduced for the specimens. This preliminary debinding stage is necessary to prevent crack development in the next sintering stage [11].

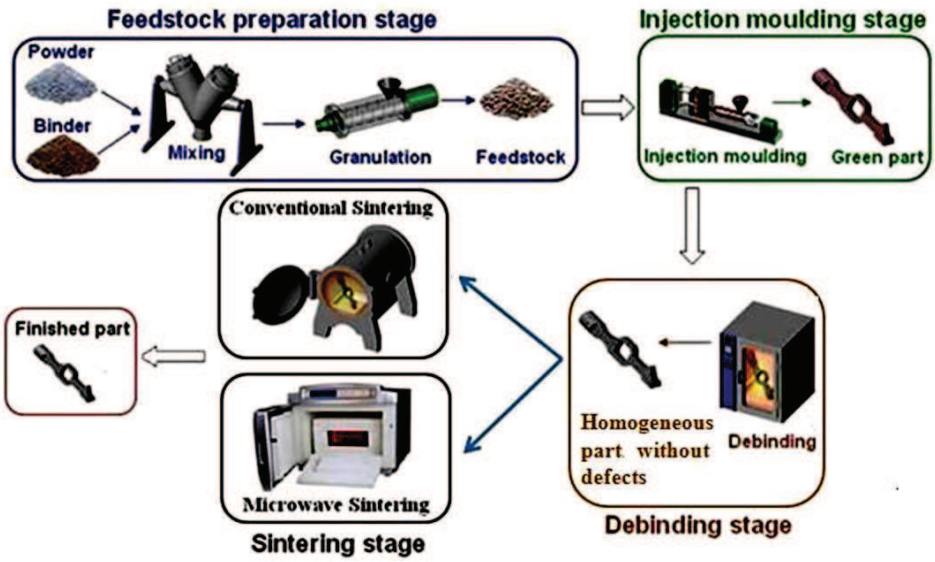

Fig. 5-2 The sequential stages to get the final sintered components [2]. The sintering stage may be processed by CRH or MW ways.

Metal powder shows poor coupling with microwaves in low temperature stage of

sintering [178], so a hybrid way of MW heating was used in the MW furnace (HAMilab-V1500). A flat SiC susceptor was placed under the powder compact and some chopped ones were put around it, according to the work of Kim-Hak et al. [179]. Surface temperature of the specimen was continuously measured by an IR pyrometer from an outside cavity window. In order to study the densification behavior under different heating modes, the same debinded components were also sintered by CRH in a vertical SETSYS® evolution dilatometer.

After sintering, size shrinkages of the sintered specimens were measured by calipers. Bulk densities were tested according to Archimedes' principle by immersing the samples into an ethanol based liquid. Afterward, the sintered samples were wet polished in a manual polisher. Then Vickers bulk hardness measurements were performed on the samples at 5 kg load with duration 10 s. To make the measurements more reliable, the hardness values took the averages of five readings at the spots near center of the prepared surfaces. Metallographic processes were employed in the microstructural analyses. 4% nitric acid solution and alcohol were used for etching the polished surface. Then optical microscope was used to observe the microstructure on polished and chemically etched surfaces of the specimens.

5.3 Results and discussion

5.3.1 Specimen sizes after being injected, debinded and MW sintered

Specimen sizes after being injected, debinded and MW sintered were compared in Fig. 5-3. It exhibits obvious size shrinkage after sintering, about 15% along the x direction. The polished section of the sintered component is shown in Fig. 5-4.

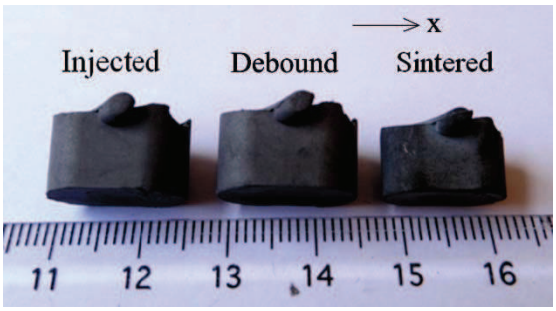

Fig. 5-3 Comparison of the sizes for the specimens in 17-4PH stainless steel powder after injection molding, thermal debinding and microwave sintering.

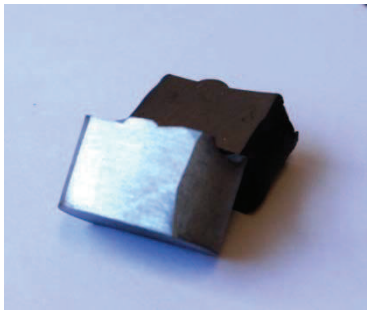

Fig. 5-4 Polished section of microwave sintered specimens in 17-4PH stainless steel powder

5.3.2 The influence factors in MW sintering process

5.3.2.1 Peak sintering temperature

In order to study the influence of peak temperature on sintering results, tests were made with different peak temperatures but other processing factors remained the same. Referring to the previous work by Quinard et al. [46] in research team on CRH sintering of 316L stainless steel, the heating processes include three steps. First the specimens were heated to 600℃, and then held the temperature for 30 minutes. Subsequently the temperature was increased to 900℃, and then held again for 30 minutes. At last the temperature is increased to peak values of the prescribed tests, and then held the peak temperature for 10 minutes. The same heating rate 5℃/min was applied to all test processes. The results for different peak temperatures are exhibited in Table 5-2.

Table 5-2 Comparison of size shrinkage (along x direction in fig. 3), relative density and Vickers-hardness obtained from specimen sintered with different peak temperatures (All processes with heating rate: 5℃/min and holding the peak temperature for 10 minutes)

Peak temperature (℃)	Size shrinkage (%)	Relative density (%)	Vickers-hardness (HV)
1100	5.67 ±0.001	72.6 ±0.01	173 ±0.1
1140	10.29 ±0.001	90.5 ±0.01	280 ±0.1
1150	12.47 ±0.001	90.9 ±0.01	311 ±0.1
1160	9.98 ±0.001	86.7 ±0.01	235 ±0.1
1200	8.12 ±0.001	81.2 ±0.01	267 ±0.1

It shows the evidence in Table 5-2 that suitable peak temperature will result in optimized results. For sintering of 17-4PH stainless steel powder by microwave, the optimal peak temperature is 1150℃, which results in the higher density and better mechanical properties.

5.3.2.2 Effect of holding time

In second batch of the tests, all samples were sintered to the same peak temperature 1150℃. The durations of holding time for peak temperature were varied for different tests. Other processing factors were retained the same as illustrated in 3.2.1. The sintering results for different holding times are shown in Table 5-3.

Table 5-3 Comparison of size shrinkage (along x direction in fig. 3), relative density and Vickers-hardness obtained from specimens by MW sintered with different holding time in the same peak temperature (All processes with heating rate: 5℃/min and sintered to the same peak temperature 1150℃)

Holding time (min)	Size shrinkage (%)	Relative density (%)	Vickers-hardness (HV)
5	8.81 ±0.001	85.9 ±0.01	238 ±0.1
10	12.47 ±0.001	90.9 ±0.01	311 ±0.1
15	8.32 ±0.001	84.6 ±0.01	253 ±0.1
20	8.19 ±0.001	83.4 ±0.01	277 ±0.1

The results showed in Table 5-3 indicate that there exists an optimal heating duration for peak temperature in microwave sintering. For the case of 17-4PH stainless steel powder, holding 10 minutes will result in the best solution for high density and mechanical properties.

5.3.2.3 Effects of heating rate

For third group of the tests, investigation was made by variation of the heating rates. The peak temperature and holding time were taken to be the optimal values determined by two above sets of tests. It represented the value 1150℃ for peak temperature and 10 minutes for holding time. For the purpose to focus closely our attention on heating rate, the specimens were heating directly to peak temperature from the ambient value, and then held it for 10 minutes. The heating rates were set for different values in different tests. The results of MW sintering for different heating rates are shown in Table 5-4.

Table 5-4 Comparison of size shrinkage (along x direction in fig. 3), relative density and Vickers-hardness obtained from specimen by MW sintered with different heating rates (All processes sintered to the same peak temperature 1150℃ and holding it for 10 minutes)

Heating rate (℃/min)	Size shrinkage (%)	Relative density (%)	Vickers-hardness (HV)
10	11.11 ±0.001	92 ±0.01	227 ±0.1
20	15.15 ±0.001	95 ±0.01	299 ±0.1
30	16.11 ±0.001	96.6 ±0.01	316 ±0.1
40	14.90 ±0.001	93.6 ±0.01	231 ±0.1
50	Specimen damaged		

From the results in Table 5-4, heating rate 50℃/min leads to damage of the specimen. The too fast heating rate results in uneven temperature distribution, which leads to the distortion or collapse. The lower heating rate may lead to grain coarsening, which results in lower density and lower surface hardness of the sintered products. A heating rate 30℃/min is shown to be optimal for MW sintering of 17-4PH stainless steel.

5.3.2.4 Pre-sintering temperature

Based on the above mentioned results, specimens were heated to peak temperature 1150℃ with heating rate 30℃/min, then holding for 10 min. Now the study on pre-sintering stage is realized. Before the formal sintering stage, the specimens were heated to a pre-sintering temperature, and then held for 30 min. The results for different pre-sintering temperatures are shown in Table 5-5. A test without pre-sintering was also realized to compare with the other processes.

Table 5-5 Comparison of size shrinkage (along x direction in fig. 3), relative density and Vickers-hardness obtained from specimen by MW sintered with different pre-sintering temperature (All processes heated with the same heating rate 30℃/min, sintering in the same peak temperature 1150℃ and holding it for 10 minutes)

Pre-sintering temperature (℃)	Size shrinkage (%)	Relative density (%)	Vickers-hardness (HV)
900	9.33 ±0.001	83.7 ±0.01	182 ±0.1
600	10.12 ±0.001	87.8 ±0.01	190 ±0.1
400	12.15 ±0.001	89.9 ±0.01	207 ±0.1
270	13.94 ±0.001	93.4 ±0.01	274 ±0.1
no pre-sintering stage	16.11 ±0.001	96.6 ±0.01	316 ±0.1

In Table 5-5, it is remarkable that the best result is obtained by the process without pre-sintering stage. If pre-sintering is really necessary for the purpose to get the initial stiffness, the lower temperature is used, the better quality can be obtained.

A conclusion can be drawn from the facts in section 3.2. The optimal choice in microwave sintering process for specimens in powders of 17-4PH stainless steel (powder size≈11μm) is shown in Fig. 5-5.

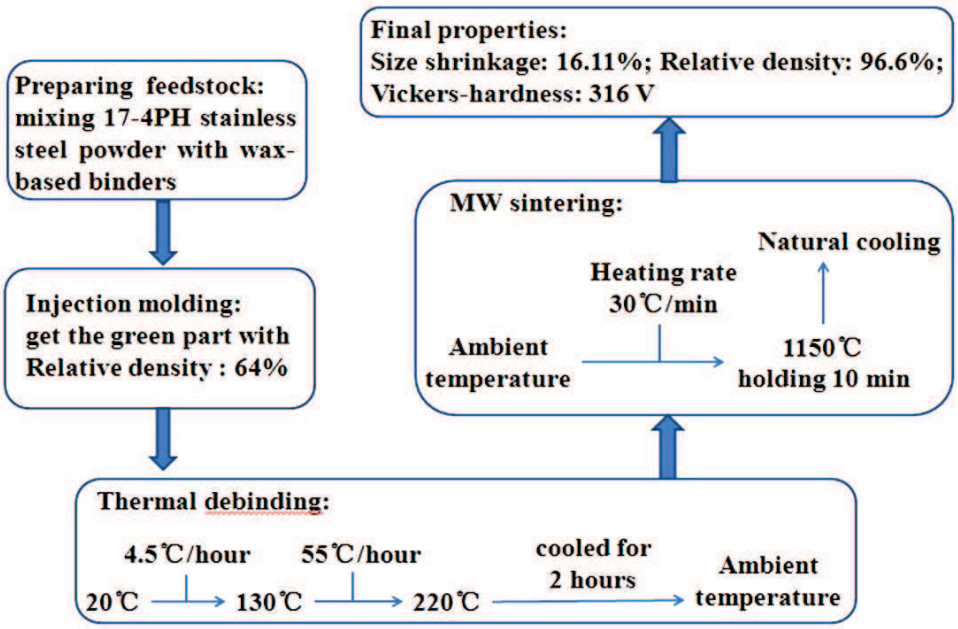

Fig. 5-5 The optimal process proposed for MW sintering of specimens in 17-4PH stainless steel powders.

5.3.3 Microstructure

The microstructure of sintered materials has been observed by optical microscope. For the purpose of clear observation, the specimens were polished and chemically etched for the observed areas. The sintering stage was interrupted at different temperatures, and left cooled to have the observation on the corresponded micro structures. When the peak temperature was reached, a holding time of 10 minutes was maintained. Evolution of the micrographs from powders to the sintered compacts is illustrated in Fig. 5-6.

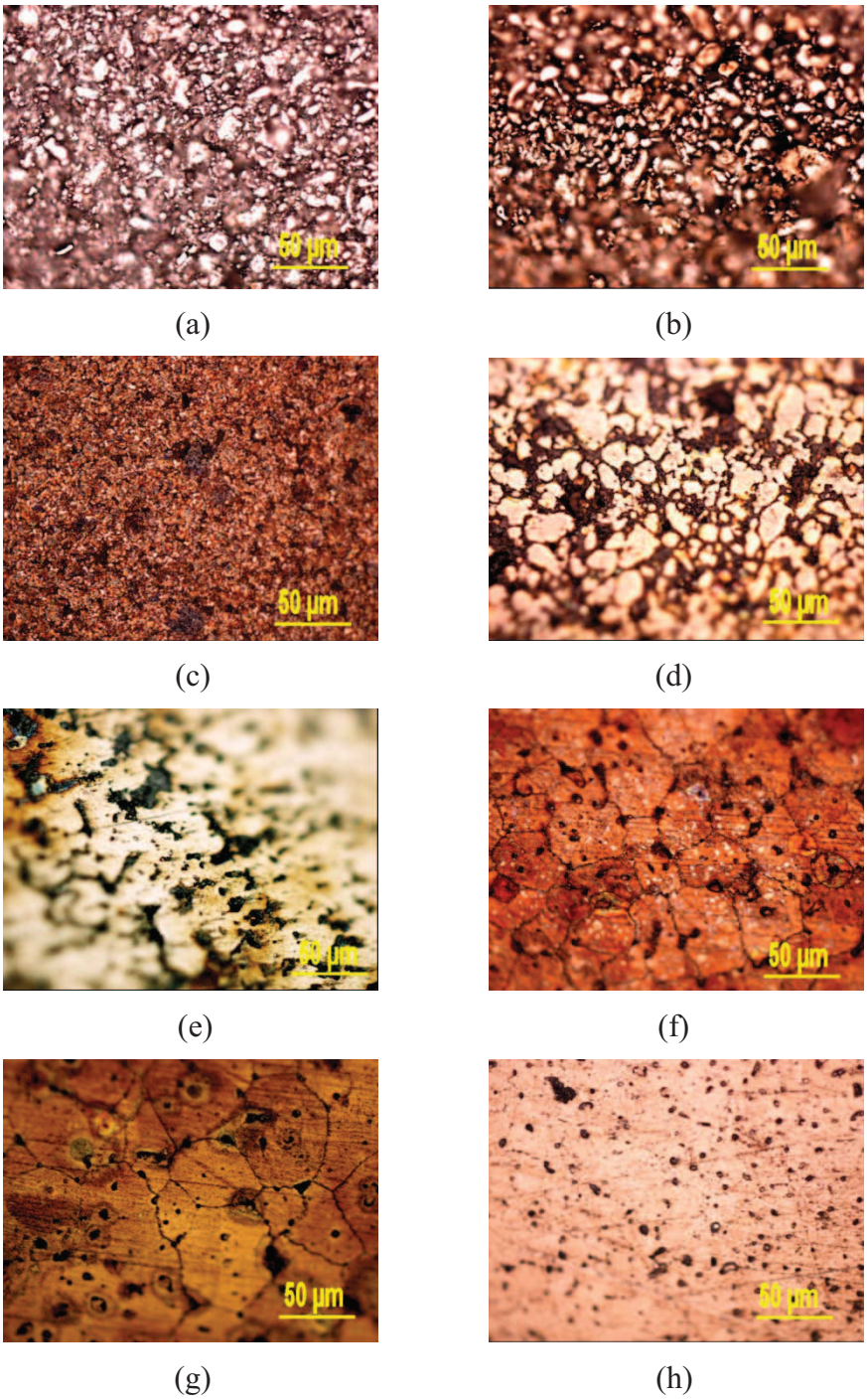

Fig. 5-6 Micrographs of the microstructure evolution for MW sintering of the 17-4PH stainless steel powders, observed by optical microscope: (a) injected, (b) debinded, then MW sintered at (c) 950℃, (d) 1000℃, (e) 1050℃, (f) 1100℃, (g) 1140℃, (h) 1150℃, holding for 10 min.

Fig. 5-6 depicts well the evolution process of particle crystallization. When sintered to 950℃, the as-sintered surfaces were porous and the samples exhibited small grain size. With

the increase of sintering temperature, the number of pores decreased, and the rate of grain growth increased apparently. From (f) and (g), the significant grain growth is obviously observed. Most of the larger holes locate at the grain boundary. It is favorable for evacuation of the gas entrapped in the porous powder compact and then benefit to the densification process. When the temperature reached to 1150℃ (h), the big pores were almost eliminated. This phenomenon affects directly the mechanical properties of final samples.

5.3.4 Distribution of the Vickers-hardness

In MW processing, heat is produced inside the bulk material, and sent out by radiation and convection on outer surface of the specimens. Then it takes place the thermal gradient. The temperature in core is higher than that on the surface. The outer surface at different positions of the specimen subjects to different variation of temperature, because of irregular shapes of the sintered body. The sintered material closer to the centroid is denser and represents generally higher mechanical properties. This phenomenon can be proved by detection of the hardness distribution over the polished cross section of the specimen.

Detection of hardness distribution on a plane section was realized by a specific scheme. A cross section near middle plane of the specimen was prepared. On the polished section plane, 9 small areas were arranged along a horizontal axis and a vertical axis, as shown in Fig. 5-7. They were labeled in the sequence from x1 to x5, and from y1 to y5. In each small area, 5 spots were tested. The average value of 5 test results was regarded as the formal hardness of the small area.

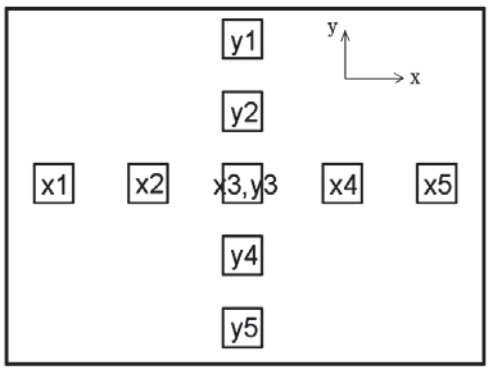

Fig. 5-7 Distribution of the detected areas in the polished section of sintered specimen for Vickers-hardness measurements

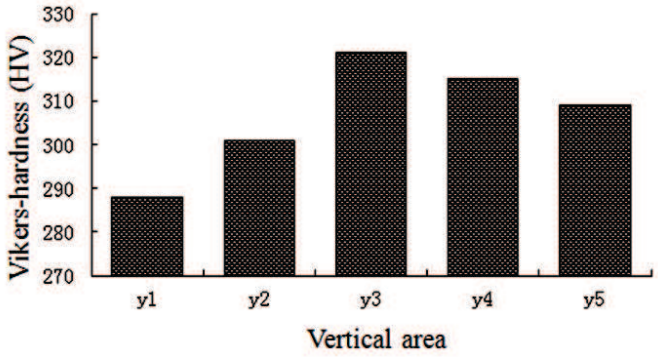

Fig. 5-8 Vickers-hardness values for each detected small areas along vertical direction

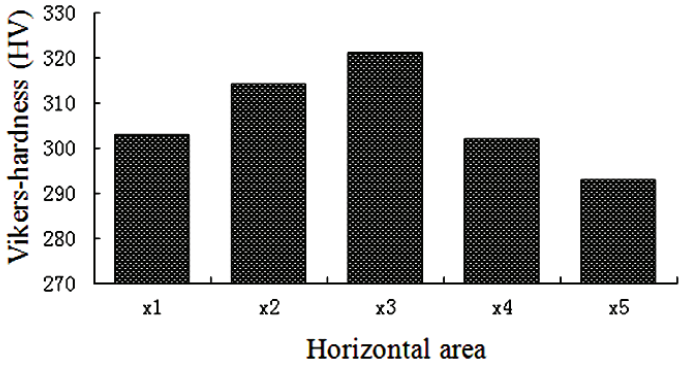

Fig. 5-9 Vickers-hardness values for each detected small areas along horizontal direction

As expected, experimental results in Fig. 5-8 and Fig. 5-9 prove well the nature of MW sintering. It is noticed that the values at symmetrical positions, said left and right, up and down, are not symmetric. The asymmetry in the values of Vickers-hardness was induced by the use of hybrid MW sintering. For example, the point y4, y5 in lower half were closer to the susceptor than the ones in upper half. Their distance closer to the assist-heating materials SiC resulted in better heating, and then greater values in Vickers-hardness.

Moreover, it is necessary to note that the difference in hardness values among these small areas is about 20~30 Vickers units, within such a small size compact. The gradient of mechanical property is obvious in the sintered bodies. It is due to the character of rapid heating in MW sintering. However, there is no available way to reduce the optimal heating rate. The lower heating rate results in the worse sintering quality, because of the grain coarsening. Then gradient of mechanical properties can be regarded as the nature of MW sintering. It represents the important value to study the relationship between evolution of temperature gradient and the gradient of mechanical properties in sintered products.

Prediction of the gradient in mechanical properties shows its potential significance in the studies of functionally gradient materials. The research on modeling and simulation of the property gradients in MW sintering is well expected.

It should be mentioned that none of the microwave sintered specimens exhibited the visually observable distortion. As the shape of studied specimens was not sensitive to the distortion, and no precise measurement was applied on their geometries, this conclusion is just an estimated one. The influence of temperature gradient on shape distortion should be made by specially designed specimens with the precise measurement on geometries.

5.3.5 Comparison with the conventional sintering

5.3.5.1 Sintering of 17-4PH stainless steel by conventional sintering (CRH)

In order to study and compare the densification behaviors, the same debinded components were sintered by CRH in a vertical SETSYS® SETARAM evolution analyser, too. These specimens were heated to peak temperature of 1350℃, then holding for 2h, with different heating rate of 5℃, 10℃, 20℃, 30℃/min respectively. According to the process proposed by Song [48], the temperature was held for 30 min when it reached 600℃ and 900℃ to ensure homogenization of the temperature in sintered body. The kinetic size shrinkages and shrinkage rates versus temperature are illustrated in Fig. 5-10 and Fig. 5-11.

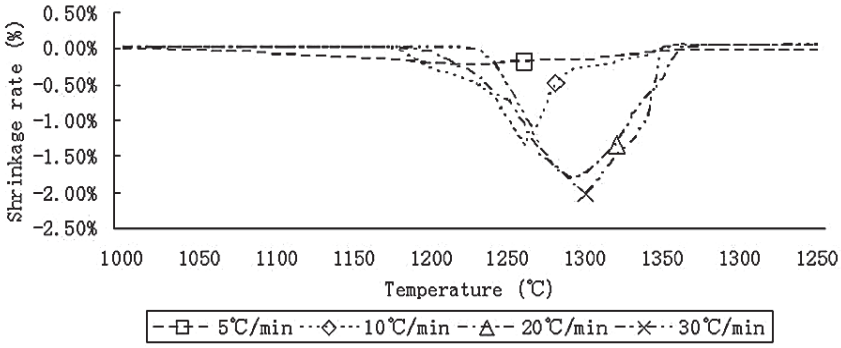

Fig. 5-10 Size shrinkage versus temperature during sintering for the specimens in 17-4PH stainless steel at different heating rates

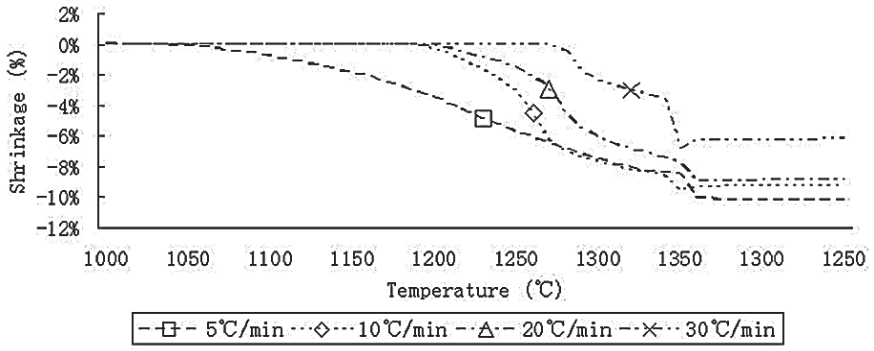

Fig. 5-11 Shrinkage rate versus temperature during sintering for the specimens in 17-4PH stainless steel at different heating rates

Fig. 5-10 and Fig. 5-11 illustrate that (a) higher heating rate leads to greater shrinkage rate but less shrinkage; (b) With higher heating rate, shrinkage happens at higher temperature, and the peak of shrinkage rate happens also at higher temperature.

5.3.5.2 Comparison between MW sintering and CRH sintering

According to the results in 3.5.1, two tests were chosen to make a comparison: (1) For CRH sintering: heated to 1350℃ with heating rate 5℃/min then held for 2 hours. During the heating process, the temperature is held for 30 min when it reached 600℃ and 900℃, respectively. (2) For MW sintering: heated directly to 1150℃ by heating rate 30℃/min, then held for 10 min.

Table 5-6 Comparison of sintering time, peak temperature and final properties of the specimens obtained by CRH sintering and MW sintering

Sintering mode	Sintering time (min)	Peak temperature (℃)	Size shrinkage (%)	Relative density (%)	Vickers-hardness (HV)
Conventional	445	1350	14.95±0.001	95.2±0.01	284±0.1
Microwave	48	1150	16.11±0.001	96.6±0.01	316±0.1

It demonstrates in Table 5-6 that: (1) The sintering of 17-4PH stainless steel compacts in a MW furnace represents 90% of reduction in processing time; (2) The optimal peak temperature for MW sintering is 150℃~200℃ lower than that for CRH sintering; (3) The

achieved size shrinkage, relative density and hardness of MW sintered material are larger than the values obtained by CRH sintering in dilatometer. The similar results are obtained by Charmond [167]. Their research found that MW sintered specimens in Y-Tetragonal Zirconia Polycrystal powder exhibited a larger final density than the CRH sintered ones at the same temperature. A reasonable interpretation for this positive MW effect on the densification of the material is that the oscillating electric field enhances the interface reaction [180].

The microstructure of 17-4PH stainless steel sintered by CRH is presented in Fig. 5-12. It is obviously observed that there are more and much larger gas holes in the specimen sintered by CRH than in the ones sintered by MW sintering, as shown previously in Fig. 5-6 (h). This phenomenon is due to the heating characters of CRH sintering. The Heat is conducted from outer surface to core of the specimen. The direction of heat conduction is opposite to the direction of outward gas exhaust. Outer layer of the powder is easier to be sintered. It obstructs then the paths of gas exhausting. Some of the gas is kept inside the specimen and then forms the large holes. The powder compact heated by microwaves is more homogeneous in microstructure despite the high heating rate. It represents well the advantage of volumetric heating by microwave. It is one of the important reasons why specimens after MW sintering are always with greater density, better surface quality and higher mechanical properties.

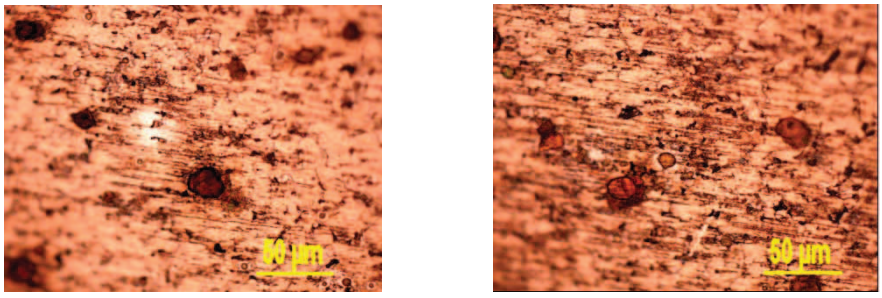

Fig. 5-12 Micrographs of the microstructure obtained from CRH sintering of specimens in 17-4PH stainless steel observed by optical microscope

5.3.6 Conclusions

In present studies, compacts based on 17-4PH stainless steel powder were successfully consolidated to nearly full density by hybrid MW sintering. The experiments were realized in a furnace of mono-mode cavity. The optimal heating cycle was determined by the experiments. The best result was obtained by heating directly from ambient temperature to 1150℃ with heating rate 30℃/min, and then held 10 minutes. It got the specimen with higher density (relative density: 96.6%) and better mechanical properties (Vikers-hardness: 316V). The sintering of 17-4PH stainless steel powder by MW heating represents short processing time and lower peak temperature. It takes merely 10% of the conventional sintering time to get the better results. The peak temperature is 150℃~200℃ lower than that in the CRH sintering. Despite of high heating rates, the specimens did not display the observable distortion or cracking. It represents the important advantage of volumetric heating by MW. The MW sintering also represents better densification, more homogeneous microstructure, and higher mechanical properties. As higher density is achieved, the sintering by MW heating results in more shrinkage in size.

It is remarkable that sintering by MW heating resulted in the obvious gradient in mechanic properties of the sintered material, because of its rapid heating in the internal volumetric way. It is valuable to continue the studies on this nature for the application of MW sintered products. The modeling and simulation on generation of the gradient properties appears the significant insights for the further studies.

Chapter 6 Mathematical Modeling and Simulation of Microwave Sintering Process

6.1 Research Background

Microwave sintering represents the coupling phenomena of multi-physical fields. It includes the coupling of electro-magnetic fields, thermal conduction and the densification process of sintered powders. The true process of microwave sintering must be simulated under the condition that these complicated coupling are taken into account. Most of the actual literatures focus on the analysis of microwave heating. [181] utilizes FDTD method to model the realistic sintering experiments in multimode microwave cavities; [163] develops a simulation model for heating of the foods in microwave ovens; [182] proposes and tested simple semi-analytical models based on a piecewise constant approximation of the material properties; [183] develops a quasi-analytic model to examine the energy conversion during the microwave sintering. These literatures proposed macro models that coupled the microwave heating and thermal conduction. But none of them deals with the densification process in microwave sintering. This chapter focuses on how to integrate such a sintering behavior in simulation to form a complete coupling cycle of the microwave sintering. Based on a thermo-elasto-viscoplastic model proposed by Zhang and Gisik [140], the present work uses the previous work in research team done by Quinard, Song et al. Through studying the sintering behaviors of compacts formed by 316L stainless steel powders [46] and alumina powders [184] by means of dilatometer and conventional sintering furnace, a macro model was established to describe the shrinkage phenomena of thermal sintering process. Such a constitutive law is employed into the model of microwave sintering process in the present work. Numerical simulation has also been realized by using the finite element solver COMSOL Multiphysics (C) platform. It results in the 3D simulation for an example of microwave sintering in a single mode cavity. The coupling in simulation of microwave electric field, thermal conduction and sintering densification of the powder material is achieved.

6.2 Mathematical model of microwave sintering

The heating to materials by microwave is in fact dissipation of the energy for the electro-magnetic fields in propagation. Because of its nature, the sintered bodies are heated by the internal source produced by dissipation of the microwave energy. In order to establish the mathematical model for microwave sintering, there exist five main aspects to be solved:

1) Solve Maxwell equation to get electromagnetic fields in cavity of the furnace;
2) Solve for distribution of the heat generation in process of microwave sintering;
3) Solution of heat transfer equation to get temperature field in the sintered body;
4) Solve the governing equations of sintering densification to get the structural response of sintered body;
5) Coupling of the Maxwell equation, heat transfer equation and mechanic equations.

6.2.1 Solve Maxwell equation to get electromagnetic fields in cavity of the furnace

The governing equation of electro-magnetic problems in macroscopic scale is Maxwell equation. In the present studies, it involves the shaped components of non-ferromagnetic or ceramic powders. The heating effect of magnetic field in microwave is then very small compared to the effect of electric field [185]. So the effect of magnetic field is not taken into account in the present studies. Distribution of the electric field in cavity of the furnace can be achieved by the solution of Eq. 6-1 [185]:

$$\nabla \times \mu_{\mathrm{r}}^{-1}(\nabla \times E) - \omega^2 \varepsilon_r E = 0 \tag{6-1}$$

where μ_r is relative complex permeability， E is the strength of electric field， ω is angular frequency of the microwave source， ε_r is relative complex permittivity:

$$\varepsilon_r = \varepsilon_{\mathrm{r}}^{'} - i\varepsilon_r^{''} \tag{6-2}$$

where $\varepsilon_{\mathrm{r}}^{'}$ is dielectric constant; $\varepsilon_r^{''}$ is dielectric losses factor, which is an important parameter that determines the electric field. Inside the heating chamber, the volume is

divided into two parts: the one occupied by sintered compact and the rest space in vacuum, with different value of ε_r .

During sintering process, electromagnetic parameters, such as ε_r and μ_r etc., are the functions of temperature and density of the sintered powder. The exact variations of these parameters are unknown as the researches in their calibrations are still required. In simulations, the referred values of zirconia powder are taken from the literature [186] for approximation.

6.2.2 Solve for distribution of the heat generation in process of microwave sintering

The resistance heat for the material to generate in electromagnetic field, or the dissipated energy in microwave heating, can be determined by Eq. 6-3 [185]:

$$P = \frac{1}{2}[(\sigma_{EC} + \omega\varepsilon_r^{''})E^2 + \omega\mu_r^{''}H^2] \tag{6-3}$$

where E and H are electric and magnetic fields respectively. In the present studies, it involves the shaped components in ceramic powder. Then the second term in right hand side of equation (3) can be eliminated. σ_{EC} is electric conductivity， $\mu_r^{''}$ is magnetic loss factor (the imaginary part of relative complex permeability) of the sintered materials.

6.2.3 Solution of heat transfer equation to get temperature field in the sintered body

In principle of the microwave heating, the sintered body is regarded as dissipative medium for transmission of the microwave. The dissipation of microwave in medium is converted into heat. It increases the temperature in the heated body. In the heating process, the inhomogeneity of dissipated energy is resulted by inhomogeneous distribution of the electro-magnetic field. Then non uniform distribution of the temperature is resulted. The process of heat transfer in microwave heating can be simulated by solution of the heat

transfer equation (Fourier equation):

$$\rho C_{pp}\frac{\partial T}{\partial t}=k\nabla^2 T+P_h \tag{6-4}$$

where ρ is density of the materials， C_{pp} is its heat capacity， k is thermal conductivity， T is the temperature and P_h is heat source. The thermodynamic parameters such as C_{pp} and k depend on density of the material and its temperature. The measurements by specific experiments are required for their calibrations. The values referred from literatures are adopted in the present studies.

6.2.4 Solve the governing equations of sintering densification to get the structural response of sintered body

Green components of PIM materials after injection molding and debinding are consisted of the porous powders. The densification process during sintering is caused by grain growth and boundary diffusion of the grains. The evolution of relative density in sintered body during sintering process subjects to the mass conservation equation. It takes the form of Eq. 6-5:

$$\dot{\rho}+\rho\cdot tr(\dot{\boldsymbol{\varepsilon}})=0 \tag{6-5}$$

where ρ is density of the sintered material; $tr(\dot{\boldsymbol{\varepsilon}})$ is the trace of total strain rate. $\dot{\boldsymbol{\varepsilon}}$ is the tensor of total strain rate.

Under high sintering temperature conditions, macroscopic behavior of the material can be regarded as creep deformation [187-189]. An analogous viscoplastic constitutive law is adopted to describe densification behaviour of the powders. In addition, the effects of elasticity and thermal expansion are taken into account. The thermo-elasto-viscoplastic model [190] presented in Fig. 6-1 is used in the present study.

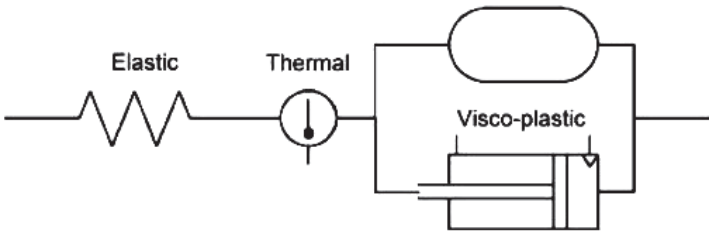

Fig. 6-1 The sintering model in present investigations

The tensor of total strain rate $\dot{\boldsymbol{\varepsilon}}$ is consisted of three parts: elastic strain rate $\dot{\boldsymbol{\varepsilon}}_{\mathrm{e}}$, thermal strain rate $\dot{\boldsymbol{\varepsilon}}_{\mathrm{th}}$ and viscoplastic strain rate $\dot{\boldsymbol{\varepsilon}}_{\mathrm{vp}}$.

$$\dot{\boldsymbol{\varepsilon}} = \dot{\boldsymbol{\varepsilon}}_{\mathrm{e}} + \dot{\boldsymbol{\varepsilon}}_{\mathrm{th}} + \dot{\boldsymbol{\varepsilon}}_{\mathrm{vp}} \tag{6-6}$$

The part of elastic strain rate is assumed to be linear and isotropic. It can be expressed in the following expression:

$$\dot{\varepsilon}_e = C_e \dot{\sigma} \tag{6-7}$$

where C_e is the elastic compliance matrix. Eq. 6-7 can also be expressed in the rate form of Hooke's law, as following:

$$\dot{\sigma} = D_e \dot{\varepsilon}_e = D_e \left(\dot{\varepsilon} - \dot{\varepsilon}_{\mathrm{th}} - \dot{\varepsilon}_{\mathrm{vp}} \right) \tag{6-8}$$

where D_e is elastic stiffness matrix.

The thermal strain is mainly due to thermal expansion that can be expressed as:

$$\dot{\varepsilon}_{\mathrm{th}} = \alpha \dot{T} I \tag{6-9}$$

where α is the thermal expansion coefficient, $\dot{T}$ is the temperature incremental rate, $\boldsymbol{I}$ is a second order identity tensor. α can be determined by the experiments carried out in dilatometer.

The viscoplastic strain rate $\dot{\boldsymbol{\varepsilon}}_{\mathrm{vp}}$ and related constitutive equation, which represents macroscopic response of the sintering process, is the key issue for sintering simulation. In present research, the phenomenological macroscopic mechanic model based on the principle of continuum mechanics is chosen to describe the densification behavior of the sintered material. The sintering body is regarded macroscopically as the compressible continuum even though it is composed of the solid and pores. The linear viscoplastic constitutive law is the most widely used one in the macroscopic models for sintering [114, 191, 192]. It can be expressed as Eq. 6-10:

$$\dot{\varepsilon}_{vp} = \frac{\sigma'}{2G_p} + \frac{tr\sigma_t - 3\sigma_s}{9K_p} I \tag{6-10}$$

where σ_t is the stress tensor in sintered materials，σ' is the deviatoric stress tensor，$tr\sigma$ is trace of the stress tensor，σ_s represents the sintering stress，I is second order identity tensor. G_P and K_P are the shear and bulk viscosity modulus of the porous material, respectively.

Various models have been developed to determine G_p, K_p and σ_s in the constitutive law. Generally they fall into three types that include the phenomenological, microstructural and experimental ones. The elastic-viscous analogy is chosen to define the shear and bulk viscosity modules for sintering materials, as related in equation [188]:

$$G_p = \frac{\eta_z}{2(1+\nu_{vp})}$$
$$K_p = \frac{\eta_z}{3(1-2\nu_{vp})} \tag{6-11}$$

where η_z and ν_{vp} are uniaxial viscosity and viscous Poisson's ratio of the porous material. From Eq. 6-11, it is known that G_P and K_P can be determined by experiments by means of the calibration of uniaxial viscosity and viscous Poisson's ratio. Song et al. have defined the following relationship to define the uniaxial viscosity η_z by bending tests [14, 155, 169], as shown in Fig. 6-2 and Eq. 6-12.

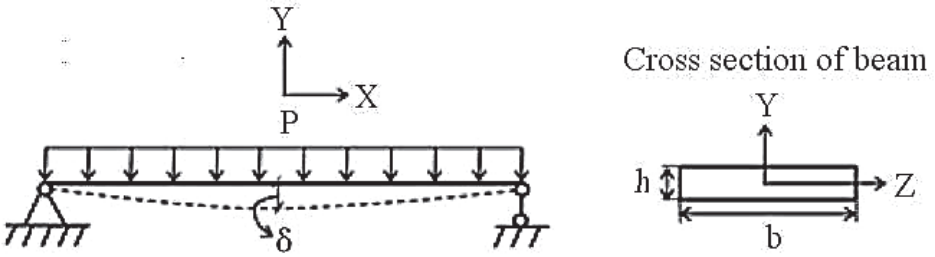

Fig. 6-2 Simply supported beam model for beam-bending tests

$$\eta_z = \frac{1}{\dot{\delta}}\left(\frac{5\rho_a g L_s^4}{32h^2} + \frac{PL_s^3}{4bh^3}\right) \tag{6-12}$$

where $\dot{\delta}$ is the deflection rate at center of the specimen, ρ_a is the apparent density, g is

gravitational acceleration, P is the external load, L_s is the distance between the two supporting rods. b and h are width and thickness of the specimen.

The viscous Poisson's ratio is determined from an average relationship in the following form [188]:

$$\nu_{vp} \approx \frac{1}{2}\sqrt{\frac{\rho}{3-2\rho}} \tag{6-13}$$

where ρ is the relative density.

Sintering stress σ_s should be calibrated experimentally by different heating processes. Sintering stress σ_s is the function of apparent density ρ, surface energy and particle sizes. Its calibration is realized by sintering of small specimens in dilatometer [14, 155]. In simulation for the process of microwave sintering, it is the function of density and temperature. The following equation is proposed to determine the sintering stress [193]:

$$\sigma_s = B\rho^C \tag{6-14}$$

where B and C are the material parameters that should be identified from dilatometer experiments.

The above evaluation is summarized in Fig. 6-3.

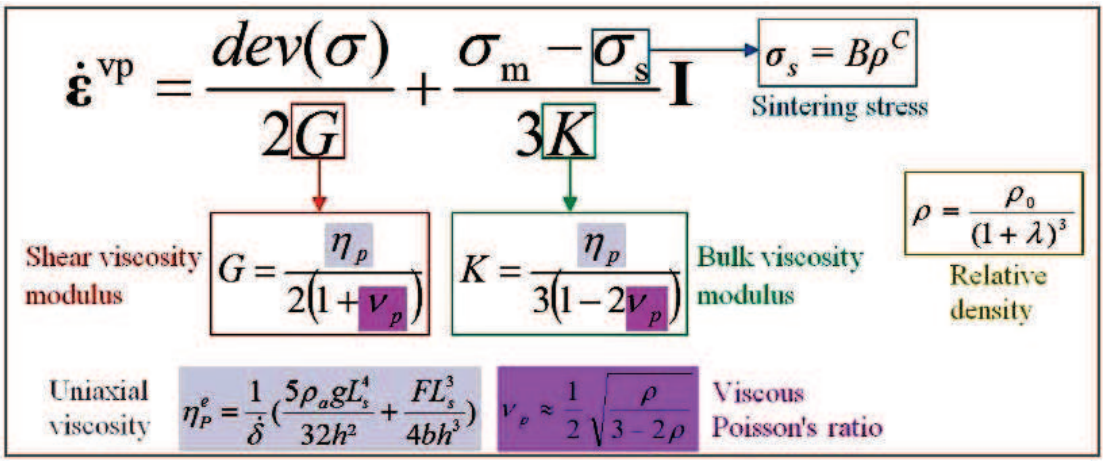

Fig. 6-3 Evaluation of the viscoplastic strain rate in the sintering model (λ is the uniaxial shrinkage, measured by the tests in dilatometer)

To realize the simulation, the coefficient of thermal dilatation α for sintered material, as well as the material parameters related to elastic deformation, are required, too. These parameters are expressed illustratively by:

$$\alpha = \alpha(\rho, T), \quad E_{\mathrm{e}} = E_e(\rho, T) \tag{6-15}$$

where E_{e} is the elastic modulus of porous material.

6.2.5 Coupling of the Maxwell equation, heat transfer equation and mechanic equations

The process of microwave sintering includes three types of the physics. One is the transmission of microwave energy in the heating cavity. A part of the microwave energy is converted into heat energy, because of its dissipation during the transmission. The second one is the process of heat transfer. Because of inhomogeneous distribution of the electric field in the heating cavity, it generates the heat not homogeneously in the sintered material, too. Then there exists the process of heat transfer. The third one is the process of densification during sintering. The particles and grains of PIM material connect and fuse together. The pores among the particles reduce and disappear gradually. Macroscopically it appears to be the shrinkage of sintered products. The volume is reduced while the density increases. The evolution of density and temperature during sintering results in the variation of different parameters in physical equations. It results then the complicated coupling of different physics.

6.3 Numerical simulation of microwave sintering process

6.3.1 Modeling of Microwave Sintering

Microwave sintering is the process of microwave heating to realize the sintering densification. It involves the solution of steady state equations for frequency domain analysis of electro-magnetic fields and the distribution of generated heat. The distribution of

temperature in sintered body is obtained by transient simulation of the heat transfer. Evolution of the density and shrinkage of PIM material is achieved by mechanical simulation of the sintering process.

The incremental algorithm is applied for integration in time of the mathematic model, in which the processes of microwave sintering on PIM materials are described. The governing equations for three types of the physics mentioned above are solved by the fractional steps. In each time step, distribution of the electric field at this instant is solved by the direct methods, while temperature field and evolution of the densification should be solved iteratively. The coupling among three different physics is realized by increment of the time steps. In the process of solution, the dissipated energy is introduced into the equation of heat transfer (Eq. 6-4) as internal heating source. Then distribution of the temperature field is solved. The temperature field is further introduced into the solution of constitutive equation and densification equation. Their solution provides then the evolution of densification and shape deformation during sintering of the PIM material.

Due to the variation of electromagnetic and thermal parameters according to density of the material and temperature, the field variables are solved with the updated parameters in the incremental solutions. The cyclic increments run forward until the prescribed sintering process is finished. So the simulation process of microwave sintering is the cyclic solutions of Maxwell equation, heat transfer equation, as well as the structural equilibrium equation, material densification equation and constitutive equation, as show in Fig. 6-4.

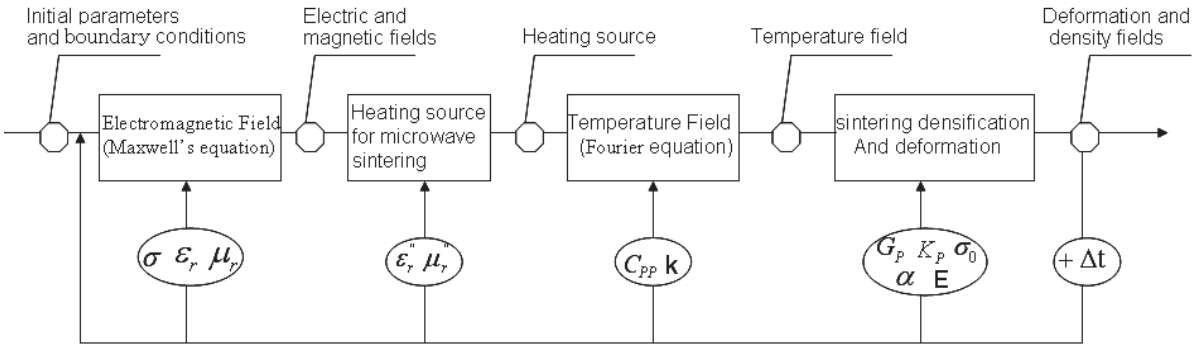

Fig. 6-4 The coupling of multi-physics in simulation of the microwave sintering

The cavity of microwave furnace can be regarded as a metallic box. A microwave

source of 2.45 GHz is connected with continuously adjustable output power. As the magnetic effect is ignored in the present studies, the microwave source is set to be the transvers electric (TE) wave. Wall surfaces of the furnace and waveguide are regarded as the perfect electric conductor, represented by the boundary condition $\mathbf{n} \times \mathbf{E} = 0$. Because of the symmetry, half of the model is analyzed. Due to mirror symmetry of the electric field, the plan of symmetry can be regarded as a perfect magnetic conductor, represented by the boundary condition $\mathbf{n} \times \mathbf{H} = 0$.

The shaped body in submicron ceramic powder is taken in simulation. Its physical parameters are shown in Table 6-1. The referred values of zirconia powder in literature [186] are taken for approximation. It should be mentioned that the experimental measurements for these parameters are still less available. The related physical parameters, such as relative permittivity, conductivity etc, as well as the ones in analogous viscoplastic constitutive law for sintering, are still the current researches in material science. Their values retrieved from literatures represent large differences, too. However, the true material parameters represent prime importance for accurate simulation of the microwave sintering process. The present paper focuses on the modeling and simulation method for densification process of the microwave sintering. The really reliable parameters of sintered materials in microwave sintering should be achieved by the experimental ways in the further works.

Table 6-1 physical parameters of CIM component based on zirconia powder [186]

Electromagnetic parameters：
Air in the cavity： $\mu_{r\_air} = \varepsilon_{r\_air} = 1$;
Sintered compact: $\varepsilon_r = 10 - i0.1e^{0.0017(T-293)}$， $\mu_r = 1$；
Input power of microwave source：1 KW
Heat transfer parameters：
Conductivity：k=30 ρ_r W/(mk)； Density： $\rho = 6000\rho_r\ kg/m^3$；
Heat capacity： C_{pp}=900ρ_r $J/(kgK)$；
Initial temperature： $T_0 = 293k$ (ρ_r is relative density)
Densification process:
Thermal expansion coefficient: α=1.2×10^{-2}/k; Poisson's ratio: ν=0.33 ;
Shear viscosity modulus: G_P =1 × 10^{11} Pa; Bulk viscosity modulus K_P =1 × 10^{11} Pa;
Initial relative density： $\rho_{r0} = 0.65$.
Note: Some of the above parameters are the initial ones. For the ones with unknown variation, constant values are taken in the present simulation.

6.3.2 Numerical analysis

The finite element package COMSOL Multiphysics (C) is employed in the research on simulation of microwave sintering process. In order to determine the suitable position of sintered compact in cavity of the microwave furnace, the distribution of electric field in an empty cavity is first analyzed. The result is shown in Fig. 6-5.

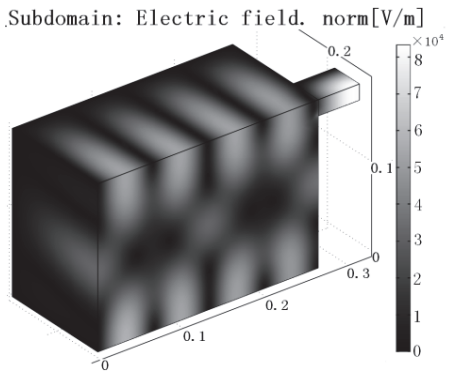

Fig. 6-5 Distribution of electric field in empty cavity

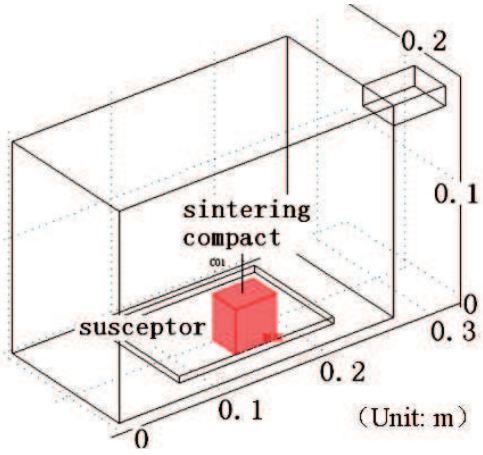

Fig. 6-6 Placement of sintered compact

It provides the suitable placement of sintered body by investigation on distribution of the electric field in cavity of the microwave furnace. As shown in Fig. 6-6, the sintered compact should be placed to the position of peak electric field. Then the sintered material absorbs as much as possible the energy of electric waves. Geometric dimensions and meshes are shown in Fig. 6-7 and Fig. 6-8 respectively. 3D tetrahedron lagrange element has been set as the element type. The total model includes 753 nodes, 3514 elements.

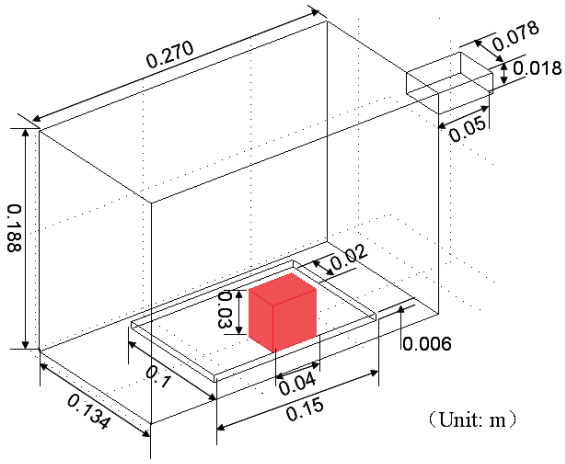

Fig. 6-7 Geometric dimensions

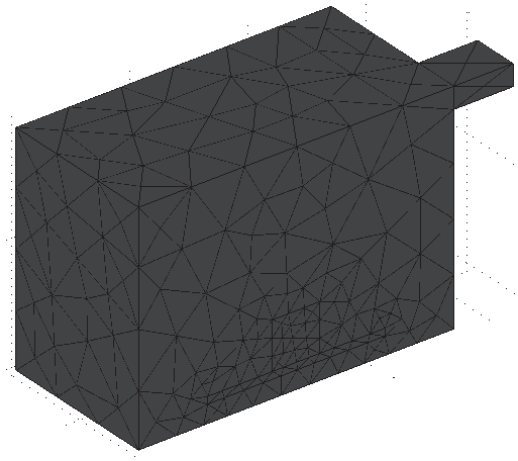

Fig.6-8 3D Meshes in COMSOL

To simplify the model, it is assumed that the outer surface of sintered compact is adiabatic with the environment in furnace chamber. When the solutions on evolution of heat transfer, structural response of strain-stress and relative density are realized, it takes into account only the region of sintered compact. The calculations for these effects are then suppressed in void volume of cavity.

The temperature field on a cross section inside the CIM material, after heating 1500 seconds, is shown in Fig. 6-9. The peak value of temperature reaches to about 1650 ^{o}K near center of the sintered compact. The temperature gradient is moderate in the compact. The displacement along x direction is shown in Fig. 6-10. The magnitude of displacement at same time is shown in Fig. 6-11. The obvious shrinkage towards center and bottom of the compact can be observed, which represents the effect of densification, too. The final relative density field can be seen in Fig. 6-12.

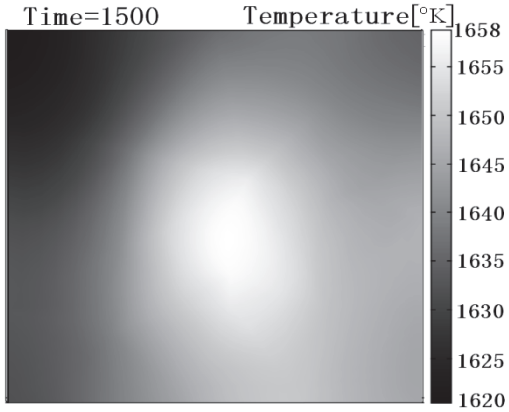

Fig. 6-9 Temperature field at 1500s

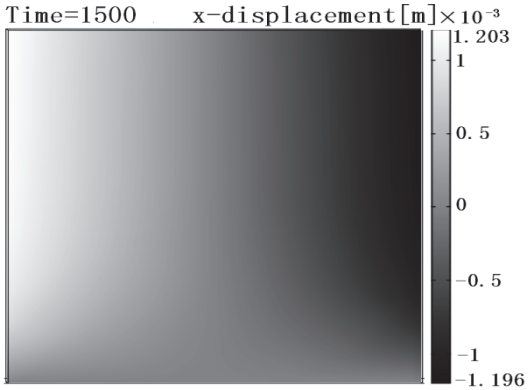

Fig. 6-10 Displacement along x-direction

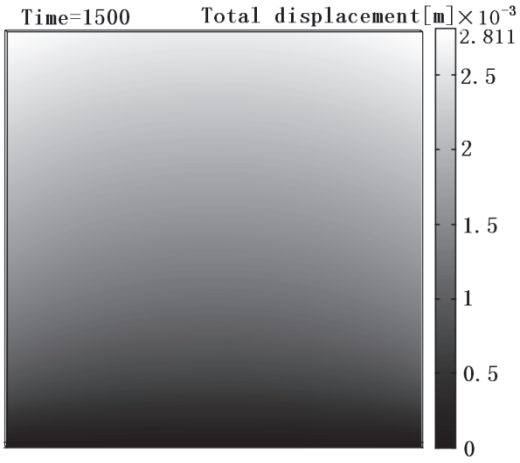

Fig. 6-11 Total displacement in cross section

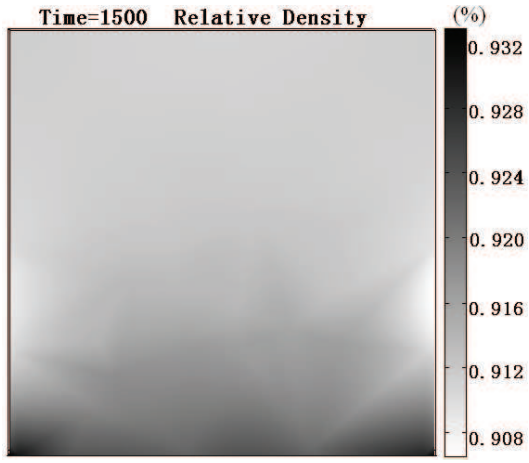

Fig. 6-12 Final relative density

The solutions are realized by non-linear solver of the package COMSOL. It lasts 1500 seconds (25 minutes) for the whole process of microwave sintering. The results at 6 instants are kept in simulation process for the further investigation. The 6 instants are chosen by equal intervals for the whole process in 1500 seconds.

As relative permittivity of the material is a function of temperature, dielectric loss factor increases with the increase of temperature. So generation of resistance heat in the material is

very small in initial stage of the microwave heating. It heats slowly. In the first 10 minutes, there is no obvious variation for temperature and relative density in the material. After 10 minutes, temperature increases with the strong increasing rate in the CIM material to reach the peak value. The relative density increases continuously with the increase of temperature, too. At last, it gets close to the fully densified material (The relative density is increasing over 0.9). The discussed variations can be observed in Fig. 6-13 and Fig. 6-14. As the power of microwave source is set to be a constant value 1kw, the temperature in material increases continuously. By regulation of the input powder of microwave source, the sintering process can be controlled to get into the holding stage, and then the cooling stage. For evaluating the simulation result, experiment results from Charmond et al. [167] can be used to make a comparison. Specimens made by spray-dried 2 mol% yttria-doped zirconia nanopowder have been investigated in [167]. It concludes that the sintered material shows poor coupling with the microwaves below 673 ^{o}K, and then the coupling effects become stronger and stronger when the temperature is over 673 ^{o}K. This experiment phenomenon meets well with the simulation result. With the same maximal sintering temperature at about 1633 ^{o}K, the corresponding final relative density of conventional sintering, microwave sintering and simulation result can be seen in Fig. 6-15. We can see that result of simulation is a little lower than the experimental one, because the sintering model for present simulation is not a precisely calibrated one. For some parameters with unknown variation, constant values are taken in the present simulation. So the evolution of relative density represents only the referential values.

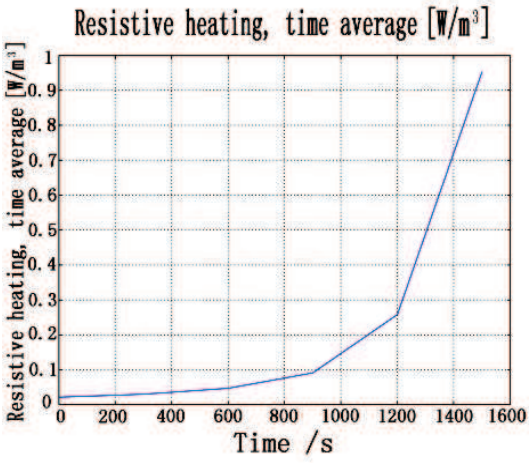

Fig. 6-13 Evolution of heat generation

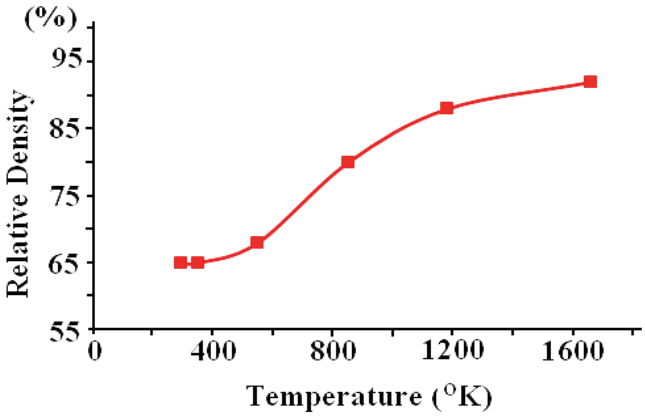

Fig. 6-14 Evolution of relative density versus sintering temperature during microwave sintering process

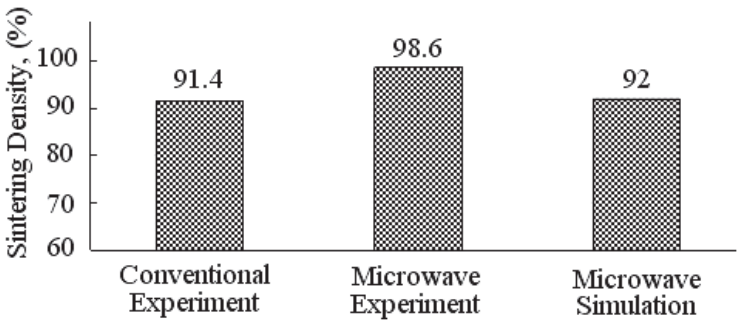

Fig. 6-15 Comparison between the experimental and the numerical relative density, the experiment results are taken reference from the work of Charmond et al. [167].

6.4 Conclusion and outlook

The process of microwave sintering includes the phenomena of electromagnetism, heat transfer and sintering densification, as well as their couplings. By analysis on the principles of microwave sintering, the mathematic model is established. The governing equations to describe three main physical phenomena are provided. Coupling relationships among the main governing equations are discussed. The parameters in equations are analysed to identify their dependence on the other factors. Discussion is made on the methods to determine their values. The specific configuration of microwave furnace is taken into account in the simulation. The RF module, heat transfer module, structure analysis module in

COMSOL package is employed. The constitutive law, which describes sintering densification of CIM materials under high temperature, is implemented into the structure analysis. The coupling of multi-phasics in microwave sintering is realized in simulation. Results of simulation are analysed. The work focuses on modelling of the microwave sintering and the methods for its simulation. It provides an effective way for the further analysis and the achievement of knowledge on microwave sintering. For more accurate simulations, the true parameters and constitutive law of CIM materials are required. Besides that, the external effect, such as boundary conditions, gravitation and friction, should be taken into account. It represents the great importance to study and achieve theses parameters and relationships by experiments.

Chapter 7 Conclusions and Perspectives

7.1 Conclusions

The research reported in this thesis represents two main aspects for investigation of the PIM technologies. One is the enhancement and improvement to the actual tools for simulation of the micro filling process. The other focuses on the experiment and simulation research of microwave sintering. Due to rarely reported, components based on 17-4PH stainless steel powder are introduced in the experiment of microwave sintering. The favorable results and regular gradient in sintered body are obtained and revealed, compared to the only report of unfavorable conclusion. The simulation of microwave sintering, from distribution of the electromagnetic fields to the densification of sintered bodies, is developed with the coupling of multi-physics. It represents the first attempt to couple the microwave heating and the behaviors of powder densification in simulation in our labs. The main contributions in present thesis are detailed below:

1) For the enhancement of filling simulation, the present study in section 2.2 and section 2.3 completed and modified the actual algorithms for simulation of the injection filling process. In section 2.2, a modification on solution of the filling front evolution is proposed and realized to improve the wrongly directed filling patterns in actual commercial software and the code in research team. A modified algorithm, which is similar to upwind method, is proposed in Section 2.2. It employs a systematic operation to modify the fluid velocity field. Then the advection of filling state is made to be more affected by the real filling flow behind the filling front. For validation of the new proposed method, the results obtained by commercial software MPI software (Autodesk$^{(C)}$) and the filling patterns obtained by experimental results from G. Larsen [66] are introduced to make a comparative analysis. It shows that this similar upwind method is valid to improve the wrongly directed filling patterns. In section 2.3, a completion of the outlet boundary condition is added in FEM code to overcome the delay of fully filling in the last filling stage. The filling ratio of incompressible flow should be a linear one with respect to time when constant velocity is imposed on inlet. But the linearity is not respected when the filling front approaches to the

outlet boundary. To remedy this defect, the modeling is formulated again. An integration term on the outlet boundary is realized in solution of the advection equation for filling state. Then the incompressibility and linearity of the filling flow can hence be well respected at the last filling stage. The results from these two modified algorithms for the simulations of mold filling process are conformed to be optimized and more reliable. The stability for solution of the filling state is improved.

2) In Chapter 3, for the lack of appropriated FEM method to take into account the surface tension effect in micro injection, a specific method is proposed and implemented. This work represents the significant importance for the analysis of capillarity dominant free surface flows in micro-injection molding. It affords the practical way for evaluation of the surface tension effects in viscous filling flow. However, when dealing with the determination of front curvature, it contains a second order derivative function, in the form of a Laplacian operator. Because the filling function is a scalar one while the velocity function is a vector one, the integration of filling function in second derivative is not suitable be transformed into the boundary integration and the integration of function in lower order derivative. So a new method is proposed to evaluate the curvature of filling front by the simple and systematical procedures. It settles down successfully the problem for calculation of the front curvature (Eq. 3-1). By comparing the magnitudes of surface tension force with the viscous force for a filling example in micro channels, it indicates that the effect of surface tension does not represent the significant effect in ordinary injection molding, but shows the importance for the micro injection molding of sub-millimeter sizes. All the works for micro injection molding have been programmed in the C++ environment and planted into the previous in-house solver on the platform of Matlab (C) version 7.10. The functionality of in-house solver has been extended and become more powerful.

3) Chapter 5 is about the experiments and some new discoveries for microwave sintering. For compacts based on 17-4PH stainless steel powder, only one investigation [175] on the MW processing is found by the retrieves of literatures in the currently available resources. It provided a conclusion that MW sintering has not improved the mechanical properties compared to CRH sintering for 17-4PH stainless steel. But the results in Chapter 5 of present thesis support a different conclusion. The authors conform that the MW sintering

process for 17-4PH stainless steel can not only shorten greatly the sintering time, lower the peak sintering temperature, but also it provides higher sintered density and fewer defects in micro structure. Higher Vickers-hardness of MW sintered compacts is also detected in the present work. By a series of the experiments, the optimal microwave sintering process for specimens based on 17-4PH stainless steel is determined. The optimal process is heating directly from ambient temperature to 1150℃ with heating rate 30℃/min, and then held 10 minutes. It will get the specimen with higher density (relative density: 96.6%) and better mechanical properties (Vikers-hardness: 316V). Moreover, because of its rapid heating in the internal volumetric way, sintering by Microwave heating resulted in the obvious gradient in mechanic properties of the sintered material. It is due to the nature of microwave heating. In the present thesis, none of the specimens presents visually observable distortion. The prediction, evaluation and purposes of the gradient properties induced by microwave leads the studies to the more precise and profound insights.

4) The mathematic model to describe Multi-physics phenomena of microwave sintering process is established in Chapter 6. It includes the coupling of electro-magnetic fields, thermal conduction and the densification process of sintered powders. Most of the actual literatures propose macro models that coupled the microwave heating and thermal conduction, but none of them deals with the densification process in microwave sintering. The present thesis represents the first attempt to model the whole sintering process by microwave heating. The simulation of densification is based on a thermo-elasto-viscoplastic model [140]. It is employed into the modelling of whole microwave sintering process. Using the finite element solver COMSOL Multi-physics, the coupling of microwave electric field, thermal conduction and sintering densification of the powder material is realized for a 3D example of microwave sintering in a single mode cavity. It provides an effective way for the further analysis and the achievement of knowledge on microwave sintering.

7.2 Future Work

The presented enhancement and improvement for simulation of micro-injection molding process, and the mathematical models for modeling the process of microwave sintering have

proven their effectiveness in prediction of the final results. However, the works are far away to be finished. There are still the important problems to be solved. Some of the works in the near future can be suggested as below:

- Reinforce the research on micro-injection molding in both experiment and simulation aspect. Evaluate each of the influence factors, such as surface tension, wall slip, viscous dissipation and convective heat transfer to the filling flow in micro cavities. Extend the simulation of μ-injection to nano-injection with a lot of knowledge on the new physical and mathematical models.
- For microwave sintering experiment, the obvious gradient in mechanic properties is found inside the sintered material. It is due to the rapid generation of heat by microwave heating inside the sintered material. It is valuable to continue the studies on this effect for the application of microwave sintered products. The modeling and simulation on generation of the gradient properties represent also the significant insights for the further studies. More physical experiments should be conducted to know the mechanical properties. The simulation models for predicting the mechanical properties can be built based on the experimental investigations.
- For simulations of the microwave sintering process, it is actually a preliminary attempt. There are many imperfect aspects. Chapter 6 focuses on the modeling and simulation method for densification process of the microwave sintering. The related physical parameters, such as relative permittivity, conductivity etc., as well as the ones in analogous viscoplastic constitutive law for sintering, are not the really reliable parameters of sintered materials. However, the true material parameters represent prime importance for accurate simulation of the microwave sintering process. They should be achieved by the new technologic and scientific development to have a specially instrumented microwave furnace with a lot of scientific equipment (infrared camera, pyrometers, optical measurements etc).
- The sintering experiments in microwave oven for different kinds of feedstock and the same one with various powder loadings should be carried out in future.
- Combination of the simulation for injection filling stage and microwave sintering stage is favorable for optimization of the entire PIM process. In order to simulate the sintering

process under real conditions, the parameters such as the frictional coefficient, thermal conductivity and heat capacity of the porous materials should be determined.

- The mechanical properties of the sintered components are dependent on its microstructures. Besides the macroscopic models, the microscopic or mesoscopic models for sintering should also be developed. With the multi-scale modeling, the dimensional changes and the microstructural evolutions of the sintering components can be predicted simultaneously.

Acknowledgment

I would like to express my sincere gratitude to my thesis supervisor, Prof. Baosheng LIU (Southwest Jiaotong University, China) and Prof. Jean-Claude GELIN (ENSMM, France), for their support, guidance and encouragement during the whole research course. Their advanced knowledge and rich experiences in the field of forming manufacturing and numerical simulation are the assurance for performing this thesis. I am also grateful to my co-supervisor, Prof. Zhiqiang CHENG (Southwest Jiaotong University, China) and Prof. Thierry BARRIERE (Université de Franche-Comté, France). Thanks for their working enthusiasm and constructive opinions.

I would like to thank Université de Franche-Comté, Femto-ST institution for their invitation and acceptance, which give me a chance to pursue my study abroad. And also thanks to China Scholarship Council for awarding me a scholarship to stay in France.

Special thanks to engineers in Femto-ST institution, Mohamed Sahli, Gérard Michel, Christine Millot and Vincent Placet, for their support in the experiments. I particularly express my thankful to my friend Gang Cheng, who did me a great favor in work and daily life when I was staying in France.

I wish to thank my colleagues and teammates：Edouard Falconnet, Belgacem Mamen, Gang Cheng, Jie Zhang, Huibin Ou in Femto-ST institute and Huiliang Luo, Yanyu Wang, Hangzhuo Yu, Fengshun Gao, Xiangqiang Wei, Jie Chen, Lngyu Yang, Yanxin Liu and Ming Li in Southwest Jiaotong University.

Finally, I wish to thank my grandma and my parents for providing me a lovely environment and continuous support all through these years. I especially thank my girlfriend Xuanyu, Yan for her fully support, encouragement and company. Je suis très heureux, Je t'aime.

References

[1] GERMAN R M. Powder Injection Molding [M]. Princeton: NJ, 1990.

[2] SAHLI M, MILLOT C, GELIN J C, et al. The manufacturing and replication of microfluidic mould inserts by the hot embossing process [J]. Journal of Materials Processing Technology, 2013, 213(6): 913-25.

[3] SUPATI R, LOH N H, KHOR K A, et al. Mixing and characterization of feedstock for powder injection molding [J]. Materials Letters, 2000, 46(2–3): 109-14.

[4] LIU Z Y, LOH N H, TOR S B, et al. Characterization of powder injection molding feedstock [J]. Materials Characterization, 2002, 49(4): 313-20.

[5] AHN S, PARK S J, LEE S, et al. Effect of powders and binders on material properties and molding parameters in iron and stainless steel powder injection molding process [J]. Powder Technology, 2009, 193(2): 162-9.

[6] KONG X, BARRIERE T, GELIN J C. Determination of critical and optimal powder loadings for 316L fine stainless steel feedstocks for micro-powder injection molding [J]. Journal of Materials Processing Technology, 2012, 212(11): 2173-82.

[7] MENG J, LOH N H, FU G, et al. Micro powder injection moulding of alumina micro-channel part [J]. Journal of the European Ceramic Society, 2011, 31(6): 1049-56.

[8] YE H, LIU X Y, HONG H. Fabrication of metal matrix composites by metal injection molding—A review [J]. Journal of Materials Processing Technology, 2008, 200(1–3): 12-24.

[9] GERMAN R M, BOSE A. Injection Molding of Metals and Ceramics [M]. Princeton, New Jersey, USA, 1997.

[10] GERMAN R M. Strength evolution during thermal debinding of injection moulded parts: (Pennsylvania State University, USA.) [J]. Metal Powder Report, 2000, 55(9): 39.

[11] ENNETI R K, SHIVASHANKAR T S, PARK S-J, et al. Master debinding curves for solvent extraction of binders in powder injection molding [J]. Powder Technology, 2012, 228(0): 14-7.

[12] TRUNEC M, CIHL Ř J. Thermal debinding of injection moulded ceramics [J]. Journal of the European Ceramic Society, 1997, 17(2–3): 203-9.

[13] WEINAND D, BLOEMACHER M. MIM feedstock for rapid catalytic debinding : (BASF AG, Ludwigshafen, Germany) [J]. Metal Powder Report, 1994, 49(1): 39.

[14] SONG J. Experiments, Modelling and Numerical Simulation of the Sintering Process for Metallic or Ceramic Powders [D]; University of Franche-Comté and Southwest Jiaotong University, 2007.

[15] http://www.amt-mat.com/Powder_Injection_Molding_PIM_Comparison.html.

[16] MERHAR J R. Overview of metal injection moulding [J]. Metal Powder Report, 1990, 45(5): 339-42.

[17] STEVENSON J F. Powder Metal Injection Molding [M]//MUSA R K, AVRAM L I, SHIH-JUNG LIUA2 - MUSA R. KAMAL A L I, et al. Injection Molding. Hanser. 2009: 309-40.

[18] GERMAN R M. Research productivity and the value to the P.I.M. market [M]//GERMAN R M. PIM 2000, Int Conference on Injection Moulding of Metals and Ceramics. Penn States University Press. 2000.

[19] GERMAN R M. Status of PIM Research and Development [M]//M.P.I.F. PIM 2007, Int Conference on Injection Moulding of Metals and Ceramics. 2007.

[20] GERMAN R M. Powder Injection molding: Statistical trends and forward forcasts for the industry [J]. PIM International, 2013, 7(1): No.1.

[21] KONG X J. Development and Characterization of Polymermetallic Powder Feedstocks for Micro-injection Molding [D]; L'Université de Franche-Comté, 2011.

[22] Metal and Ceramic Injection Moulding (AVM049B) from BCC Research, http://www.bccresearch.com/pressroom/report/code/AVM049B, retrieved 10/31/12. [M].

[23] MACNEAL T. Growth prospects brightening for global MIM market [J]. Metal Powder Report, 2013, 68(1): 14-5.

[24] GERMAN R M. Sintering theory and practice [M]//WILEY J, SONS. 1996.

[25] GERMAN R M. Design and applications [M]. Innovation Material Solutions, 2000.

[26] EDIRISINGHE M J. Injection Molding [M]//EDITORS-IN-CHIEF: K H J B, ROBERT W C, MERTON C F, et al. Encyclopedia of Materials: Science and Technology (Second Edition). Oxford; Elsevier. 2001: 4088-94.

[27] GUNDUZ O, AHMAD Z, STRIDE E, et al. A device for the fabrication of multifunctional particles from microbubble suspensions [J]. Materials Science and Engineering: C, 2012, 32(4): 1005-10.

[28] SHAW H M, EDIRISINGHE M J. Porosity development during removal of organic vehicle from ceramic injection mouldings [J]. Journal of the European Ceramic Society, 1994, 13(2): 135-42.

[29] SHAW H M, EDIRISINGHE M J. Shrinkage and particle packing during removal of organic vehicle from ceramic injection mouldings [J]. Journal of the European Ceramic Society, 1995, 15(2): 109-16.

[30] ALCOCK J. Co-injection promises further growth for MIM [J]. Metal Powder Report, 1999, 54(6): 30-4.

[31] KOWALSKI L, DUSZCZYK J, KATGERMAN L. Thermal conductivity of metal powder-polymer feedstock for powder injection moulding [J]. Journal of Materials Science, 1999, 34(1): 1-5.

[32] TURKER M, GODLINSKI D, PETZOLDT F. Effect of production parameters on the properties of IN 718 superalloy by three-dimensional printing [J]. Materials Characterization, 2008, 59(12): 1728-35.

[33] RADOCAJ A, WEISS T, HELSBY W I, et al. Force-Generating Cross-Bridges during Ramp-Shaped Releases: Evidence for a New Structural State [J]. Biophysical Journal, 2009, 96(4): 1430-46.

[34] PIOTTER V, FINNAH G, HANEMANN T, et al. Micro Injection Molding [M]//MUSA R K, AVRAM L I, SHIH-JUNG LIUA2 - MUSA R. KAMAL A L I, et al. Injection Molding. Hanser. 2009: 341-93.

[35] ZEEP B, NORAJITRA P, PIOTTER V, et al. Net shaping of tungsten components by micro powder injection moulding [J]. Fusion Engineering and Design, 2007, 82(15–24): 2660-5.

[36] BIDAUX J E, JOCHEM A. Powder injection moulding of NiTi shape memory materials [J]. Powder Injection Moulding International, 2008, 2(1): 59-62.

[37] NYBORG L. Interactions between surface-active additives and 316L stainless steel powder for MIM: (Chalmers University of Technology, Sweden.) [J]. Metal Powder Report, 1998, 53(4): 38.

[38] LEVENFELD B, V REZ A, CASTRO L, et al. Processing of P/M M2 high speed steels by mould casting using thermosetting binders [J]. Journal of Materials Processing Technology, 2001, 119(1–3): 1-6.

[39] MATOS M, CASTANHO J M, VIEIRA M T. Composite copper/stainless steel coated powders [J]. Journal of Alloys and Compounds, 2009, 483(1–2): 460-3.

[40] LIU Z Y, LOH N H, TOR S B, et al. Micro-powder injection molding [J]. Journal of Materials Processing Technology, 2002, 127(2): 165-8.

[41] YAMAMOTO O, SASAMOTO T, INAGAKI M. Antioxidation of carbon-carbon composites by SiC concentration gradient and zircon overcoating [J]. Carbon, 1995, 33(4): 359-65.

[42] KANG Y, KANG S. The surface microstructure of TiC-(Ti,W)C-WC-Ni cermets sintered in a nitrogen atmosphere [J]. Materials Science and Engineering: A, 2010, 527(27–28): 7241-6.

[43] KANG Y, KANG S. WC-reinforced (Ti,W)(CN) [J]. Journal of the European Ceramic Society, 2010, 30(3): 793-8.

[44] DUTILLY M, GHOUATI O, GELIN J C. Finite-element analysis of the debinding and densification phenomena in the process of metal injection molding [J]. Journal of Materials Processing Technology, 1998, 83(1–3): 170-5.

[45] GELIN J C, BARRIERE T, DUTILLY M. Experiments and Computational Modeling of Metal Injection Molding for Forming Small Parts [J]. CIRP Annals - Manufacturing Technology, 1999, 48(1): 179-82.

[46] QUINARD C, SONG J, BARRIERE T, et al. Elaboration of PIM feedstocks with 316L fine stainless steel powders for the processing of micro-components [J]. Powder Technology, 2011, 208(2): 383-9.
[47] BARRIERE T, GELIN J C, LIU B. Experimental and numerical investigations on properties and quality of parts produced by MIM [J]. Powder Metallurgy, 2001, 44(3): 228-34.
[48] SONG J, GELIN J C, BARRIERE T, et al. Experiments and numerical modelling of solid state sintering for 316L stainless steel components [J]. Journal of Materials Processing Technology, 2006, 177(1–3): 352-5.
[49] SPENCER R S, GILMORE G D. Some flow phenomena in the injection molding of polystyrene [J]. Journal of Colloid Science, 1951, 6(2): 118-32.
[50] BALIMAN R L, SHUSMAN T, TOOR H L. Injection Molding - Flow of a Molten Polymer into a Cold Cavity [J]. Industrial & Engineering Chemistry, 1959, 51(7): 847-50.
[51] KUO Y, KAMAL M R. The fluid mechanics and heat transfer of injection mold filling of thermoplastic materials [J]. AIChE Journal, 1976, 22(4): 661-9.
[52] RYAN M E, CHUNG T S. Conformal mapping analysis of infection mold filling [J]. Polymer Engineering & Science, 1980, 20(9): 642-51.
[53] HIEBER C A, SHEN S F. A finite-element/finite-difference simulation of the injection-molding filling process [J]. Journal of Non-Newtonian Fluid Mechanics, 1980, 7(1): 1-32.
[54] HIEBER C A, SOCHA L S, SHEN S F, et al. Filling thin cavities of variable gap thickness: A numerical and experimental investigation [J]. Polymer Engineering & Science, 1983, 23(1): 20-6.
[55] MAVRIDIS H, HRYMAK A N, VLACHOPOULOS J. Finite element simulation of fountain flow in injection molding [J]. Polymer Engineering & Science, 1986, 26(7): 449-54.
[56] SATO T, RICHARDSON S M. Numerical simulation of the fountain flow problem for viscoelastic fluids [J]. Polymer Engineering & Science, 1995, 35(10): 805-12.
[57] LIN M, THOMAS HAHN H, HUH H. A finite element simulation of resin transfer molding based on partial nodal saturation and implicit time integration [J]. Composites Part A: Applied Science and Manufacturing, 1998, 29(5–6): 541-50.
[58] SOLTANI B, MATTIASSON K, SAMUELSSON A. Implicit and dynamic explicit solutions of blade forging using the finite element method [J]. Journal of Materials Processing Technology, 1994, 45(1–4): 69-74.
[59] SWAMINATHAN C R, VOLLER V R. A time-implicit filling algorithm [J]. Applied Mathematical Modelling, 1994, 18(2): 101-8.
[60] DHATT G, GAO D M, CHEIKH A B. A finite element simulation of metal flow in moulds [J]. International Journal for Numerical Methods in Engineering, 1990, 30(4): 821-31.
[61] LEWIS R W, USMANI A S, CROSS J T. Efficient mould filling simulation in castings by an explicit finite element method [J]. International Journal for Numerical Methods in Fluids, 1995, 20(6): 493-506.
[62] BARRIERE T, LIU B, GELIN J C. Determination of the optimal process parameters in metal injection molding from experiments and numerical modeling [J]. Journal of Materials Processing Technology, 2003, 143–144(0): 636-44.
[63] LIU B S, BARRIERE T, GELIN J C. A new explicit algorithm for bi-phasic mixture flow in MIM [J]. Journal of Southwest Jiaotong University, 2002, 10(2): 152-60.
[64] CHENG Z, BARRIERE T, LIU B, et al. A new explicit simulation for injection molding and its validation [J]. Polymer Engineering & Science, 2009, 49(6): 1243-52.
[65] CHENG Z, BARRIERE T, LIU B, et al. A fully vectorial and explicit algorithm for mould filling [J]. Journal of Southwest Jiaotong University, 2004, 39(2): 181-4.
[66] LARSEN G, CHENG Z Q, BARRIERE T, et al. A streamline-upwind model for filling front advection in powder injection moulding [M]. NUMIFORM 2010: Proceedings of the 10th International Conference on

Numerical Methods in Industrial Forming Processes 2010: 545-52.
[67] CHENG Z Q. Numerical Simulation on Metal Injection Moulding [D]; Southwest Jiaotong University, 2005.
[68] HETU J F, GAO D M, GARCIA-REJON A, et al. 3D finite element method for the simulation of the filling stage in injection molding [J]. Polymer Engineering & Science, 1998, 38(2): 223-36.
[69] PICHELIN E, COUPEZ T. Finite element solution of the 3D mold filling problem for viscous incompressible fluid [J]. Computer Methods in Applied Mechanics and Engineering, 1998, 163(1–4): 359-71.
[70] BARRIERE T. Expérimentations, Modélisation et Simulation Numérique du Moulage par Injection de Poudres Métalliques [D]; Université de Franche-Comté, 2000.
[71] DUTILLY M. Modélisation du Moulage par Injection de Poudres Métalliques [D]; Université de Franche-Comté, Besancon, France, 1998.
[72] BERTRAND F H, GADBOIS M R, TANGUY P A. Tetrahedral elements for fluid flow [J]. International Journal for Numerical Methods in Engineering, 1992, 33(6): 1251-67.
[73] ROIG B. One-step Taylor–Galerkin methods for convection–diffusion problems [J]. Journal of Computational and Applied Mathematics, 2007, 204(1): 95-101.
[74] LAVAL H, QUARTAPELLE L. A fractional-step Taylor–Galerkin method for unsteady incompressible flows [J]. International Journal for Numerical Methods in Fluids, 1990, 11(5): 501-13.
[75] TONG A Y, WANG Z. A numerical method for capillarity-dominant free surface flows [J]. Journal of Computational Physics, 2007, 221(2): 506-23.
[76] ROKKAM R G, FOX R O, MUHLE M E. Computational fluid dynamics and electrostatic modeling of polymerization fluidized-bed reactors [J]. Powder Technology, 2010, 203(2): 109-24.
[77] NAGAIAH C, WARNECKE G, HEINRICH S, et al. Numerical simulation of temperature and concentration distributions in fluidized beds with liquid injection [J]. Chemical Engineering Science, 2007, 62(6): 1567-90.
[78] JIANG C B, KAWAHARA M, KASHIYAMA K. A Taylor—Galerkin-based finite element method for turbulent flows [J]. Fluid Dynamics Research, 1992, 9(4): 165-78.
[79] SHA B, DIMOV S, GRIFFITHS C, et al. Investigation of micro-injection moulding: Factors affecting the replication quality [J]. Journal of Materials Processing Technology, 2007, 183(2–3): 284-96.
[80] MOHD FOUDZI F, MUHAMAD N, BAKAR SULONG A, et al. Yttria stabilized zirconia formed by micro ceramic injection molding: Rheological properties and debinding effects on the sintered part [J]. Ceramics International, 2013, 39(3): 2665-74.
[81] CHEN P, POLICOVA Z, PACE-ASCIAK C R, et al. Study of molecular interactions between lipids and proteins using dynamic surface tension measurements: a review [J]. Colloids and Surfaces B: Biointerfaces, 1999, 15(3–4): 313-24.
[82] LIOVIC P, LAKEHAL D. Subgrid-scale modelling of surface tension within interface tracking-based Large Eddy and Interface Simulation of 3D interfacial flows [J]. Computers & Fluids, 2012, 63(0): 27-46.
[83] RAESSI M, MOSTAGHIMI J, BUSSMANN M. A volume-of-fluid interfacial flow solver with advected normals [J]. Computers & Fluids, 2010, 39(8): 1401-10.
[84] EYIYUREKLI M, BREEN D. Interactive free-form level-set surface-editing operators [J]. Computers & Graphics, 2010, 34(5): 621-38.
[85] MOELANS N, BLANPAIN B, WOLLANTS P. An introduction to phase-field modeling of microstructure evolution [J]. Calphad, 2008, 32(2): 268-94.
[86] PIANET G, VINCENT S, LEBOI J, et al. Simulating compressible gas bubbles with a smooth volume tracking 1-Fluid method [J]. International Journal of Multiphase Flow, 2010, 36(4): 273-83.
[87] HIRT C W, NICHOLS B D. Volume of fluid (VOF) method for the dynamics of free boundaries [J]. Journal of Computational Physics, 1981, 39(1): 201-25.

[88] SUSSMAN M, PUCKETT E G. A Coupled Level Set and Volume-of-Fluid Method for Computing 3D and Axisymmetric Incompressible Two-Phase Flows [J]. Journal of Computational Physics, 2000, 162(2): 301-37.

[89] WILLIAMS M W, KOTHE D B, PUCKETT E G, et al. Fluid Dynamics at Interface; proceedings of the Cambridge University Press,, Cambridge, F, 1999 [C].

[90] POPINET S. An accurate adaptive solver for surface-tension-driven interfacial flows [J]. Journal of Computational Physics, 2009, 228(16): 5838-66.

[91] RENARDY Y, RENARDY M. PROST: A Parabolic Reconstruction of Surface Tension for the Volume-of-Fluid Method [J]. Journal of Computational Physics, 2002, 183(2): 400-21.

[92] OSHER S, SETHIAN J A. Fronts propagating with curvature-dependent speed: Algorithms based on Hamilton-Jacobi formulations [J]. Journal of Computational Physics, 1988, 79(1): 12-49.

[93] FEDKIW R P, SAPIRO G, SHU C-W. Shock capturing, level sets, and PDE based methods in computer vision and image processing: a review of Osher's contributions [J]. Journal of Computational Physics, 2003, 185(2): 309-41.

[94] BOURLIOUX A. Coupled level set volume of fluid algorithm for tracking material interfaces; proceedings of the in: Proceedings of the 6th International Symposium on Computational Fluid Dynamics, , Lake Tahoe, F, 1995 [C].

[95] SON G, HUR N. A COUPLED LEVEL SET AND VOLUME-OF-FLUID METHOD FOR THE BUOYANCY-DRIVEN MOTION OF FLUID PARTICLES [J]. Numerical Heat Transfer, Part B: Fundamentals, 2002, 42(6): 523-42.

[96] NARD M T, TANGUY S, BERLEMONT A. Coupling level set/VOF/ghost fluid methods: Validation and application to 3D simulation of the primary break-up of a liquid jet [J]. International Journal of Multiphase Flow, 2007, 33(5): 510-24.

[97] LI Q, OUYANG J, YANG B, et al. Numerical simulation of gas-assisted injection molding using CLSVOF method [J]. Applied Mathematical Modelling, 2012, 36(5): 2262-74.

[98] SUN D L, TAO W Q. A coupled volume-of-fluid and level set (VOSET) method for computing incompressible two-phase flows [J]. International Journal of Heat and Mass Transfer, 2010, 53(4): 645-55.

[99] SHU C-W, OSHER S. Efficient implementation of essentially non-oscillatory shock-capturing schemes, II [J]. Journal of Computational Physics, 1989, 83(1): 32-78.

[100] LV X, ZOU Q, ZHAO Y, et al. A novel coupled level set and volume of fluid method for sharp interface capturing on 3D tetrahedral grids [J]. Journal of Computational Physics, 2010, 229(7): 2573-604.

[101] HYSING S. Mixed element FEM level set method for numerical simulation of immiscible fluids [J]. Journal of Computational Physics, 2012, 231(6): 2449-65.

[102] DR AU K, CHEVAUGEON N, MO S N. Studied X-FEM enrichment to handle material interfaces with higher order finite element [J]. Computer Methods in Applied Mechanics and Engineering, 2010, 199(29–32): 1922-36.

[103] YANG X, JAMES A J, LOWENGRUB J, et al. An adaptive coupled level-set/volume-of-fluid interface capturing method for unstructured triangular grids [J]. Journal of Computational Physics, 2006, 217(2): 364-94.

[104] MACKLIN P, LOWENGRUB J. An improved geometry-aware curvature discretization for level set methods: Application to tumor growth [J]. Journal of Computational Physics, 2006, 215(2): 392-401.

[105] RAMŠAK M, ŠKERGET L. 3D multidomain BEM for solving the Laplace equation [J]. Engineering Analysis with Boundary Elements, 2007, 31(6): 528-38.

[106] TRONTIN P, VINCENT S, ESTIVALEZES J L, et al. A subgrid computation of the curvature by a particle/level-set method. Application to a front-tracking/ghost-fluid method for incompressible flows [J]. Journal of Computational Physics, 2012, 231(20): 6990-7010.

[107] RANGOGNI R. Numerical solution of the generalized Laplace equation by coupling the boundary

element method and the perturbation method [J]. Applied Mathematical Modelling, 1986, 10(4): 266-70.

[108] MEIER M, YADIGAROGLU G, SMITH B L. A novel technique for including surface tension in PLIC-VOF methods [J]. European Journal of Mechanics - B/Fluids, 2002, 21(1): 61-73.

[109] RAESSI M, MOSTAGHIMI J, BUSSMANN M. Advecting normal vectors: A new method for calculating interface normals and curvatures when modeling two-phase flows [J]. Journal of Computational Physics, 2007, 226(1): 774-97.

[110] LI C-T, LAI F C. Visualization of the surface tension and gravitational effects on flow injection in center-gated disks [J]. International Communications in Heat and Mass Transfer, 2010, 37(3): 230-3.

[111] BRACKBILL J U, KOTHE D B, ZEMACH C. A continuum method for modeling surface tension [J]. Journal of Computational Physics, 1992, 100(2): 335-54.

[112] CHENG Z, BARRIERE T, LIU B, et al. A vectorial algorithm with finite element method for prediction of powder segregation in metal injection molding [J]. International Journal for Numerical Methods in Fluids, 2012, 70(10): 1290-304.

[113] DAĞ İ, CANıVAR A, ŞAHIN A. Taylor–Galerkin and Taylor-collocation methods for the numerical solutions of Burgers' equation using B-splines [J]. Communications in Nonlinear Science and Numerical Simulation, 2011, 16(7): 2696-708.

[114] OLEVSKY E A. Theory of sintering: from discrete to continuum [J]. Materials Science and Engineering: R: Reports, 1998, 23(2): 41-100.

[115] HAUSNER H H. //RISTIC M M. Sintering New Developments. Elsevier, Amsterdam. 1979: 3.

[116] KUCZYNSKI G C. //RISTIC M M. Sintering New Developments. Elsevier, Amsterdam. 1979: 245.

[117] http://wwwipmdnet/Introduction_to_powder_metallurgy/Sintering.

[118] MANESHIAN M H, SIMCHI A. Solid state and liquid phase sintering of mechanically activated W–20 wt.% Cu powder mixture [J]. Journal of Alloys and Compounds, 2008, 463(1–2): 153-9.

[119] LEE Y-C, YEH Y-Y, TSAI P-R. Effect of microwave sintering on the microstructure and electric properties of (Zn,Mg)TiO3-based multilayer ceramic capacitors [J]. Journal of the European Ceramic Society, 2012, 32(8): 1725-32.

[120] OLAKANMI E O. Selective laser sintering/melting (SLS/SLM) of pure Al, Al–Mg, and Al–Si powders: Effect of processing conditions and powder properties [J]. Journal of Materials Processing Technology, 2013, 213(8): 1387-405.

[121] WANG L, ZHANG J, JIANG W. Recent development in reactive synthesis of nanostructured bulk materials by spark plasma sintering [J]. International Journal of Refractory Metals and Hard Materials, 2013, 39(0): 103-12.

[122] PERSSON P, JARFORS A E W, SAVAGE S. Self-propagating high-temperature synthesis and liquid-phase sintering of TiC/Fe composites [J]. Journal of Materials Processing Technology, 2002, 127(2): 131-9.

[123] HULBERT D M, ANDERS A, DUDINA D V, et al. The absence of plasma in "spark plasma sintering" [J]. Journal of Applied Physics, 2008, 104(033305-7

[124] RAHAMAN M N. Ceramic Processing and Sintering [M]. 2nd ed, Marcel Dekker Inc. New York, USA. 2003.

[125] UPADHYAYA G S. Some issues in sintering science and technology [J]. Materials Chemistry and Physics, 2001, 67(1–3): 1-5.

[126] GERMAN R M. Powder injection molding - design and applications [M]. Pennsylvania, USA, 2003.

[127] GERMAN R M. Computer modeling of sintering processes [J]. International Journal of Powder Metallurgy, 2001, 38(2): 48-66.

[128] ZHANG R. Numerical simulation of solid-state sintering of metal powder compact dominated by grain

boundary diffusion [D]; The Pennsylvania State University, 2005.

[129] FRENKEL J. Viscous flow of crystalline bodies under the action of surface tension [J]. Journal of Physics (USSR), 1945, 9(5): 385–91.

[130] KUCZYNSKI G C. Self diffusion in sintering of metallic particles [J]. Metals Transactions, 1949, 185(169-78.

[131] KINGERY W D, BERG M. Study of the initial stages of sintering of solids by viscous flow, evaporation condensation and self-diffusion [J]. Journal of Applied Physics, 1955, 26(10): 1205-12.

[132] COBLE R L. Sintering of crystalline solids. I. Intermediate and final state diffusion models [J]. Journal of Applied Physics, 1961, 32(5): 787-92.

[133] MACKENZIE J K, SHUTTLEWORTH R. A Phenomenological Theory of Sintering [J]. Proceedings of The Physical Society Section B, 1949, 62(12): 833-52.

[134] ASHBY M F. A first report on sintering diagrams [J]. Acta Metallurgica, 1974, 22(3): 275-89.

[135] ARLT E. The influence of an increasing particle coordination on the densification of spherical polders [J]. Acta Metallurgica, 1982, 30(10): 1883-90.

[136] EXNER H E, ARZT E. Sintering processes [M]//CAHN R W, HAASEN P. Physical Metallurgy, 30, Elsevier Science. 1996: 2628–62.

[137] ZENG P, ZAJAC S, CLAPP P C, et al. Nanoparticle sintering simulations [J]. Materials Science and Engineering: A, 1998, 252(2): 301-6.

[138] PAN J, LE H, KUCHERENKO S, et al. A model for the sintering of spherical particles of different sizes by solid state diffusion [J]. Acta Materialia, 1998, 46(13): 4671-90.

[139] ZHANG W, SCHNEIBEL J H. The sintering of two particles by surface and grain boundary diffusion—a two-dimensional numerical study [J]. Acta Metallurgica et Materialia, 1995, 43(12): 4377-86.

[140] ZHANG B, GASIK M M. Stress evolution in graded materials during densification by sintering processes [J]. Computational Materials Science, 2002, 25(1–2): 264-71.

[141] ABOUAF M, CHENOT J L, RAISSON G, et al. Finite element simulation of hot isostatic pressing of metal powders [J]. International Journal for Numerical Methods in Engineering, 1988, 26(1): 191–212.

[142] DUVA J M, CROW P D. The densification of powders by power-law creep during hot isostatic pressing [J]. Acta Metallurgica et Materialia, 1992, 40(1): 31-5.

[143] COCKS A C F. Inelastic deformation of porous materials [J]. Journal of the Mechanics and Physics of Solids, 1989, 37(6): 693-715.

[144] COCKS A C F, SINKA I C. Constitutive modelling of powder compaction – I. Theoretical concepts [J]. Mechanics of Materials, 2007, 39(4): 392-403.

[145] OGHBAEI M, MIRZAEE O. Microwave versus conventional sintering: A review of fundamentals, advantages and applications [J]. Journal of Alloys and Compounds, 2010, 494(1–2): 175-89.

[146] GUO Y, YI J, LUO S, et al. Fabrication of W–Cu composites by microwave infiltration [J]. Journal of Alloys and Compounds, 2010, 492(1–2): L75-L8.

[147] DEMIRSKYI D, RAGULYA A, AGRAWAL D. Initial stage sintering of binderless tungsten carbide powder under microwave radiation [J]. Ceramics International, 2011, 37(2): 505-12.

[148] TOMPSETT G A, CONNER W C, YNGVESSON K S. Microwave synthesis of nanoporous materials [J]. Chemphyschem 2006, 7(2): 296-319.

[149] TAKAHASHI H, KATO K, JINHAO Q, et al. Property of lead zirconate titanate actuator manufactured with microwave sintering process [J]. Japanese Journal of Applied Physics, 2001, 40(2A): 724-7.

[150] HUANG G, ZHOU D, XU J, et al. Low-temperature sintering and microwave dielectric properties of (Zr,Sn)TiO4 ceramics [J]. Materials Science and Engineering: B, 2003, 99(1–3): 416-20.

[151] ROY R, AGRAWAL D, CHENG J, et al. Full sintering of powdered-metal bodies in a microwave field [J]. Nature, 1999, 399(6737): 668-70.

[152] KONG X, QUINARD C, BARRIERE T, et al. Mixing and Characterisation of stainless steel 316L feedstock [J]. Int J Mater Form, 2009, 2(1): 709-12.

[153] QUINARD C, BARRIERE T, GELIN J C. Development and property identification of 316L stainless steel feedstock for PIM and μPIM [J]. Powder Technology, 2009, 190(1–2): 123-8.

[154] LARSEN G, CHENG Z Q, BARRIERE T, et al. Modelling and numerical simulation of biphasic fluid flow [J]. Steel Research International, 2010, 81(9): 1458-61.

[155] SONG J, BARRIERE T, LIU B, et al. Experimental and numerical analysis on the sintering behaviours of injection moulded components in 316L stainless steel powder [J]. Powder Metallurgy, 2010, 53(4): 295-304.

[156] RACK H J, KALISH D. The strength, fracture toughness, and low cycle fatigue behavior of 17-4 PH stainless steel [J]. MT, 1974, 5(7): 1595-605.

[157] ZAKERI M, BAHRAMI A, MOUSAVI ANIJDAN S H. Using genetic algorithm in heat treatment optimization of 17-4PH stainless steel [J]. Materials & Design, 2007, 28(7): 2034-9.

[158] LIN X, CAO Y, WU X, et al. Microstructure and mechanical properties of laser forming repaired 17-4PH stainless steel [J]. Materials Science and Engineering: A, 2012, 553(0): 80-8.

[159] SUNG H-J, HA T K, AHN S, et al. Powder injection molding of a 17-4 PH stainless steel and the effect of sintering temperature on its microstructure and mechanical properties [J]. Journal of Materials Processing Technology, 2002, 130–131(0): 321-7.

[160] YE H, LIU X Y, HONG H. Sintering of 17-4PH stainless steel feedstock for metal injection molding [J]. Materials Letters, 2008, 62(19): 3334-6.

[161] SIMCHI A, ROTA A, IMGRUND P. An investigation on the sintering behavior of 316L and 17-4PH stainless steel powders for graded composites [J]. Materials Science and Engineering: A, 2006, 424(1–2): 282-9.

[162] IMGRUND P, ROTA A, SIMCHI A. Microinjection moulding of 316L/17-4PH and 316L/Fe powders for fabrication of magnetic–nonmagnetic bimetals [J]. Journal of Materials Processing Technology, 2008, 200(1–3): 259-64.

[163] CAMPA ONE L, PAOLA C, MASCHERONI R. Modeling and Simulation of Microwave Heating of Foods Under Different Process Schedules [J]. Food Bioprocess Technol, 2012, 5(2): 738-49.

[164] CLARK D E, FOLZ D C, WEST J K. Processing materials with microwave energy [J]. Materials Science and Engineering: A, 2000, 287(2): 153-8.

[165] LEONELLI C, VERONESI P, DENTI L, et al. Microwave assisted sintering of green metal parts [J]. Journal of Materials Processing Technology, 2008, 205(1–3): 489-96.

[166] PRABHU G, CHAKRABORTY A, SARMA B. Microwave sintering of tungsten [J]. International Journal of Refractory Metals and Hard Materials, 2009, 27(3): 545-8.

[167] CHARMOND S, CARRY C P, BOUVARD D. Densification and microstructure evolution of Y-Tetragonal Zirconia Polycrystal powder during direct and hybrid microwave sintering in a single-mode cavity [J]. Journal of the European Ceramic Society, 2010, 30(6): 1211-21.

[168] WU Q, ZHANG X, WU B, et al. Effects of microwave sintering on the properties of porous hydroxyapatite scaffolds [J]. Ceramics International, 2013, 39(3): 2389-95.

[169] ZHENG X, DU Y, XIAO J, et al. Celsian/yttrium silicate protective coating prepared by microwave sintering for C/SiC composites against oxidation [J]. Materials Science and Engineering: A, 2009, 505(1–2): 187-90.

[170] CHANDRASEKARAN S, BASAK T, RAMANATHAN S. Experimental and theoretical investigation on microwave melting of metals [J]. Journal of Materials Processing Technology, 2011, 211(3): 482-7.

[171] LIU Y, MIN F-F, ZHU J-B, et al. Effect of nanometer Al2O3 powder on microstructure and properties of alumina ceramics by microwave sintering [J]. Materials Science and Engineering: A, 2012, 546(0): 328-31.

[172] TANG C Y, ZHANG L N, WONG C T, et al. Fabrication and characteristics of porous NiTi shape memory alloy synthesized by microwave sintering [J]. Materials Science and Engineering: A, 2011, 528(18): 6006-11.

[173] MULA S, SAHANI P, PRATIHAR S K, et al. Mechanical properties and electrical conductivity of Cu–Cr and Cu–Cr–4% SiC nanocomposites for thermo-electric applications [J]. Materials Science and Engineering: A, 2011, 528(13–14): 4348-56.

[174] PANDA S S, SINGH V, UPADHYAYA A, et al. Sintering response of austenitic (316L) and ferritic (434L) stainless steel consolidated in conventional and microwave furnaces [J]. Scripta Materialia, 2006, 54(12): 2179-83.

[175] BOSE A, AGRAWAL D, DOWDING. R J. Preliminary Investigations into Microwave Processing of Powder Injection Molded 17-4 PH Stainless Steel [J]. International Conference on Powder Metallurgy and Particulate Materials, 2004, 53.

[176] SAPTONO R. Solid State Sintering of Nanostructured Ceramics [J]. Procedia Engineering, 2012, 50(0): 369-80.

[177] BELGACEM M, THIERRY B, JEAN-CLAUDE G. Investigations on thermal debinding process for fine 316L stainless steel feedstocks and identification of kinetic parameters from coupling experiments and finite element simulations [J]. Powder Technology, 2013, 235(0): 192-202.

[178] MENEZES R R, SOUTO P M, KIMINAMI R H G A. Microwave hybrid fast sintering of porcelain bodies [J]. Journal of Materials Processing Technology, 2007, 190(1–3): 223-9.

[179] KIM-HAK O, SOULIER M, SZKUTNIK P-D, et al. Microwave sintering and thermoelectric properties of p-type (Bi0.2Sb0.8)2Te3 powder [J]. Powder Technology, 2012, 226(0): 231-4.

[180] BERNARD-GRANGER G, GUIZARD C. Apparent Activation Energy for the Densification of a Commercially Available Granulated Zirconia Powder [J]. Journal of the American Ceramic Society, 2007, 90(4): 1246-50.

[181] ISKANDER M D, ANDRADE A O N M. FDTD simulation of microwave sintering of ceramics in multimode cavities [J]. EEE Trans Microwave Theory and Techniques, 1994, 42(1): 793-9.

[182] KOZLOV P V, RAFATOV I R, KULUMBAEV E B, et al. On modeling of microwave heating of a ceramic material [J]. Journal of physics D: Applied Physics, 2007, 40(9): 2927-35.

[183] LASRI J, RAMESH P D, SCH CHTER L. Energy Conversion during Microwave Sintering of a Multiphase Ceramic Surrounded by a Susceptor [J]. Journal of the American Ceramic Society, 2000, 83(6): 1465-8.

[184] SONG J, BARRIERE T, GELIN J C, et al. Powder injection molding of metallic and ceramic hip implants [J]. International Journal of Powder Metallurgy, 2009, 45(3): 25-34.

[185] SANTOS T, VALENTE M A, MONTEIRO J, et al. Electromagnetic and thermal history during microwave heating [J]. Applied Thermal Engineering, 2011, 31(16): 3255-61.

[186] BOUVARD D, CHARMOND S, CARRY C P. Mutiphysics Simulation of Microwave Sintering in a Monomode Cavity [M]. 12 Seminar Computer Modeling in Microwave Engineering & Applications. Grenoble, France. 2010.

[187] COBLE R L. A model for boundary diffusion controlled creep in polycrystalline materials [J]. Journal of Applied Physics, 1963, 34(6): 1679-82.

[188] BORDIA R K, SCHERER G W. On constrained sintering-I Constitutive model for a sintering body [J]. Acta Materialia, 1988, 36(9): 2393-7.

[189] NABARRO F R N. Creep at very Low Rates [J]. Metallurgical and Materials Transactions A, 2002, 33A(153): 213-8.

[190] GASIK M, ZHANG B. A constitutive model and FE simulation for the sintering process of powder compacts [J]. Computational Materials Science, 2000, 18(1): 93-101.

[191] R.K B, SCHERER G W. On constrained sintering-I Constitutive model for a sintering body [J]. Acta Metallurgica, 1988, 36(9): 2393-7.

[192] KRAFT T, RIEDEL H. Numerical simulation of solid state sintering; model and application [J]. Journal of the European Ceramic Society, 2004, 24(2): 345-61.

[193] PETERSSON A, ÅGREN J. Constitutive behaviour of WC–Co materials with different grain size sintered under load [J]. Acta Materialia, 2004, 52(7): 1847-58.

Publications

Published papers

[1] 石建军, 成志强, 柳葆生. 微注射成形中表面张力效应的数值模拟. 应用力学学报[J], Vol.27, No.4, 2010, 723-727.
Jianjun SHI, Zhiqiang CHENG, Baosheng LIU. Numerical Analysis to Surface Tension Effects of Micro-Injection Molding [J]. Chinese Journal of Applied Mechanics, 2010, 27(4):723-727.

[2] 石建军, 成志强, 柳葆生. 注射成形填充模拟的修正算法. 西南交通大学学报[J], Vol.47, No.6, 2012, 962-967.（EI, DOI: 10.3969/j.issn.0258-2724.2012.06.009）
Jianjun SHI, Zhiqiang CHENG, Baosheng LIU. Modified Algorithm for Simulation of Injection Molding Process [J]. Journal of Southwest Jiaotong University, 2012, 47(6): 962-967.（EI, DOI: 10.3969/j.issn.0258-2724.2012.06.009）

[3] Jianjun SHI, Zhiqiang CHENG, Jean-Claude GELIN, Baosheng LIU, Thierry BARRIERE. Modified method for simulation of the filling states at the end of injection molding process, The 2nd International Conference on Advances in Computational Modeling and Simulation. Applied Mechanics and Materials [J]. 2013, 444-445:1042-1049. (EI, DOI: 10.4028/www.scientific.net/ AMM.444-445.1042)

[4] 石建军, 成志强, J.C. Gelin, 等. 微波烧结过程的建模与模拟研究, 机械工程材料[J]. (已录取待发表)
Jianjun SHI, Zhiqiang CHENG, Jean-Claude GELIN, Baosheng LIU, Thierry BARRIERE. Modeling and simulation on process of microwave sintering, Materials for Mechanical Engineering [J]. (Accepted)

[5] 石建军, 成志强, J.C. Gelin, 等. 微波烧结多物理场耦合过程的数值模拟方法研究，科技论文在线, 2013, http://www.paper.edu.cn.
Jianjun SHI, Zhiqiang CHENG, Jean-Claude GELIN, Baosheng LIU, Thierry BARRIERE. Numerical Simulation Method on Multi-physics Coupling Process of Microwave Sintering. Chinese Sciencepaper Online, 2013, http://www.paper.edu.cn.

Manuscript under review

[6] Jianjun SHI, Zhiqiang CHENG, Jean-Claude GELIN, Baosheng LIU, Thierry BARRIERE. Efficient sintering of 17-4PH stainless steel powder by microwave and gradient in mechanic properties. Materials Design [J].

[7] Jianjun SHI, Zhiqiang CHENG, Jean-Claude GELIN, Baosheng LIU, Thierry BARRIERE. A simple and systematic scheme implemented in explicit FEM solver for surface tension effects in micro-injection molding. Journal of Computational Physics [J].

Abstrat :

Powder Injection molding process consists off our main stages: feedstock preparation, injection molding, debinding and sintering. The thesis presents the research on two main aspects: micro-injection molding and microwave sintering. The main contributions can be concluded in the following four aspects: Modification and supplement of previous algorithm for the simulation of injection molding process; Evaluation and implementation of surface tension effect in simulation for micro injection; Microwave sintering experiments of compacts based on 17-4PH stainless steel; Realization of the microwave sintering simulation with the coupling of multi-physics, including the classic microwave heating, heat transfer, and the supplement of model for sintering densification of powder impacts

Key words：

Micro-Injection Molding, Microwave Sintering, surface tension effect, 17-4PH stainless steel powder, Numerical Simulation, Multi-physics

Résumé :

Procédé de moulage par injection de poudres est constitué de quatre étapes principales: la préparation des matières premières, moulage par injection, le déliantage et le frittage. Cette thèse présente les recherches sur deux aspects principaux: la micro-injection et frittage par micro-ondes. Les contributions principaux peuvent être conclues dans les quatre aspects suivants: Modification et complément de l'algorithme précédent pour la simulation du procédé de moulage par injection; L'évaluation et la mise en oeuvre de l'effet de tension de surface en simulation pour micro-injection; Micro-ondes expériences de frittage de compacts basés sur l'acier inoxydable 17-4PH; Réalisation de la simulation de frittage à micro-ondes avec couplage de la multi-physique, y compris le chauffage à micro-ondes classique, le transfert de chaleur, et le supplément de modèle pour la densification de frittage de la poudre compacté.

Mots clés:

La Micro-Injection, Micro-ondes Frittage, L'effet de la Tension de Surface, Poudre d'acier Inoxydable17-4PH, Simulation Numérique, Multi-physiques

SPIM

■ École doctorale SPIM 16 route de Gray F - 25030 Besançon cedex

■ tél. +33 (0)3 81 66 66 02 ■ ed-spim@univ-fcomte.fr ■ www.ed-spim.univ-fcomte.fr

UFC UNIVERSITÉ DE FRANCHE-COMTÉ